UNIVERSITA' DEGLI STUDI DI PADOVA

DIPARTIMENTO DI SCIENZE CHIMICHE

CORSO DI LAUREA MAGISTRALE IN CHIMICA

TESI DI LAUREA MAGISTRALE

COPPER-ORGANIC BINDER COMPLEXES IN PIGMENTS: AN EPR STUDY

Relatore: Prof. Alfonso Zoleo

Controrelatrice: Prof.ssa Marta Maria Natile

LAUREANDO: PUNIS RICCARDO

ANNO ACCADEMICO 2021-2022

CONTENTS

Introduction

Since ancient times, many copper compounds, both synthetic and natural, have been used as blue or green pigments and dyes. Their diversity, reflecting their various chemical composition as well as their chemical stability and their origin, makes their characterization very challenging. Pigments were usually mixed with some ligands, as for example linseed oil, arabic gum, collagen, or yolk, to reach some particular painting effects: for example, pigment mixtures realized with collagen appears glassy and bright. In recent years, with the developing of many spectroscopic (Raman, FT-IR, UV-Vis, etc.) and analytical techniques (GC-MS, HPLC, etc.) new pieces of knowledge in cultural heritage chemistry have emerged but a complete and wide characterization is not yet available. There is not only a characterization problem, but it is well known since ancient times [1] that these kinds of pigments and mixtures are very prone to degradation. In fact, copper-induced degradation is one the most relevant problem in cultural heritage conservation [2, 3, 4].

Figure 1: Pictures of waterways in Codex 29: cc. 88 verso, 89 recto [5].

It has also been discovered that copper ions and metal centers in general are involved in the supporting material (parchment, wooden boards, etc.) degradation [6, 7]. For example, *Verdigris* is a widely used green pigment, it is one of the most degradation prone pigments, and thousands of artists across centuries have used this cheap, natural color. Quoting "*The Book of the Art*" by Cennino Cennini [8]:

"*Grind it with vinegar, which it is its nature to retain; and it makes a green for grass perfect and beautiful to the eye, but not durable."* *

The chemical degradation of supporting material and darkening effects suggest that pigment is not simply dispersed in the ligand matrix (as in colloidal kind of materials) but metal ions are dissolved into the matrix, creating metal-ligand complexes able to react and give degradation processes. It is evident that is strictly necessary to prove metal-ligand formation and, once verified this process, to characterize these complexes: characterization could give important information to clarify darkening and damaging processes.

In this context, this master's thesis has the aim to study copper-organic ligand complexes in raw pigments and pigment-ligand mixtures by a non-destructive and very sensitive technique: the Electron Paramagnetic Resonance (EPR) spectroscopy. EPR spectroscopy and derived techniques can give highly detailed information about magnetic species present in samples, thanks to its very high sensitivity and very high specificity: just Cu(II) species in organic complexes or matrices are usually detected.

This thesis has the following structure: copper-based pigments nature, properties and usage are overviewed in Chapter 1, EPR technique basic concepts and peculiar features

* *"Trialo con aceto, che ritiene secondo suo' natura. E se vuoi fare un verde in erba perfettissimo, è bello all'occhio, ma non dura"*

of main metal centers (Cu(II), Fe(III) and Mn(II)) are overviewed in Chapter 2, preparation of pigments – organic ligand mixtures and experimental conditions – are overviewed in Chapter 3, experimental results are reported in Chapter 4, a brief discussion of the experimental results is reported in Chapter 5, and finally general conclusions on the work done are compiled in Chapter 6.

Chapter 1: Pigments and binders overview

1.1 Pigments

Pigments are usually inorganic compounds that contain metal cations. This master's thesis is focused on copper-based pigments (Cu (II) metal ions) because of their tendency to damaging processes [2, 3 4, 6, 7]. Next paragraphs describe pigments used in the master's thesis work from historical and chemical points of view.

1.1.1 Verdigris

Verdigris was mentioned for the first time as a green pigment in ancient Greek and Roman literature: Theophrastus wrote about a rust of copper [9], Plinio [10] referred to the green pigment as "*aeurgo*" and finally Vitruvius [11] called it "*aureca*". However, "*aureca*" or "*aeurgo*" were referred to a general group of compounds coming from some kind of process concerning copper metal.

Other types of green and blue pigments coming from chemical treatments of copper were reported in other manuscripts: for example, in the "*Mappae Clavicula*" [12] is named the "*viride rotomagense*", a mixture of copper acetate and a small quantity of copper salts of fatty acids. Therefore, historically "*verdigris*" is referred to a multitude of compounds with common roots: they were prepared by chemistry methods. Cennino Cennini in "*The Book of The Art*" says [8]:

"*There is a green pigment called verderame* [†]*. It is sufficiently green of itself, and is an artificial chemical production, made of copper and vinegar*" [‡]

Quoting also "*De coloribus et de artibus Romanorum*" [9]:

"*Fill the basil with vinegar, put inside copper foils and drop in as much copper as you can have, and leave it like this for one, two or three months and then you will see a wonderful green*" [§]

Instead, nowadays the English term "*verdigris*" – probably derived from French term "*vert de Grèce*" – refers exclusively to copper salts of acetic acid (copper acetate). Therefore, in this master's thesis the term "*verdigris*" is referred to a copper acetate salt avoiding any misunderstanding.

Verdigris has been widely used by many artists around the world thanks to its intense green tone. The green pigment was mixed also with white lead, even if Cennini discourages its use [7]. According to Braxandal [13], this kind of pigment was not used to paint relevant elements in pictorial compositions, but in marginal areas because of its cheapness and in spite of its degradation problems. Verdigris was also used as a drying agent in oil media [8].

As discussed in the introduction, this pigment is very prone to darkening and, due to the presence of copper Cu (II) ions, is involved in supporting material degradation. In

[†] "*Verderame*" stands for "*verdigris*" in Italian

[‡] "*Verde è un colore il quale si chiama verderame. Per se medesimo è verde assai, ed è artificiato con archimia, cioè di rame e d'acieto*". It is interesting to point out that Cennini used the term "*archimia*" (alchemy) instead of chemistry.

[§] *"Imple pelvim de aceto albi vini, et immitte laminas cupri ed quidquid cupri poteris habere, proice intus, et sic stare permittes per spatium unius mensis vel duorum vel trium, et postea optimum viriem procreatum invenies"*

fact, the chemical structure of copper acetate has been very well characterized by many techniques [14, 15, 16] (see **Figure 1.1**).

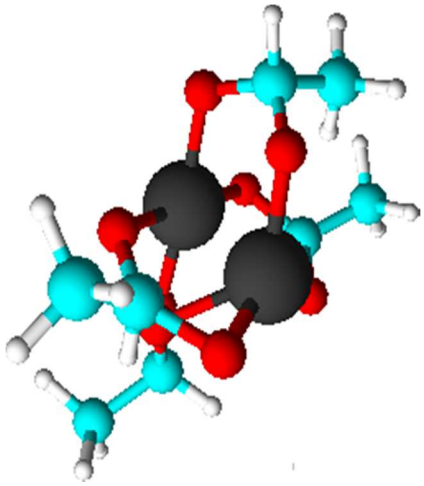

Figure 1.1: Copper acetate structure.

In general, copper acetate compounds can be divided into two main categories: neutral and basic verdigris pigments. In general, all these compounds are based on a bimetallic carboxylate complex with a bidentate bridging coordination $Cu_2(CH_3COO)_4$ [16]. Copper ion has an octahedral distorted coordination due to Jahn-Teller effect: more specifically, ligands arrange in a square-planar coordination (Cu^{2+}: [Ar] $3d^9$). In the copper coordination, the number of water coordinated to the metal center, or the number of hydroxyl groups, could change: these changes give rise to pigments differently blue or green colored [16]. For this reason, as explained also by Cennino Cennini [8], often the rough basic copper acetate, resulting from the initial action of vinegar on copper, was treated with acetic acid to obtain a bright green neutral copper acetate also called "*purified*" verdigris [17]. Other differences between two groups of compounds are present: for example, basic copper acetate is only slightly soluble in cold water while neutral copper acetate entirely dissolve in water with no degradation.

In the past, neutral verdigris was preferred to the basic one [17], having a well-defined blue-green tone, while basic verdigris pigments have variable blue-greenish hue.

According to its structure, many authors have proposed many degradation processes: changing of copper oxidation state, changing of oxidation state in the carboxylate bidentate binder, or radical degradation in acidic environment. In fact, pH could be also a factor inducing chromatic modifications due the reaction of copper acetate [18]. However, a complete explanation of these processes is not yet present.

Figure 1.2: Neutral verdigris powder.

1.1.2 Copper Resinate

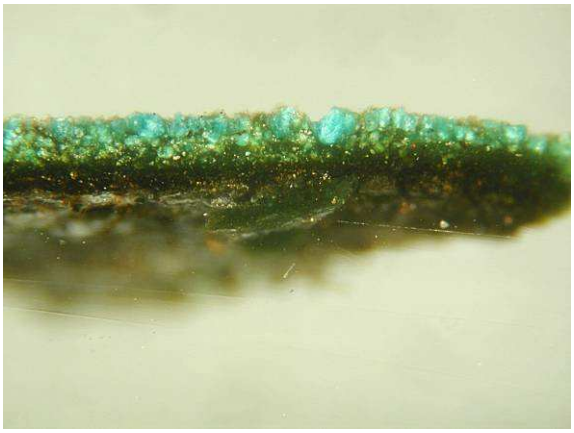

Figure 1.3: Copper resinate in a pictorial film section.

The term "*copper resinate*" refers to copper salts of resin acids. There is a big deal of uncertainty about copper resinate usage as an actual pigment in the art history. Copper resinate has a grass green and transparent aspect. Laurie and Flieder found similar colors in illuminated, ancient manuscripts of the tenth to fifteenth century [19,20]. However, Flieder himself suggested the formation of these kind of colors because of the reaction between verdigris, or malachite, and the protein medium that composes the pictorial layer (egg tempera was commonly used as binder for miniature painting). Therefore, an ancient usage of this pigment is unlikely. In addition to what reported before, the first recipe to prepare copper resinate goes back to the seventeenth century, and was given by De Mayerne ** [16]. The result of the recipes is a glassy, bright green pigment: the main characteristics of copper resinate. The main chemical product of this recipe is a copper salt of *abietic acid,* $C_{19}H_{29}COOH$, the main component of pine resin. According to De Mayerne's recipe, where natural resins are used, other copper salts could be present: e.g., copper salts of isopimaric acid or levopimaric acid. These

** *"Beau Verd. Rp. Therebentine de Venisse ~ij, huile de Therebentine ~jss. mesles, adjoustes Vert de gris mis en morceaulx 3ij, mettes sur cendres chaude & faittes bouillir doulcement. Essayes sur vn verre si la couleur vous plaist; passes par vn ligne"*

acids differs one from the other only for the double bonds positions as shown in **Figure 1.44**. Some kind of natural resin contains high quantities of these two diterpenoids [18] (see **Table 1.1**).

Conifer species	Origin	Pimaric acid	Sandaracopimaric acid	Isopimaric acid	Levopimaric acid	Neoabietic acid	Abietic acid
Pinus Pinaster	Europe	8	2	12	39	18	14
Pinus Halepensis	Europe	1	10	39	37	2	10
Pinus Sylvestris	Europe-Asia	19	3	2	34	10	28
Pinus Ponderosa	North America	8	3	15	40	11	11

Table 1.1: Diterpenoids w/w percentages in main natural resins [18].

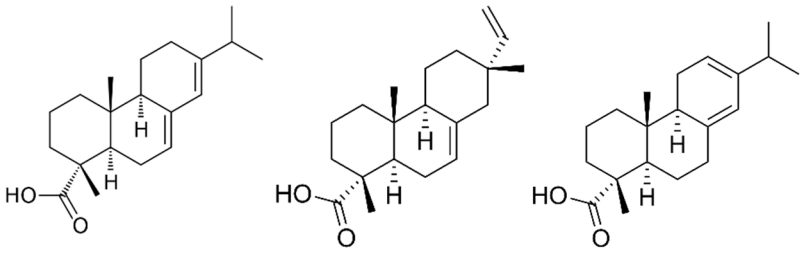

Figure 1.4: Structures of abietic, isopimaric, and levopimaric acid.

Nowadays, copper resinate is usually prepared by reacting a solution of copper salts with an aqueous solution of sodium resinate: a copper salt of abietic acid is the main product.

The chemical structure of copper resinate has been determined [13,14,15], and it is very similar to the verdigris one. In fact, is based on the same bidentate structure with a square-planar coordination of copper centers. However, a different group functionalizes the acetate group, as shown in **Figure 1.5**.

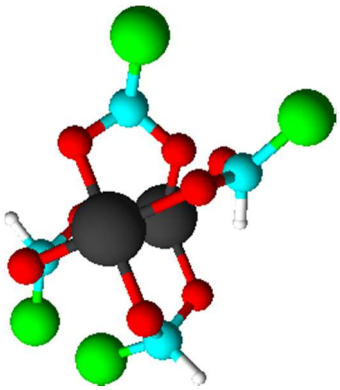

Figure 1.5: Copper resinate structure. Green balls could be abietic acid, isopimaric or levopimaric acid.

1.1.3 Azurite

Figure 1.6: Azurite mineral.

"There is a natural pigment of a blue color, which is found in and around veins of silver" [8].

Azurite (**Figure 1.9**) is a pigment of formula $Cu_3(OH)_2(CO_3)_2$, which is found in nature as mineral. With respect to verdigris, or copper resinate, azurite is quite stable in oil and tempera paintings. Exposed to air and humidity, it can change to the green pigment malachite, a different copper carbonate, according to the reaction:

$2[2CuCO_3 \cdot Cu(OH)_2] + H_2O \rightarrow 3[CuCO_3 \cdot Cu(OH)_2] + CO_2$

However, when mixed with a binder, azurite is rarely exposed to humidity, and this latter reaction does not occur. Also, contrary to verdigris and copper resinate, no degradation phenomena are known to happen on the material supports where azurite was used. This has made azurite a much-appreciated blue pigment.

However, azurite is not suitable for fresco painting. As shown in **Figure 1.10**, azurite is stable in the pH range 6-8, while at basic pH (as present in fresco painting), malachite, tenorite and other carbonates are more stable, causing a color change of painting from blue to green: this happened, for example, in the Cimabue fresco paintings in the ceiling of the Upper Church of St Francis in Assisi [8,17]

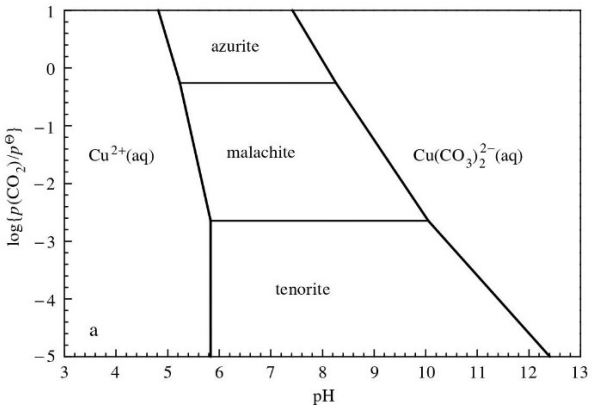

Figure 1.7: pH dependence of copper carbonates [17].

Moreover, in presence of sodium chloride (e.g., in areas close to the sea), azurite easily turns into a basic chloride copper mineral called paratacamite.

This pigment was for many centuries the most important light blue pigment, together with ultramarine blue. In fact, very often suppliers sold azurite as ultramarine blue (more expensive), but it was likewise simple discover the fraud: azurite turns into copper oxide by heating up the sample with a flame, ultramarine blue (from lapis

lazuli) does not [7]. The relevance of this pigment in the past was very high. In fact, Cennino wrote a method to reproduce the azurite tone with other pigment[††].

The preparation of the pigment powder from the mineral was easy: selected lumps of azurite were simply grinded, washed and sieved. Different blue tones can be obtained grinding more, or less, the pigment.

In the azurite structure, copper ion is placed into two kinds of slightly distorted octahedral sites (see **Figure 1.11**). In one site, the copper ion is in a square-planar coordination, while in the second site it has a square pyramidal environment.

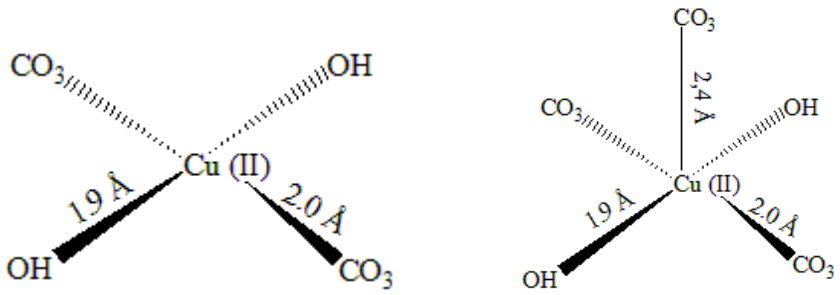

Figure 1.8: Azurite copper centers structures.

1.1.4 Malachite

Figure 1.12: Malachite mineral.

[††] *"Azurro che è come sbiadato, simigliante ad azzurro. Sì togli hindaco bacchadeo e ttrialo perfettissimamente […] e meschola un pocho di biaccha […] o un pocho di biancho sangiovanni"*

Malachite is a green pigment massively present as a mineral, with chemical formula $Cu_2CO_3(OH)_2$. It is commonly found in the azurite ores, since, as seen in the previous section, azurite turns into malachite with humidity. In the "*Libro dell'Arte"*, Cennino Cennini reports that malachite pigment can be obtained artificially from azurite, although it does not specify the way to do it‡‡.

In "*De arte Illuminadi*" [1] more information is available. Quoting the text:

"Natural green is so found: it is the green ground that is ordinary used by painters and the 'viride azurinum' " §§

Large ore deposits are located in the Ural Mountains and Hungary and probably the last was the main ore deposit even in medieval times. Its color is a pale green with a sandy consistency. When applied in paintings, it does not show particular darkening processes, and that made this pigment one of the most loved green colors in ancient times, with a usage spread all over the world [18]. Even some Chinese and Japanese pieces of art were colored with malachite pigment [17]. An example is shown below in **Figure 1.13**.

‡‡ *"Verde è un colore el quale è mezzo naturale: e questo si fa artifizialmente, ché si fa d'azzurro della Magna; e questo si chiama verde azzurro. Non ti metto come si fa, ma compera del fatto."*

§§ *"Viridis colori naturali reperitur sic: videlicet, terra viridis qua communiter pictores utuntur, et viride azurinum"*

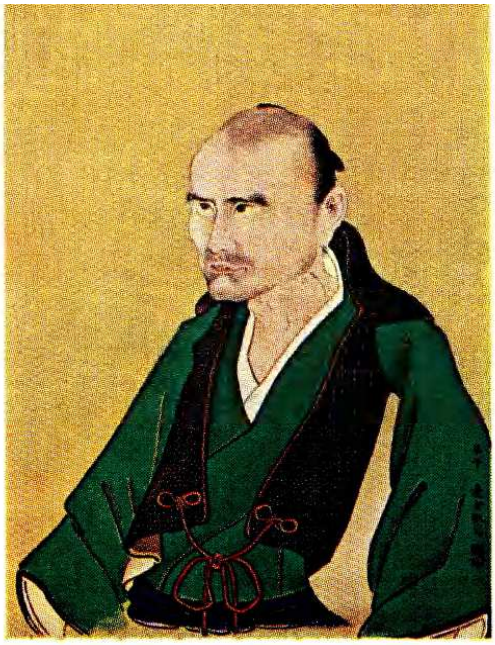

Figure 1.13: Portrait of Sato Issai, Edo Period, Nanga school, by Watanabe Kazan (1793-1841). Courtesy of Freer Gallery of Art, 68.66. Photo: Raymond A. Schwartz.

The preparation of the pigment from the mineral is very simple: a bunch of malachite is crushed, ground into powder and washed.

In the carbonate structure of malachite mineral, copper ions (Cu(II)) are present in two different octahedral sites, distorted through Jahn-Teller effect. The two sites are shown in **Figure 1.14** [21]. In this case, copper centers are not in square planar coordination as seen for verdigris and copper resinate structures, but apical ligands have a stretched bond length while planar Cu-OH bonds have shorter bond lengths with respect to the perfect octahedral coordination.

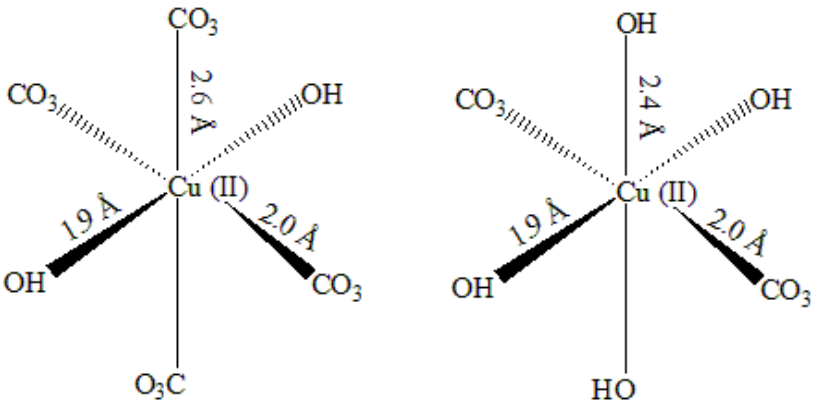

Figure 1.14: Malachite copper centers structures.

1.2 Binders

Binders are materials that permit to create a paste with pigments and spread the pictorial layer after some preparation steps. Binders have also the function to make color stick on the supporting material (paper, parchment, etc.). These compounds can be divided in three main categories according to their chemical composition: protein, lipid, and polysaccharide binders.

Protein binders are essentially protein aqueous solutions. The most used protein binders come from chicken eggs: the egg white (egg albumin) and the yolk. Very often, they are mixed to obtain the *tempera*. The main difference between egg white and yolk is in the fatty component: in the white there is no lipid component (see **Table 1.2**).

Components	Egg White (w/w %)	Yolk (w/w %)
Water	88	49
Solids	12	51
Proteins	10	16,5
Lipids	0	33
Carbohydrates	1	1
Inorganic component	0,6	1,7

Table 1.2: Egg white and yolk composition [18].

Animal glues are the second type of protein binder. They can be divided into two categories: strong glues (e.g., rabbit glue), not particularly pure and usually used as adhesive materials, and gelatins (e.g., fish glue), purer than strong glues and used to disperse pigments, often mixed with egg white.

Lipidic binders too can be divided into two categories: waxes and drying oils. Waxes are mixtures of saturated fatty acids, and their corresponding esters, with a large amount of high-weight hydrocarbons. Usually, waxes are in solid state at room temperature and are not soluble in water. The most used is *beeswax* (see **Table 3** and **Table 4** for its composition). Beeswax is produced by worker bees and then utilized by the hive bees to build cells for honey storage. Many studies were made about beeswax degradation processes in cultural heritage chemistry [18, 23].

Figure 1.15: Beeswax.

Components	Weight (%)
Hydrocarbons	14,0
Mono-esters	35,0
Di-esters	14,0
Tri-esters	3,3
Hydroxyl-mono-esters	3,6
Hydroxyl-poly-esters	7,7

Table 1.3: Beeswax composition [18].

Fatty acid	Weight (%)
C16:0	59,8
C18:0	2,6
C18:1	4,1
C20:0	1,5
C22:0	1,3
C24:0	11,9
C26:0	4,2
C28:0	4,3
C30:0	3,8
C32:0	3,2
C34:0	3,1
C36:0	0,2

Table 1.4: Fatty acids composition in beeswax (Cm: n; m= number of carbon in the chain, n= number of C=C double bonds) [18].

Drying oils are mixtures of unsaturated fatty acids and their esters. They are obtained by seeds squeezing. They also contain a variable fraction of phenols and tocopherols

(see **Table 1.5**). The most used drying oil is linseed oil, because of its properties: the high amount of linoleic acid that contains more C=C double bonds makes linseed oil fast to dry. On the other side, linseed oil films are prone to yellowing.

Drying oil	**C16:0 (w/w %)**	**C18:0 (w/w %)**	**C18:1 (w/w %)**	**C18:2 (w/w %)**	**C18:3 (w/w %)**
Linseed oil	7-8	3-5	19-23	14-17	52-55
Poppyseed oil	10-14	2-3	16-24	56-70	0,5
Walnut oil	6-7	1-2	14-26	57-62	10-15

Table 1.5: Composition of main drying oils (C18:3 = linoleic acid) [18].

Figure 1.6: Flax seeds.

Polysaccharide binders, like arabic gum, tragacanth gum, or starch, are polymers formed by condensation of monosaccharides like glucose, fructose, xylose. Polysaccharide binders are rich of OH groups, and because of that are very soluble in water. Starch is a polysaccharide widely present in seeds, cereals or tubers. As cellulose, starch is composed only by glucose units. It is found in nature as a mixture

of *amylose*, characterized by a linear chain of glucose, and *amylopectin*, with side chains of glucose. Gums are heteropolymers, formed by condensation of several six-carbon sugars, like glucose, arabinose, rhamnose, but containing also glucuronic acid, i.e., glucose oxidized at the C6. Both starch and gums were used as adhesive materials, or mixed in temperas.

Next paragraphs describe the binders used in the master's thesis work.

1.2.1 Rabbit Glue

Rabbit glue is a protein binder, belonging to the class of strong glues. The main component is the protein *collagen*, deriving from denaturation of collagen fibers from rabbit skin, bones, tendons, and nerves. Collagen fiber is not soluble in water due its compact structure, consisting of ordered and bound collagen molecules (**Figure 1.17**).

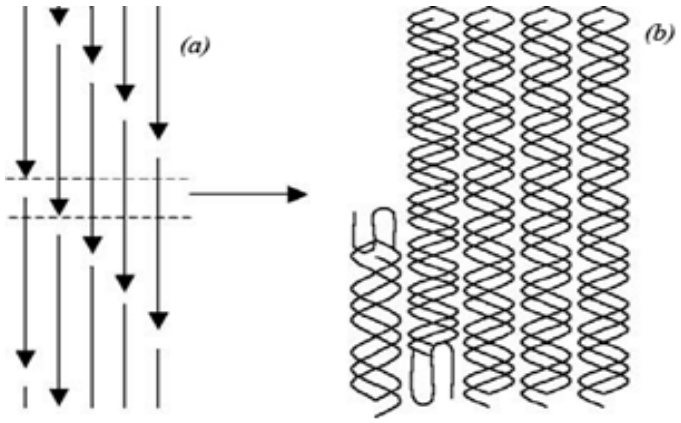

Figure 1.17: Collagen fibers structure.

In order to prepare the glue, the rabbit parts (skin, bones, etc.) are left in cold water and then heated up until a clear solution is formed. Once obtained the solution, it is cooled down and a gelatin formed (colloidal material): the glue.

In "*The Book of the Art*" [8], Cennino Cennini does not report a recipe for rabbit glue, but he describes a recipe for a goat glue:

"There is a glue called 'colla di spicchi', which is made of the clippings of the muzzles of goats, feet, sinews and many clippings of the skin. This glue is boiled with an equal quantity of water until it is reduced one-half and then put it in vessels. Let remain one night; the next morning cut it in slices, like bread, with knife"[***]

Essentially, its capability to form a pictorial layer is due to the formation of a colloidal material. In fact, once the glue (or glue-pigment mixture) is spread on the supporting material, water contained in the matrix evaporates: during evaporation hydrolyzed collagen molecules interact with each other (usually through Van der Waals interactions) to create a network. This process exposes some functional group to the action of external pollutants, with possible damage of the pictorial layer. Moreover, rabbit glue allows creating a hydrophilic layer because of chemical properties of denatured collagen: water-soluble components can easily interact with the matrix [22].

Collagen is also capable to bind with metal centers, in particular Cu (II) and Fe (III) [5]. It has been noted in many articles that these two metal centers catalyze the Fenton reaction, degrading the collagen structure and the pictorial film.

[***] *"E ell'è una cholla che ssi chiama cholla di spicchi, la quale si fa di mozzature di musetti di charavella, peducci, nervi e molte mozzature di pelli. Questa tal cholla si fa bollire tanto con acqua chiara, che torna men che per mezzo. Poi la metti in dei vasi. Lasciala stare una notte; poi la mattina, con choltello, le taglia a ffette chome di pane"*

1.2.2 Egg White

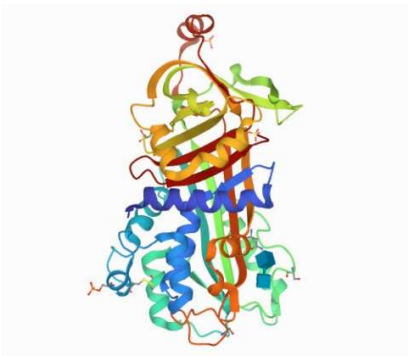

Figure 1.18: Ovalbumin 3D structure.

Egg tempera was more used than glues; in particular, egg white was the widest binder used for paintings. As said before, egg white is an aqueous protein solution. These proteins are ovalbumin (70% w/w of protein fraction), conalbumin (15% w/w of protein fraction), ovomucoid (12 % w/w of protein fraction) and lysozyme (3% w/w of protein fraction).

The "*De arte illuminandi*" [1] reports a recipe for preparing egg white as a binder:

"The chicken egg whites, that are the best, are so prepared: take fresh eggs, one, two or more according to the necessity; break them and extract the egg white separating them from the yolk. Put egg whites in a glass bowl and stir with a sponge until all egg whites are absorbed and squeeze the sponge. Repeat this operation several times until it flow as water"[†††]

There is also another recipe reported in "*De coloribus et de artibus Romanorum*" [9]:

[†††] *Clara ovorum gallinarum, que meliora sunt, sic fit. Recipe ova recentia, unum, duo vel plura, secundum quod opus fuerit, e frange caute, et extrae clara, et separa gallaturam ab eis, et vitellim cum ea non misceas; et mitte in scutella vitrea cum spongia et ducas tantum cum maninus donec tota clara recipiatur a dicta. Cum spongea donec non currat ut aqua."*

"If you want to prepare egg white, take a filter, and wet it with water. Take egg whites with water and filter them pressing it seven or eight times until the egg whites become like water"[‡‡‡]

Once mixed with pigments, the mixture is spread on the supporting material. The mechanism by which the pictorial layer is obtained is the same seen previously for the rabbit glue. As opposed to rabbit glue, egg white protein network becomes hydrophobic after water evaporation [18]. Because of that, egg white tempera was preferred.

1.2.3 Yolk

The yolk was even better than egg white to produce pigment tempera. In fact, due to the presence of fatty acids, the tempera obtained with yolk was highly hydrophobic. The pictorial layer, formed as seen for egg white and rabbit glue, is very strong, supple and not prone to yellowing: there is no high amount of linoleic acid [18].

The yolk is a water emulsion composed by phosphoproteins and lipids stabilized by lecithin. Its typical orange coloration is due to carotenoids.

Some recipes to obtain yolk are included in some illuminated manuscripts. For example, in "*De coloribus et artibus Romanorum*" [9] is reported that:

"*Take the yolk in your hand palm, sting it with a spine, and squeeze it in a vessel adding some water"*[§§§]

[‡‡‡] *"Glaream paraturus sum staminium, et in aqua intinge illud, et maddidum sit, ut postea glaream acquae mixtam, in eodem staminio duplicato, et sic exprimendo fac transire vel septies vel octies, tandium sciliet debes hoc facere, donec glarea quasi aqua fit."*

[§§§] *"Sume vitellum in media manu, et spunge vel spina, exprime, et in vase recipe mittens guttam acquae."*

The yolk was very often mixed up with the egg white removing yolk membrane. Moreover, it was added also some wine or vinegar (ethanol) to avoid degradation processes.

1.2.4 Linseed Oil

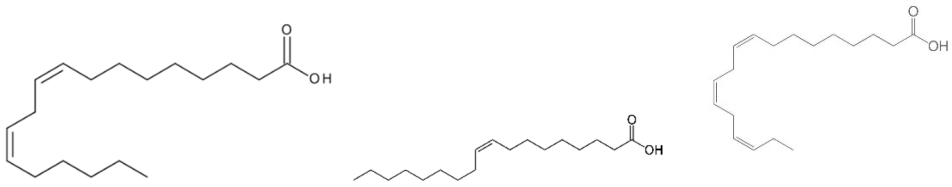

Figure 1.19: Linoleic, oleic and linoleic acid structures.

The linseed oil was one of the most used drying oils during Renaissance. It was already known its tendency to yellowing, and consequently the walnut oil was preferred. The linseed oil was obtained by cold squeezing of *linus usitutissimum* seeds. Romans already used this oil in paintings, but only in the XV century, it became widely used all over the Europe, also thanks to Jan Van Eyck, a pioneer and master of the oil technique [18]. The oil technique replaced the tempera, due to a better control of the pictorial stroke, with a better rendering, and a more vivid color palette.

The main chemical components of linseed oil are the linoleic acid, the oleic acid, and the linolenic acid (see **Table 1.5**). In fact, the C=C bonds are the reactive sites of the chain and there are two double bonds in linoleic acid, one in the oleic acid and three in the linolenic acid (main component).

The formation of the pictorial layer has a completely different mechanism from protein binders. In fact, the linseed oil consists of low-weight fatty acids, isolated or in triglyceride form, i.e., in the form of glycerol esters. The film forms through cross-

linking of the alkyl chains in the triglycerides, due to radical polymerization reaction promoted by reactive oxygen species (ROS): these species catalyze a radical reaction at C=C active sites through an epoxide intermediate. So formed radicals add to other C=C sites to create high-weight macromolecules that form a solid network at room temperature [18]. Metal ions, like copper, iron or lead, play also a relevant role in catalyzing radical polymerization, which was also known to the Renaissance painters [8].

Linseed oil is very prone to yellowing. This process is not yet fully understood, but it is supposed the formation of diketones by fatty acid oxidation, or the formation of pyrrole compounds [18].

The linseed oil mixtures are also prone to saponification catalyzed by metal ions in a basic pH environment. Saponification of triglycerides produces a molecule of glycerol and three molecules of fatty acid, a mixture which is a liquid a room temperature. With Cu(II), Fe(III) or Pb(II) ions, free fatty acids give rise to stable complexes, and/or insoluble organic salts. E.g., verdigris is known to promote the formation of Cu(II)-fatty acid complexes.

1.2.5 Arabic Gum

Figure 1.20: Exudate of Arabic gum.

Arabic gum is the exudate of many Acacia species, the *Acacia Senegal* being the most relevant species for arabic gum production. The arabic gum is a water-soluble and water-dispersive material.

The main components of the arabic gum are high-weight polysaccharides composed by chains of arabinose, galactose, rhamnose and salts of glucuronic acid. In general, gums contain a core strand of uronic acid units and one or two types of monosaccharide. Attached to the main chain there are sidechains that are usually composed by six units. Therefore, gum composition changes according to which kind of tree is used [18] (see **Table 6**)

Gums	**Arabinose**	**Rhamnose**	**Galactose**	**Glucose**	**Mannose**	**Xylose**	**Glucuronic acid**
Arabic Gum	++	+	++				+
Cherry Gum	++		+		+	+	+

Table 1.6 Sugar composition of cherry gum and Arabic gum (+: indicates that the sugar is present; ++: major component) [18].

Due to the uronic acid content, gums exhibit a pH around 5.0. The low pH could promote acid hydrolysis of the polysaccharide chains, but in dry state hydrolysis reaction ceases, since water is almost completely removed. In this condition, arabic gum appears to be stable at least for two millennia, according to literature investigations [22]. Most gums, in particular Arabic gum, does not degrade supporting material as paper.

The stability of glycosidic bonds to acid hydrolysis depends also on the monosaccharide composition of the polysaccharide chain. The condensation bonds of

furanose units in the sidechains are very prone to hydrolysis in acid environment [22]. On the opposite, stronger conditions (lower pH and higher temperatures) are needed to break the bonds between an uronic acid and a monosaccharide, which are the most common monomers in the main polysaccharide chain (core chain). Therefore, the core chain is highly stable, whereas sidechains are more prone to hydrolysis [22].

Chapter 2: Theoretical introduction to CW-EPR experiments

2.1 EPR Spectroscopy Theory

The Electron Paramagnetic Resonance Spectroscopy (EPR, also named ESR, Electron Spin Resonance) is a widely used technique to study paramagnetic systems, like, e.g., free radicals, triplet excited states, bi-radicals, transition metal complexes or electronic-localized defects in solids. It is based on the possibility to induce transitions between spin levels separated in energy by an external magnetic field (*Zeeman Effect*).

Each electron has a dipolar moment $\vec{\mu}$ directly proportional to angular momentum $\vec{S}$ according to **Eq. 2.1**:

$$\vec{\mu} = -g_e \mu_B \vec{S} = \gamma_e \vec{S} \qquad \textbf{Eq. 2.1}$$

Where g_e is the g-factor of a free electron, μ_B is the Bohr magneton ($\mu_B = 9{,}274\ 10^{-24}$ JT^{-1}) and γ_e is gyromagnetic ratio.

Angular momentum $\vec{S}$ is quantized along the z-axis, called quantization axis. $\vec{S}_z$ can have two positions as shown in **Figure 2.1** related to two different spin states ($S_z = m_s\hbar$, $m_s = \pm\frac{1}{2}$): α and β states.

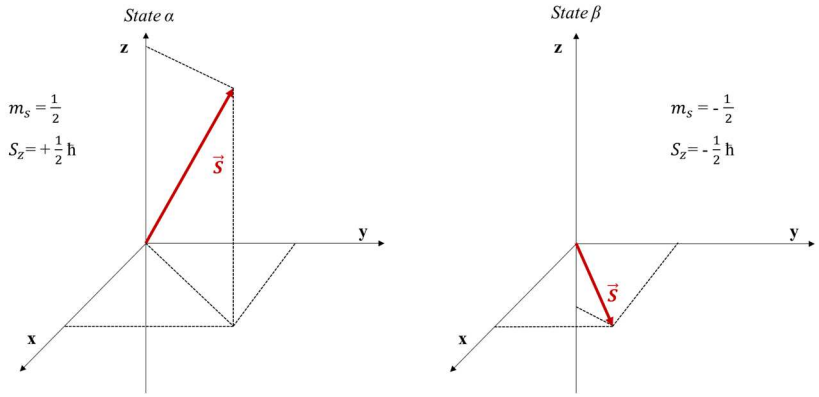

Figure 2.1: spin states α and β.

Without an external magnetic field, indicated as $\vec{B}_0$, these two states are degenerate. When a magnetic field $\vec{B}_0$ is applied along the *z*-axis, the degeneration is removed because of the interaction between $\vec{\mu}$ and the external magnetic field, so called Zeeman interaction. A Spin-Hamiltonian operator can express every interaction in a magnetic system. In the presence of the only magnetic field, the corresponding Spin-Hamiltonian is $\hat{H}_z$ (Zeeman Hamiltonian operator), whose expression is reported below (**Eq. 2.2**):

$$\hat{H}_z = -\hat{\mu}_z\vec{B}_0 = g_e\gamma_e B_0\hat{S}_z \qquad \textbf{Eq. 2.2}$$

By applying this operator to the spin eigenfunctions $|\alpha\rangle$ and $|\beta\rangle$, two energy states are obtained (**Eq. 2.3**):

$$E = \pm\frac{1}{2} g_e\mu_B B_0 \qquad \textbf{Eq. 2.3}$$

Therefore, between two energy states there is an energy gap $\Delta E = g_e\beta_e B_0$, dependent on external magnetic field intensity. The resonance condition has to be fulfilled to induce spin transitions, therefore the frequency of an electromagnetic wave must have a frequency ν, such as $\Delta E = h\nu = g_e\beta_e B_0$ (**Figure 2.2**).

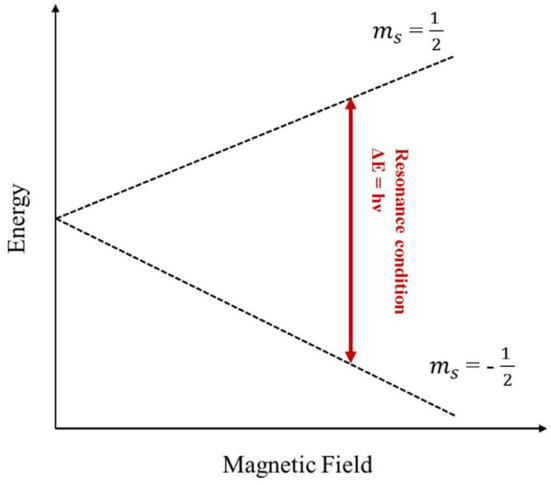

Figure 2.2: Zeeman Effect for the electron.

In an EPR sample, many electron spins are distributed between state α and state β. When there is no external magnetic field, the two states are equally populated. When a field B_0 is applied, degeneration is removed and the two states are no more equally populated: the state β (lower energy) has a slightly bigger population than the state α according to Boltzmann distribution law (**Eq. 2.4**):

$$\frac{N(\alpha)}{N(\beta)} = \exp\left(- g_e \mu_B B_0 / k_B T\right) \qquad \textbf{Eq. 2.4}$$

where k_B is the Boltzmann constant ($1.3806 \cdot 10^{-23}$ JK^{-1}) and T is the absolute temperature expressed in Kelvin. Defining the magnetization vector $\vec{M}$ as the sum of all the electron spin magnetic moments per volume, the absolute value of this quantity is different from zero and its direction is along the quantization axis z. This difference in population allows one to observe EPR transitions induced by the oscillating magnetic field of a radiation

2.2 EPR spectral parameters

An EPR spectrum gives a lot of information about the studied paramagnetic center. Until here, the g-factor has been associated to a free electron: the simplest case. Actually, the g-factor is specific for a certain species and does depend on its molecular surrounding. Therefore, its value deviates from the free electron value g_e, due to spin-orbit interaction. Spin-orbit interaction is anisotropic, so it depends on the orientation of the paramagnetic center with respect to the external magnetic field B_0. For this reason, g is described well as a tensor. **Eq. 2.2** becomes:

$$\hat{H}_z = \mu_B \vec{B}_0 \cdot \tilde{g} \cdot \hat{S}_0 \qquad \textbf{Eq. 2.5}$$

When the paramagnetic species reorientation is fast, the g-tensor averages to a scalar quantity, the g-factor. The paramagnetic center (unpaired electron) could also interact

with local magnetic fields generated by other magnetic nuclei (transition metals, ^{1}H, ^{13}C, ^{14}N). If an electron spin magnetic moment interacts with *n* equivalent nuclei, *2nI+1* transitions could be possible (*I* is the nuclear spin quantic number). Each transition is separated one from another by a constant called hyperfine constant A. The hyperfine constant too is anisotropic and described by a tensor, averaged to a scalar in case of fast molecular reorientation. The hyperfine Hamiltonian can be described as:

$$\widehat{H}_{\text{hyperfine}} = \hat{S} \cdot \tilde{A} \cdot \hat{I} \qquad \textbf{Eq. 2.6}$$

There is another important interaction to consider: the electron spin-spin interaction, which is established between two electron spins (described by the operators $\hat{S}_1$ and $\hat{S}_2$). Species containing two paramagnetic centers usually show EPR signals due to electron spin-spin interaction. This interaction is scalar, and the spin-spin Hamiltonian operator can describe it:

$$\widehat{H}_{\text{ex}} = -2J\hat{S}_1 \cdot \hat{S}_2 \qquad \textbf{Eq. 2.7}$$

J is an isotropic scalar constant. J>0 corresponds to a ferromagnetic coupling and J<0 corresponds to an antiferromagnetic coupling. The effect of $\widehat{H}_{\text{ex}}$ is to separate the degenerate ground single-spin states into spin-coupled states at different energy: e.g., two electronic spins with S=$\frac{1}{2}$ give rise to two coupled spin states S=1 and S=0. An S=1 spin state is characterized by three degenerated energy levels with M_s = ±1, 0. A zero-field-splitting Hamiltonian describes the splitting of these degenerate levels:

$$\widehat{H}_{\text{ZFS}} = D\left(\hat{S}_z^2 - \frac{1}{3}S(S+1)\right) + E\left(\hat{S}_x^2 - \hat{S}_y^2\right) \qquad \textbf{Eq. 2.8}$$

D and E represent the axial and non-axial components of the zero-field-splitting, respectively. The full spin Hamiltonian operator is:

$$\hat{H} = \hat{H}_Z + \hat{H}_{hyperfine} + \hat{H}_{ex} + \hat{H}_{ZFS} \qquad \textbf{Eq. 2.9}$$

2.3 CW-EPR experiment

The conventional CW-EPR experiment is performed with a magnetic field of 0.35 T, by exciting the sample with microwave radiation in the X-band range (frequency ν = 9.5 - 10 GHz) at low intensity (P_{max} = 200 mW). In the CW-EPR experiment, the microwave frequency is kept constant, while the magnetic field is swept : when the spin level splitting matches the radiation energy (see **Figure 2.2**), microwave radiation is absorbed and an EPR transition happens.

2.4 CW-EPR instrumentation

A CW-EPR instrument is composed by an electromagnet, a microwave source, a resonant cavity, where the sample is put in, a detector and system of signal acquisition.

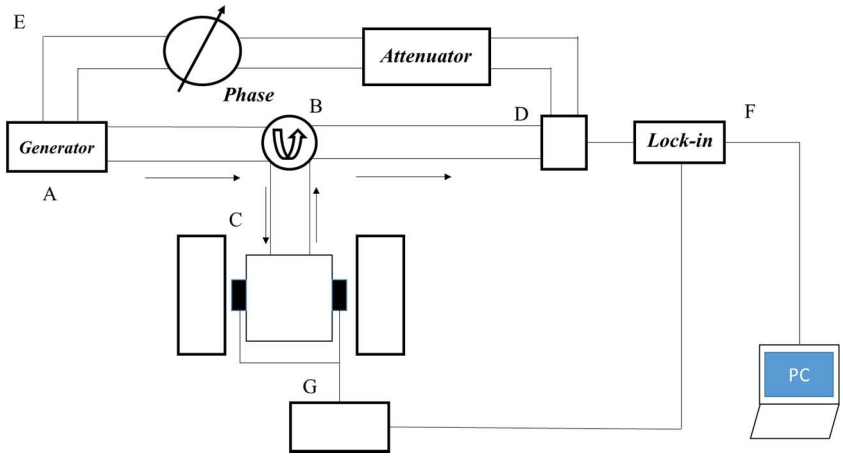

Figure 2.3: CW-EPR instrumentation block diagram.

As shown in **Figure 2.3**, the generator A, that is usually a Gunn diode or a Klystron oscillator, generates microwaves. Microwaves travel through waveguides up to the circulator B, which direct them to the cavity C. The cavity has a particular shape, and can be tuned to reach a condition called “critical coupling”, where the impedance of

cavity and waveguide is identical: in this particular situation, microwaves are trapped in the resonant cavity and no microwaves are reflected back to the waveguide. When the sample is on resonance, a transition happens, changing the cavity impedance: consequently, the critical coupling regime is broken and reflected microwaves are generated. This radiation travels through the waveguide to the circulator B, which direct it to the detector D (usually, a Schottky diode) that converts the radiation into a current directly proportional to the wave amplitude. For low microwave powers, the reflected radiation is proportional to the absorbed radiation, and therefore, the current is proportional to the sample microwave absorption. If the signal were collected with no other operation, the signal-to-noise ratio ($\frac{S}{N}$) would be very low. To improve $\frac{S}{N}$ the signal is modulated by an oscillating small magnetic field (modulation field) added to the swept magnetic field. The modulation coils G, placed on the outer side walls of the resonant cavity, generate a small oscillating magnetic field (0.1-1 mT), normally set to a frequency of 100 KHz. Consequently, also the signal current going out from the detector is now modulated at 100 KHz. The lock-in amplifier F is a frequency filter which passes only currents in a narrow band around the modulation frequency, getting rid of other currents. In this way, the lock-in enhances only the signal with the same modulation frequency, reducing the random noise, and the $\frac{S}{N}$ is very improved.

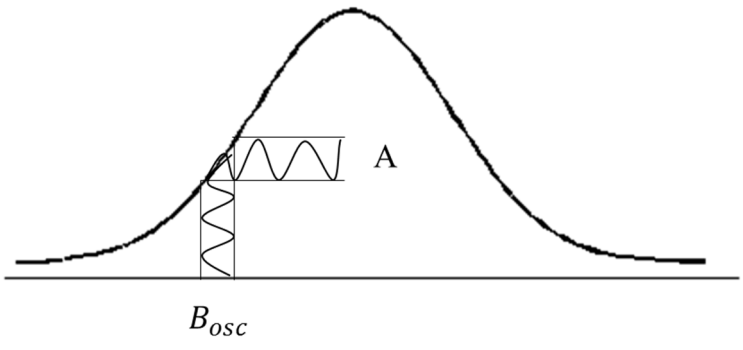

Figure 2.4: Oscillating magnetic field (B_{osc}) and output signal (A).

Because of this kind of detection system the output signal is the first derivate of the absorption profile. The absorption spectrum could be obtained, in principle, by integrating the derivative signal, but actually, EPR spectra are not shown in integrated mode, because spectral resolution is better in first derivative mode.

2.5 CW-EPR characteristics of Cu(II) complexes signal

Cu(II) ion (d^9) has an unpaired electron ($S=\frac{1}{2}$). In nature, there are two stable copper isotopes: ^{63}Cu (69.2%) and ^{65}Cu (30.8%). The nuclear spin quantum number of copper nuclei is $I=\frac{3}{2}$ for both isotopes. For a single Cu(II) center, CW-EPR spectrum (**Figure 2.5**) shows a peculiar quartet ($2I+1=4$) centered at lower fields, due to hyperfine coupling between the unpaired electron and the copper nucleus and a more intense signal at higher fields. This kind of signal suggests that the g and A tensors are axial and collinear. Therefore, the lower field signal is centered at the parallel g-value ($g_{//}$) and the higher field signal is centered at the perpendicular g-value ($g_{\perp}$). Two consecutive lines in the quartet are separated by a distance called parallel hyperfine constant ($A_{//}$). The parameters $g_{//}$ and $A_{//}$ are related to the type of copper coordination. Therefore, from these values copper coordination in the complex can be understood [24]. Experimental spectra must be simulated to obtain accurate values of these parameters.

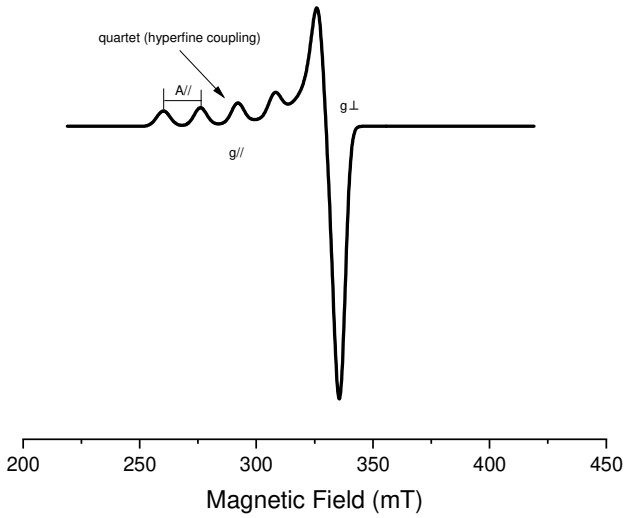

Figure 2.5: CW-EPR copper signal.

In the case of a copper dimer, the total Hamiltonian includes also $\widehat{H}_{ex}$ and $\widehat{H}_{ZFS}$. Therefore, other signals could appear in the experimental spectrum. The shape and position of dimer signals strongly depends on the parameters J, E and D, that are mainly influenced by dimer orientation with respect to the external magnetic field. The temperature also plays a significant role in the EPR spectrum. Usually, a copper dimer in an X-band experiment shows three kinds of signals: two at higher fields and one at lower field, as shown in **Figure 2.6**. The signals at higher fields correspond to two main orientations: defining Θ the angle between the Cu-Cu axis and the external magnetic field, one corresponds to Θ = 90° and the other one to Θ = 0°. The lower field signal corresponds to a forbidden transition only observable at low frequency (X-band).

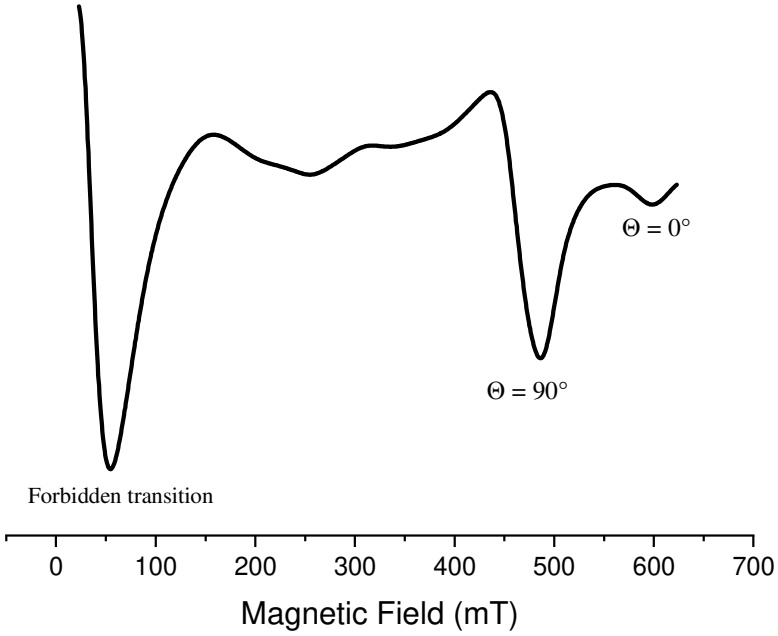

Figure 2.6: CW-EPR copper dimer signal (X-band).

2.6 CW-EPR characteristics of Fe(III) complexes signal

Fe(III) ion (d^5) usually form octahedral high-spin complexes. Therefore, it has five unpaired electrons ($S=\frac{5}{2}$). The EPR signal of Fe(III) (**Figure 2.7**) is strongly related to the symmetry of complex: in a pseudo octahedral environment, a broad, symmetric line centered at 200-400 mT (g = 2.0) is formed, while in a distorted rhombic environment a sharp, symmetric signal centered at 150-160 mT (g = 4.3) is observed [25]. Therefore, g factor values are very slightly dependent on the complex orientation.

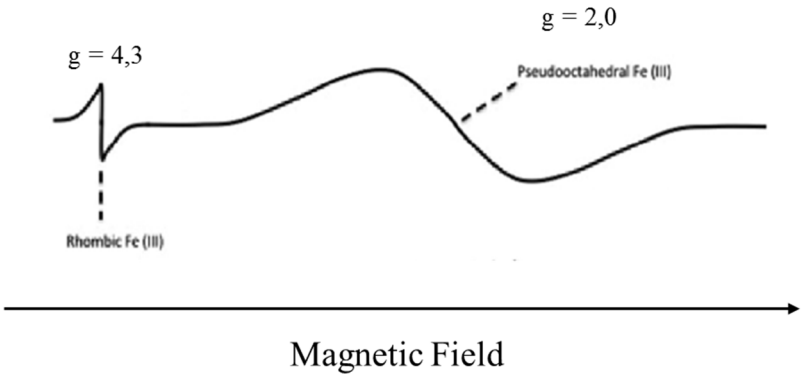

Figure 2.7: CW-EPR Fe(III) signal.

2.7 CW-EPR characteristics of Mn (II) complexes signal

Mn (II) ion (d^5) shows a typical EPR signal due to hyperfine coupling with ^{55}Mn nuclei ($I = \frac{5}{2}$): it is characterized by a six-line pattern centered at 300-400 mT (g = 2.0), as shown in **Figure 2.8**. The shape of each line in the pattern is very sensitive to the type of Mn (II) coordination. Mn (II) signal g value is almost isotropic and only slightly dependent on complex orientation.

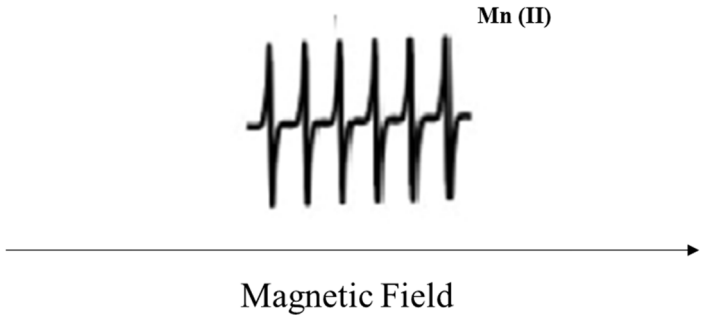

Figure 2.8: CW-EPR Mn(II) signal.

Chapter 3: Samples and methods

3.1 Materials

The pigments and binders used during master's thesis work are listed in table below (**Table 3.1**). Pigments and binders were bought from the following suppliers: Zecchi (IT), Maimeri (IT), Kremer Pigmente (DE) and Winsor & Newton (EN). Other materials utilized during the work are listed in the same table.

Name	Product Codex	Supplier	Supplier comments
Pigments			
Verdigris	0997	Zecchi	Basic copper acetate
Synthetic Verdigris	44450	Kremer	Monohydrated copper acetate
Copper Resinate	3120	Zecchi	Verdigris in natural resins
Natural Light Malachite	0104S	Zecchi	-
Synthetic Malachite	44400	Kremer	-
Natural Azurite	0107-M	Zecchi	Finely grinded
Synthetic azurite	10180	Kremer	Brema blue or Bice blue
Binders			
Arabic Gum	3022906	Winsor & Newton	Diluted with water
Rabbit glue (collagen)	2831	Zecchi	-
Linseed Oil	5816650	Maimeri	-
Chicken eggs (Egg white and Yolk)	-	Local Market	-
Solvents			
Ethanol (CH_3CH_2OH)	V001229	Sigma-Aldrich	95%
Acetic acid (CH_3COOH)	XA-0300-500	Prolab	99,8%

Table 3.1: Materials: pigments, binders, and solvents.

3.2 Preparation

Samples were prepared according to recipes found in the ancient manuscripts previously cited [1,7,8].

First step was preparation of binders. The following points describe each binder preparation:

- *Egg white*: Egg white was separated from yolk and poured in a beaker. It was stirred and filtered through wet filter paper four times until ideal viscosity [9]. Then, 3 mL of ethanol were added to preserve mixture from degradation.
- *Yolk*: Yolk was separated from egg white. After piercing yolk membrane, the yolk was squeezed out in a beaker and stirred to obtain an emulsion. Then, 3 mL of ethanol were added to preserve mixture from degradation.
- *Egg white and yolk mixture*: Yolk and egg white coming from the same egg were put in a beaker. The yolk was squeezed out from its membrane. The mixture was stirred to obtain an emulsion, and then 3 mL of ethanol were added to preserve emulsion from degradation.
- *Rabbit glue*: 10 g of dry rabbit glue were put in a beaker and 100 mL of distilled water were added to completely immerse the glue. The rabbit glue was immersed in water for 48 hours. The glue absorbed water and its volume increased. The mixture was heated 30 minutes in water bath at temperature oscillating between 50 and 60°C. A clear solution was obtained. The solution was cooled down at room temperature for 30 minutes. Before every usage, the solution was heated in a water bath.
- *Linseed oil*: the binder bought from Maimeri was exposed to light to promote oil pre-polymerization, as usually done in the ancient recipes [1].

As a second step, pigments were ground in an agate mortar. Pigments were ground with no other operation but for verdigris that was ground with the addition of acetic acid solution (10%, a few drops), according to Cennini recipe [8].

Figure 3.1: Ground pigment-binder mixture in an Agate mortar.

Two kind of samples were prepared for Zecchi pigments: one with a 1:3 w/w pigment/binder ratio and the other one with a 5% w/w pigment/binder ratio.

The ground pigment and the binder were mixed in the mortar and the mixture was ground again (**Figure 1**). The mixture obtained was spread on filter paper to simulate painting conditions (**Figure 2**).

Figure 3.9: Mixture painted on a filter paper.

The colored filtered paper was exposed to the air for at least four days until complete drying of the sample. The samples are listed in **Table 3.2**, **Table 3.3** and **Table 3.4**.

Sample name	Composition	Weight (mg)
Verdigris Zecchi (VR)	Verdigris	15,1
Copper Resinate Zecchi (RR)	Copper Resinate	24,8
Light Malachite Zecchi	Light Malachite	31,0
Azurite Zecchi	Azurite	19,4

Table 3.2: Raw pigment samples (Zecchi).

Sample name	Composition	Weight (mg)
VRO	Verdigris + Linseed oil	16,6
VRC	Verdigris + Rabbit Glue (collagen)	19,6
VRG	Verdigris + Arabic gum	11,6
VREW	Verdigris + Egg white	31,5
VRY	Verdigris + Yolk	26,4
VREY	Verdigris + Egg white & Yolk	34,0
RRO	Copper Resinate + Linseed oil	22,9
RRC	Copper Resinate + Rabbit Glue (collagen)	10,5
RRG	Copper Resinate + Arabic gum	9,9
RREW	Copper Resinate + Egg white	8,3
RRY	Copper Resinate + Yolk	46,0
RREY	Copper Resinate + Egg white & Yolk	1,2
LMO	Light Malachite + Linseed oil	12,1
LMC	Light Malachite + Rabbit Glue (collagen)	26,4
LMG	Light Malachite + Arabic gum	11,9
LMEW	Light Malachite + Egg white	18,5
LMY	Light Malachite + Yolk	20,3
LMEY	Light Malachite + Egg white & Yolk	68,5
AZO	Azurite + Linseed oil	59,9
AZC	Azurite + Rabbit Glue (collagen)	10,7
AZG	Azurite + Arabic gum	19,8
AZEW	Azurite + Egg white	26,0
AZY	Azurite + Yolk	31,4
AZEY	Azurite + Egg white & Yolk	37,6

Table 3.3: List of 1:3 w/w pigment/binder ratio samples (Zecchi).

Sample name	Composition
VRO5	Verdigris + Linseed oil
VRC5	Verdigris + Rabbit Glue (collagen)
VRG5	Verdigris + Arabic gum
VREW5	Verdigris + Egg white
VRY5	Verdigris + Yolk
VREY5	Verdigris + Egg white & Yolk
RRO5	Copper Resinate + Linseed oil
RRC5	Copper Resinate + Rabbit Glue (collagen)
RRG5	Copper Resinate + Arabic gum
RREW5	Copper Resinate + Egg white
RRY5	Copper Resinate + Yolk
RREY5	Copper Resinate + Egg white & Yolk
LMO5	Light Malachite + Linseed oil
LMC5	Light Malachite + Rabbit Glue (collagen)
LMG5	Light Malachite + Arabic gum
LMEW5	Light Malachite + Egg white
LMY5	Light Malachite + Yolk
LMEY5	Light Malachite + Egg white & Yolk
AZO5	Azurite + Linseed oil
AZC5	Azurite + Rabbit Glue (collagen)
AZG5	Azurite + Arabic gum
AZEW5	Azurite + Egg white
AZY5	Azurite + Yolk
AZEY5	Azurite + Egg white & Yolk

Table 3.4: List of 5% w/w pigment/binder ratio samples (Zecchi).

For synthetic pigments (Kremer Pigmente), only one kind of samples was prepared: the one with 5% w/w pigment/binder ratio. Only two binders were used: the linseed oil and the rabbit glue. The preparation protocol was the same described above for Zecchi pigments. The samples are listed in **Table 3.5** and **Table 3.6**.

Sample name	Composition	Weight (mg)
Verdigris Kremer (SVR)	Synthetic Verdigris	13,2
Light Malachite Kremer (SLM)	Synthetic Light Malachite	12,9
Azurite Zecchi (SAZ)	Synthetic Azurite	14,7

Table 3.5*:* Raw pigment samples (Kremer).

Sample name	Composition	Weight (mg)
SVRO5	Synthetic Verdigris + Linseed oil	-
SVRC5	Synthetic Verdigris + Rabbit Glue (collagen)	-
SLMO5	Synthetic Light Malachite + Linseed oil	-
SLMC5	Synthetic Light Malachite + Rabbit Glue (collagen)	-
SAZO5	Synthetic Azurite + Linseed oil	-
SAZC5	Synthetic Azurite + Rabbit Glue (collagen)	-

Table 3.6: List of 5% w/w pigment/binder ratio samples (Kremer).

3.3 CW-EPR experiments

EPR tubes were prepared to perform CW-EPR experiments. For the sample with 1:3 w/w pigment/binder ratio, the dried mixtures were scraped at surface to obtain a powder and put in the tube (see **Figure 3.3**). The amount (in mg) of powder introduced in each EPR tube is reported in **Table 3.2** and **3.3**. For the samples with 5% w/w pigment/binder ratio, this kind of operation was practically impossible. It was cut a piece of paper where the mixture was located and put into the EPR tube.

EPR experiments were performed at room temperature and at 250K, 210K, 180K and 150K (nitrogen flux to cool down the system) with an X-band (~9,5 GHz) spectrometer equipped with 4106 TMH cavity and an ER4111VT control unit (temperature control unit). Baseline correction was applied to the spectra. Simulations were performed with the EasySpin software [26]. The dimer signals were simulated as a spin system with S=1, while monomer signals were simulated as a spin system with S=1/2.

Figure 3.3: EPR tube with powder sample.

```
n_spec=2; %numero di specie di rame
nomefile=['RRPURO_RT_ZOOM.dat'];
z=load(nomefile,'-ascii');
x=z(:,1);
y=z(:,2);
ynrm=abs(max(y)-min(y));
plot(x/10,y/ynrm);
hold on;
g{1}=[2.06 2.06 2.27]
A{1}=[58 34 540] %MHz
lw{1}=[1.0 6.0] %mT
gStrain{1}=[0.005 0.005 0.01]
AStrain{1}=[0.5 0.5 1.0] %MHz
g{2}=[2.06 2.06 2.33]
A{2}=[58 34 470]
lw{2}=[1.0 6.0] %mT
gStrain{2}=[0.005 0.005 0.01]
AStrain{2}=[0.5 0.5 1.0] %MHz
Sys.S=1/2
Sys.Nucs='Cu'
Exp.mwFreq=9.539383
Exp.Temperature= 300
Exp.CenterSweep=[319 200]
```

```
n_spec=1; %numero di specie di rame
nomefile=['RRPURO_RT.dat'];
z=load(nomefile,'-ascii');
x=z(:,1);
y=z(:,2);
ynrm=abs(max(y)-min(y));
plot(x/10,y/ynrm);
hold on;
g{1}=[2.05 2.05 2.30]
A{1}=[15 15 200] %MHz
lw{1}=[3.0 20.0] %mT
gStrain{1}=[0.08 0.08 0.]
AStrain{1}=[0.5 0.5 100] %MHz
% g{2}=[2.05 2.1 2.25]
% A{2}=[50 50 390]
% lw{2}=[5.0 0.0] %mT
% gStrain{2}=[0.005 0.005 0.03]
% AStrain{2}=[0.05 0.05 100] %MHz
Sys.S=1
Sys.Nucs= 'Cu'
Sys.D= [9900 175]
Exp.mwFreq=9.537359
Exp.Temperature= 300
Exp.CenterSweep=[323 650]
```

Figure 3.4: EasySpin simulation parameters.

3.4 ATR-IR experiments

ATR-IR experiments were carried out with a Thermo Nicolet Nexus 870 ESP FT-IR/NIR in ATR mode. The experiments were performed on the powder samples for pure pigments, while were performed on the pictorial layer spread on the filter paper for binder-pigment mixtures. Backgrounds were acquired in the following way: binders alone were spread on the filter paper and then experiments were performed. All the spectra were acquired with the following parameters: 4 cm^{-1} of spectral resolution, 32 scans for run time in a wavenumber range between 4500 and 500 cm^{-1}. All the spectra of the pictorial layers are reported as "absorbance difference", i.e., then were corrected for the background signal represented by the binder + paper signal. In this way, only signals from pigments and possible pigment+binder complexes, were detected.

3.5 XRF experiments

Kremer and Zecchi pigments were analyzed by XRF technique. The powder pigments were placed over a piece of filter paper and analyzed. XRF experiments were performed with a Bruker ARTAX^{TM} 200. A Coolidge X-Ray tube with Mo anode was used. Voltage was set to 45 kV and tube current 0.705 mA, with 3 min. scan for each measurement.

Chapter 4: Results

The experimental results are reported in this chapter pigment by pigment. For each pigment, the results are presented for the pure pigment alone, and as a comparison for the different pigment-binder mixture, both in ratio 1:3 and at 5% w/w pigment/binder.

4.1 Verdigris

4.1.1 Raw pigment (VR and SVR samples)

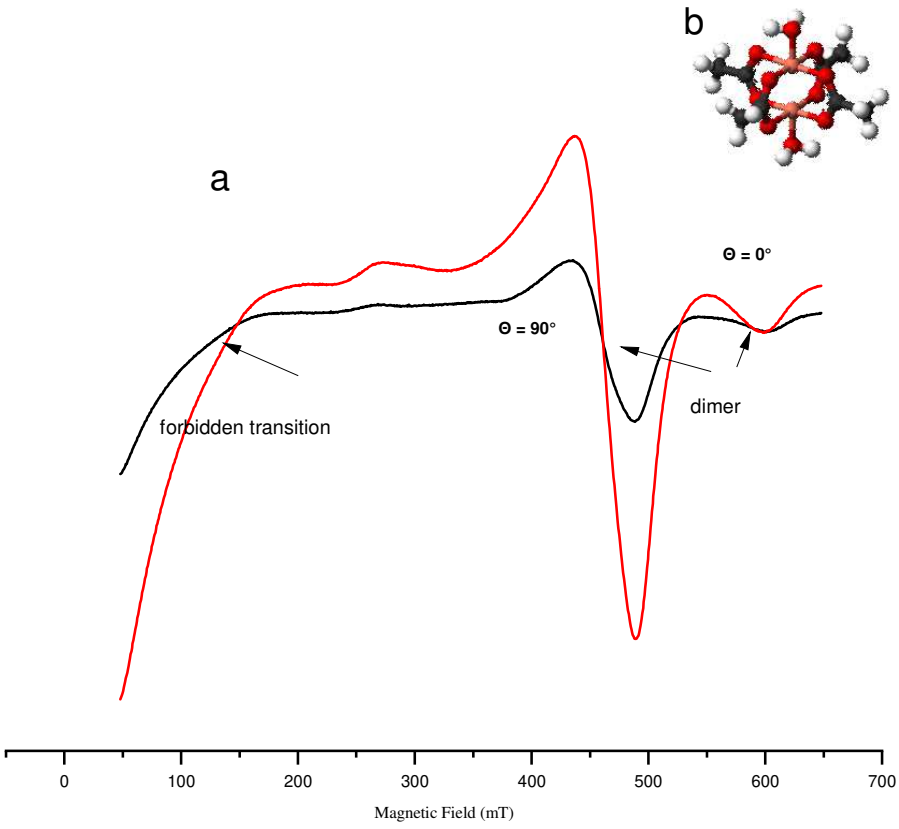

Figure 4.1: a) CW-EPR spectra (X-band) of VR (black line) and SVR (red line), b) copper acetate 3D structure.

As shown in **Figure 4.1**, the CW-EPR powder spectra of the Zecchi verdigris (VR sample, black line) and of the synthetic verdigris (SVR sample, from Kremer, red line) have three main signals: the first one in the 100-140 mT spectral region, the second one at 450 mT and the third one at 600 mT. As described in **Chapter 1**, the verdigris pigment (copper acetate) is characterized by a bimetallic carboxylate complex. The

two paramagnetic ions Cu(II), with S=1/2, interact magnetically, with ferromagnetic coupling, generating a dimeric species with S=1. The features of the EPR spectrum, with a line at very low field (100-140 mT), and a line at high field (450 mT), with a minor component at 600 mT, are indicative of a *triplet state* species (i.e., S=1 species), as it is the dimeric species in verdigris. As discussed in Chapter 2, section 2.5, the low-field component corresponds to a forbidden transition, which is observed only in the low-field regime (in the conventional X-Band EPR). The second and third signal correspond to features resulting from the different orientation of the Cu(II)-Cu(II) bond axis with respect to the external magnetic field (see **paragraph 2.5**). The spectrum also shows a shallow signal at 270 mT, of not clear origin. The synthetic copper acetate was brought by another supplier (Kremer) to evaluate differences and similarities with the Zecchi pigment. The SVR sample (red line in **Figure 4.1**) shows the same EPR features. The two spectra do not show other EPR signals. An XRF experiment was performed to rule out the presence of other metals that could give EPR signals (see **Figure 4.2** and **Figure 4.3**) for both VR and SVR samples.

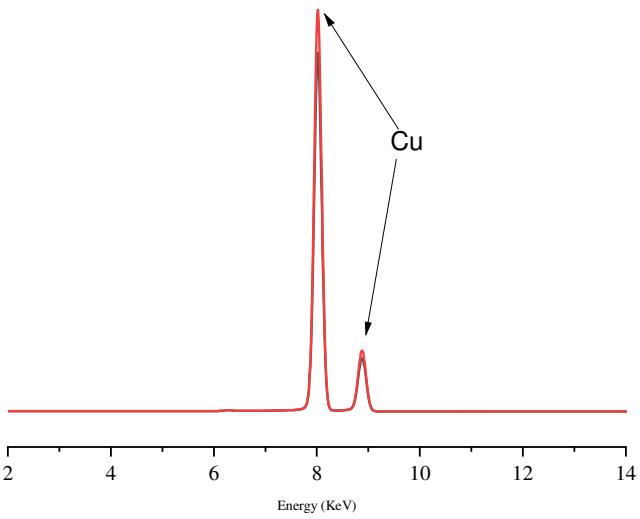

Figure 4.2. XRF spectrum of VR sample.

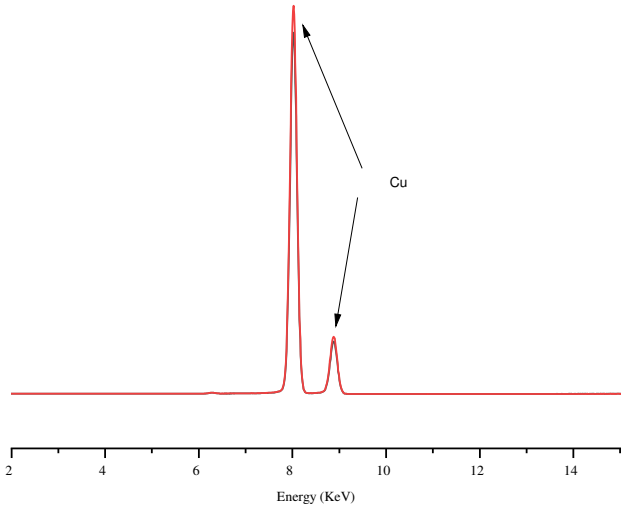

Figure 4.3. XRF spectrum of SVR sample.

Both VR and SVR XRF spectra show only signals of copper. Therefore, in the limit of XRF sensitivity, signals coming from other metallic paramagnetic centers are excluded.

The VR experimental spectrum was simulated with the EasySpin software to collect the main magnetic parameters describing the copper dimer. **Figure 4.4** shows the experimental (blue line) and simulated (red line) spectra of VR. The simulation parameters are reported in **Table 4.1**.

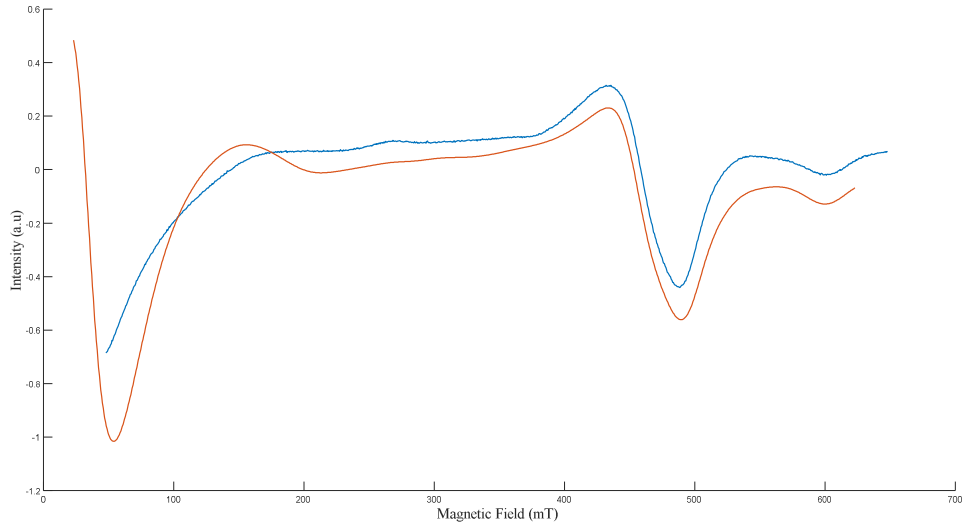

Figure 4.4. VR sample: simulated spectrum (red line) and experimental spectrum (blue line).

The simulated spectrum is quite well matched with the experimental one in the spectral region between 350 and 620 mT. A small feature at 270 mT is also reproduced in the simulation, although not as strong as in the experimental spectrum.

Sample	$g_{//}$	$g_{\perp}$	$A_{//}$ (MHz)	$A_{\perp}$ (MHz)	D (MHz)	E (MHz)
VR	2.37	2.07	200	15	10342	310

Table 4.1 Simulation parameters of the VR spectrum.

These parameters agree with those reported by Binet and co-workers [16].

The SVR experimental spectrum was simulated with EasySpin (**Figure 3.5**). The simulation parameters are equal to the VR sample ones.

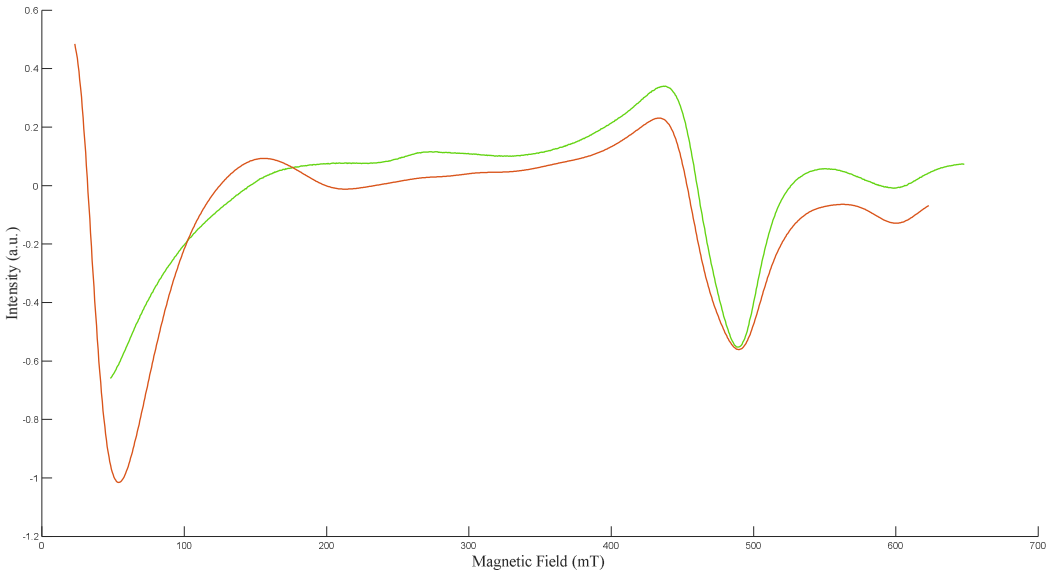

Figure 4.5: SVR sample: simulated spectrum (red line) and experimental spectrum (green line).

Low temperature CW-EPR experiments were performed for the VR sample (see **Figure 4.4**) to study the behavior of the signals.

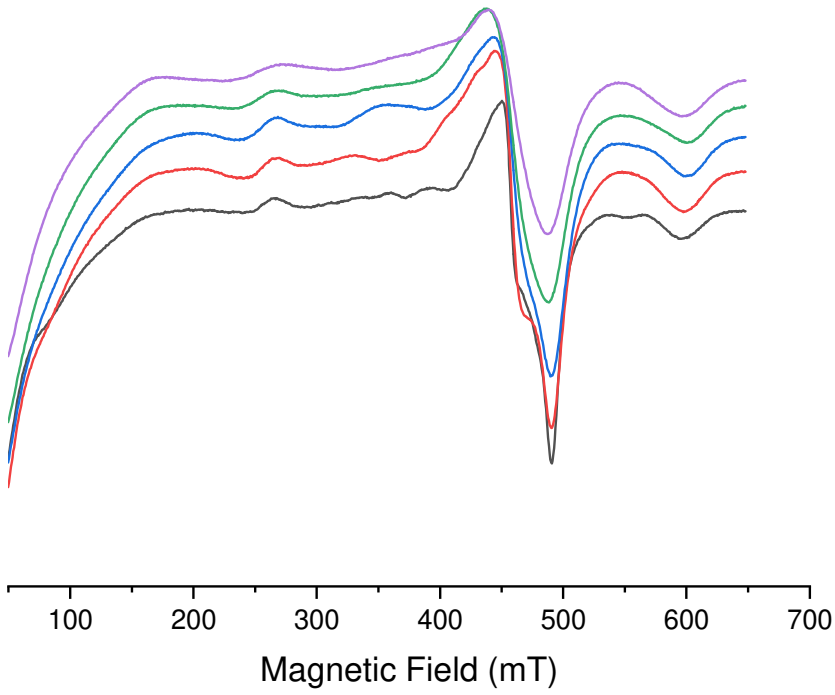

Figure 4.4 Low temperature CW-EPR (X-band) experiments for VR sample: 300K (purple line), 250K (green line), 210K (blue line), 180K (red line) and 150K (black line).

Cooling down the system permits to resolve better the coupling structure of the signals observed at room temperature. In fact, the signal at 450 mT seems to split in a doublet. According to the copper acetate structure, the two unpaired electron of the two Cu(II) nuclei can be coupled to give a singlet (antiferromagnetic coupling, S=0) or a triplet (ferromagnetic coupling, S=1) state. In a crystal structure, many magnetically interacting copper ions are present, and the ferromagnetic/antiferromagnetic behavior is very strong. If the state at lower energy were the antiferromagnetic one, the ferromagnetic state should be the excited one, whereas the opposite would happen if the ferromagnetic state were at lower energy. The EPR signal derives only from the population of the ferromagnetic state (either excited or fundamental), being the antiferromagnetic state EPR-silent. The Double Integral (DI) of an EPR signal is proportional to the amount of species in the ferromagnetic state and, according to Maxwell-Boltzmann statistics, decreasing temperature increases the population of the lower energy state with respect to the excited one. Therefore, plotting the DI values against temperature we should observe an increasing in the signal if the ferromagnetic state is the low-energy state, and a decreasing, if the ferromagnetic state is the high-energy state The two signals (450 mT and 600 mT) were double-integrated to obtain their DI and the DI were plotted against the temperature (**Figure 4.5**) .

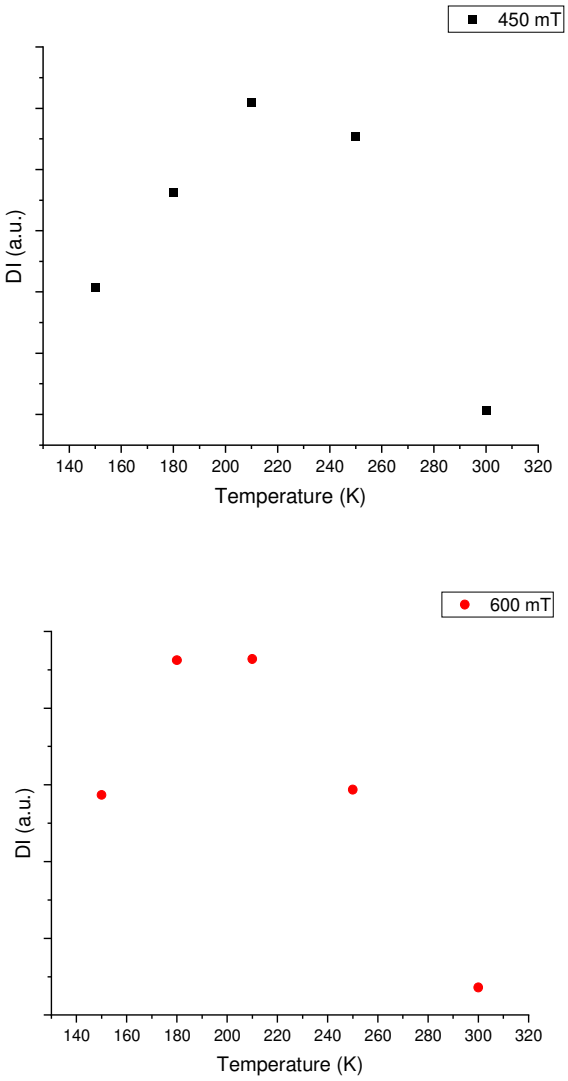

Figure 4.5: DI vs Temperature for 450 mT signals (black dots) and 600 mT (red dots).

Both signals have a peculiar behavior: an initial growth cooling down and then a decrease of DI values below 210 K. This suggests that the stable state is antiferromagnetic at high temperature (above 210 K) and ferromagnetic at low temperature (below 210 K), indicating a ferromagnetic-antiferromagnetic transition around 210 K [27].

The ATR-IR spectrum of the VR sample was acquired and reported in **Figure 4.6**: it has been calculated as the difference between the signal of the sample and the background, as reported in **Chapter 3**. All ATR-IR spectra are reported in this way.

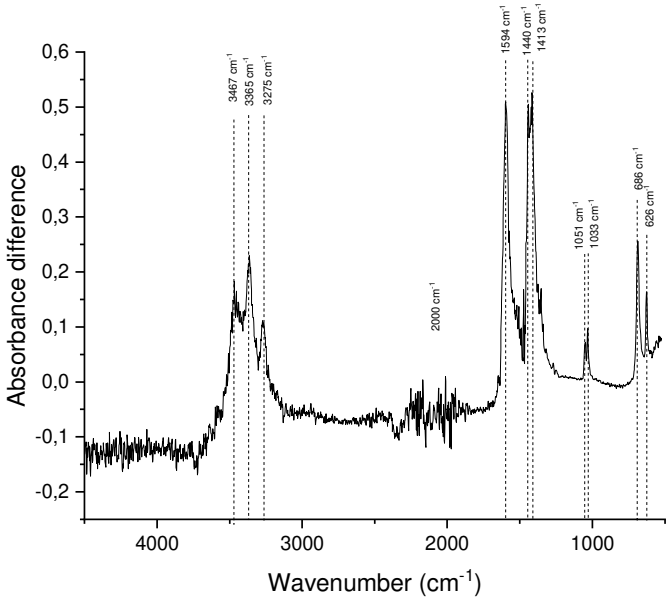

Figure 4.6. ATR-IR spectrum of VR sample.

The ATR-IR spectrum of VR sample shows the typical signals of copper acetate pigment as reported by Platania [28] and Wiggins [29]. The assignments are reported in **Table 4.2**. The acetate -CH stretching are very low in intensity and is impossible to distinguish signal from noise. They should appear around 2980 cm^{-1} in the ATR-IR spectrum.

Wavenumber (cm^{-1})	Chemical function	Type of vibration
3000-3500	-OH	Stretching
1594	-COO	Stretching
1442 and 1413	$-CH_3$	Scissoring
1051 and 1033	$-CH_3$	Rocking
688 and 626	-O-C-O	Stretching

Table 4.2: IR signals of VR sample [28].

The SVR ATR-IR spectrum is very similar (**Figure 3.7**), indicating no structural differences between the two pigments.

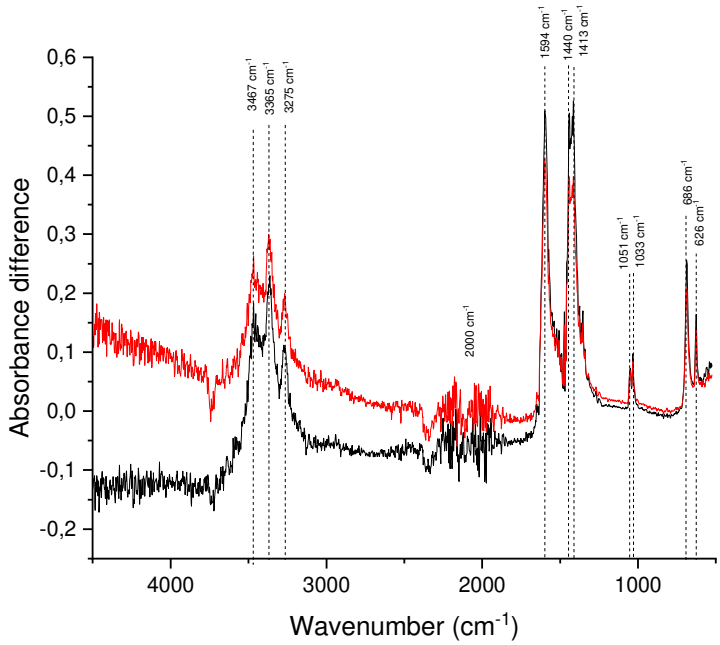

Figure 4.7. ATR-IR spectrum of SVR sample (red line) and VR sample (black line).

4.1.2 Verdigris mixtures

The CW-EPR X-band spectra of pigment/mixtures with a 1:3 ratio were acquired at room temperature and are collected in **Figure 4.8**.

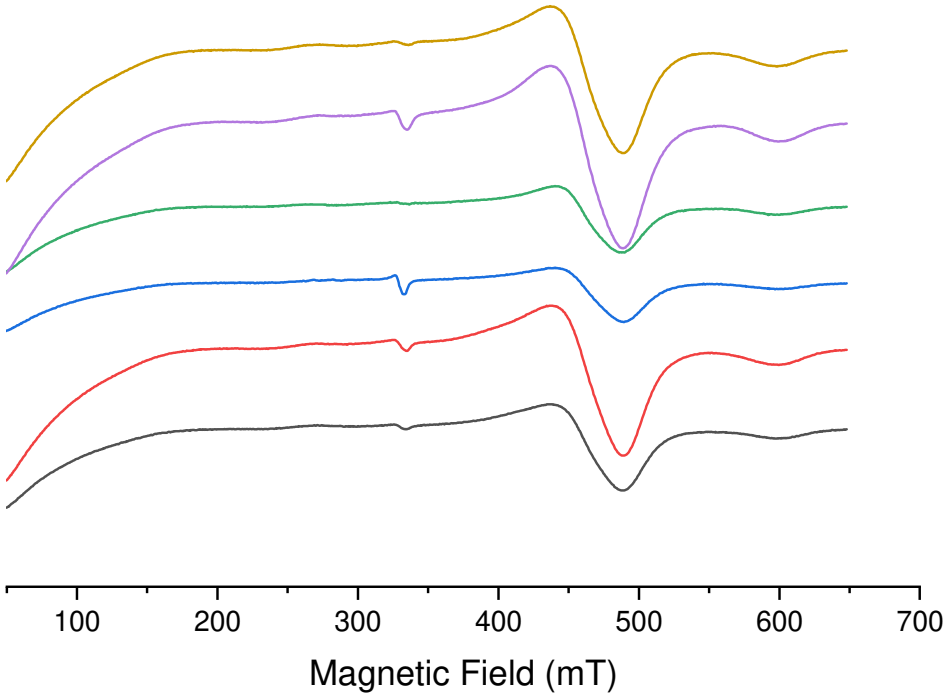

Figure 4.8. CW-EPR (X-band) spectra at room temperature: VRY (yellow line), VREY (purple line), VRO (green line), VRG (blue line), VREW (red line) and VRC (black line).

According to the different binder used in the mixture, the CW-EPR spectrum changes. In particular, the VREY sample, the VRG sample and the VREW sample show a signal around 330 mT. This signal is due to the formation of a monomeric copper species. This is a clear feature that the dimer of copper acetate is partially dissolved in the binder, and the dimeric structure is broken allowing the single copper ions to form complexes with the binder molecules. On the other hand, the VRO sample does not show any signal at 330 mT, indicating that linseed oil molecules does not complex copper ions to form monomeric complexes, at least in these conditions. Compared to the samples VREY, VREW and VRG, the samples VRY and VRC show a weaker

signal of monomeric species, at 330 mT. It appears, therefore, that the more hydrophilic binders (egg white, arabic gum, and whole egg) are more prone to dissolve verdigris producing monomeric copper complexes.

The CW-EPR spectra at room temperatures of the samples with 5% w/w pigment/binder ratio were acquired (**Figure 4.9**). If it is correct the interpretation of the monomeric copper signals as due to Cu(II)-binder complexes, a larger amount of binder should induce the formation of monomeric copper complexes.

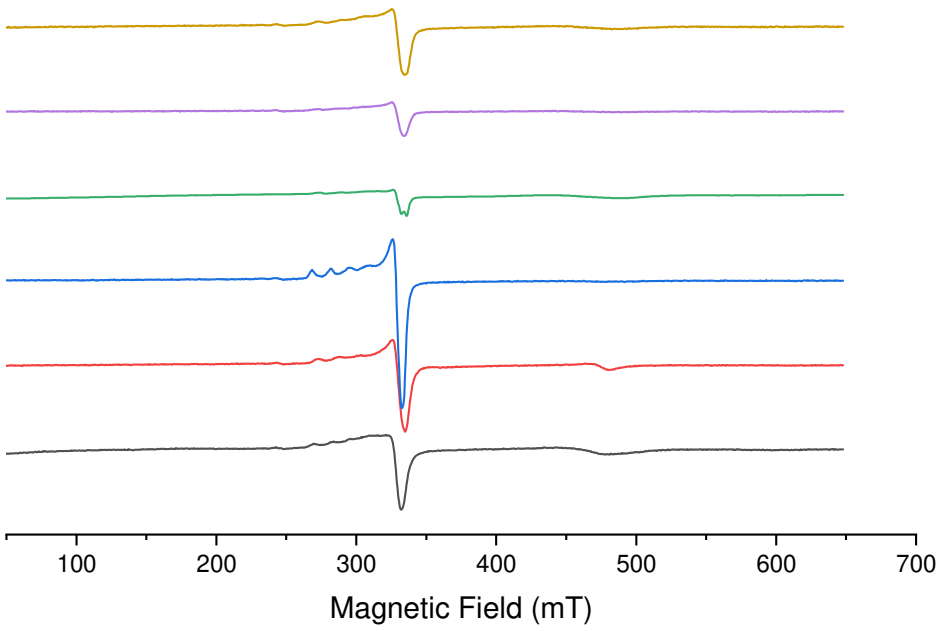

Figure 4.9: CW-EPR (X-band) spectra at room temperature: VRY5 (yellow line), VREY5 (purple line), VRO5 (green line), VRG5 (blue line), VREW5 (red line) and VRC5 (black line).

Actually, the signal at 330 mT is stronger than the signal observed in the 1:3 pigment/ ratio samples. In some cases (VRY5, VREY5, VRG5), the dimer copper signal is disappeared, indicating that verdigris crystals were completely dissolved in the binder. In other cases (VRO5 and VRC5), the dimer signal is still present. The stronger dimer signal belongs to the VRO5 sample: the linseed oil molecules appear to be weaker ligands for the copper center.

In **Figure 4.10,** the CW-EPR spectra of the monomeric species for the 5% samples are shown in more detail: the signal is strong and almost noiseless, and the line quartet at low field can be appreciated very well.

Therefore, for each sample it was possible to get a simulation and determine g-factor and hyperfine constant A values. In most cases, two monomeric specie were needed to properly simulate the signal. The VRC5 spectrum displays also some minor features, maybe due to the coupling between the copper center and coordinating nitrogen atoms, inducing an hyperfine sub-pattern. The signal at 242 mT, indicated in figure, belongs to the cavity background.

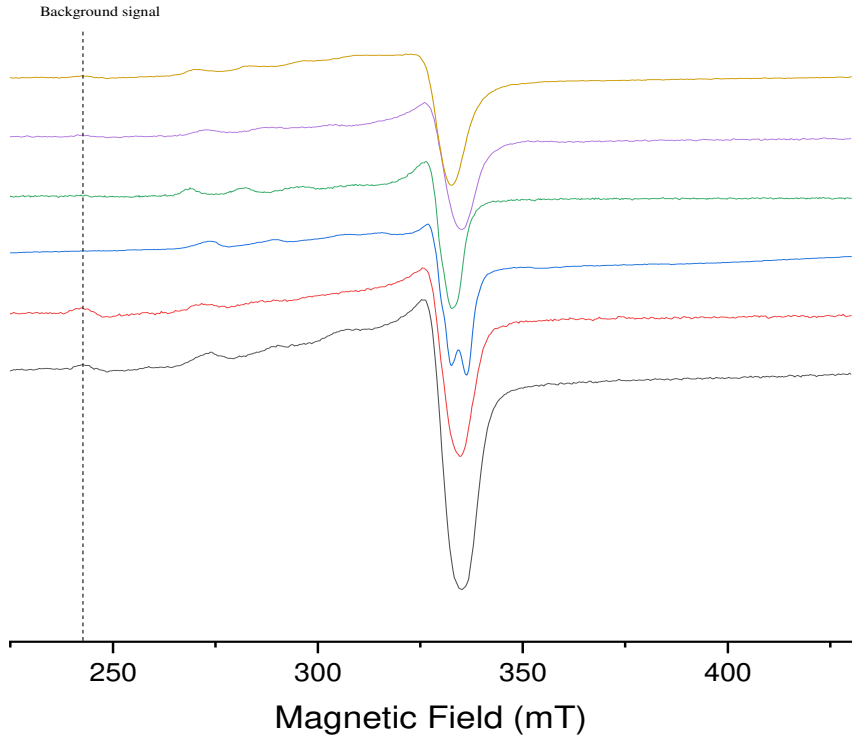

Figure 4.10: CW-EPR (X-band) spectra at room temperature: VRY5 (yellow line), VREY5 (purple line), VRO5 (green line), VRG5 (blue line), VREW5 (red line) and VRC5 (black line).

From **Figure 4.11** to **Figure 4.16** the spectra and the corresponding simulations, for each sample, are reported.

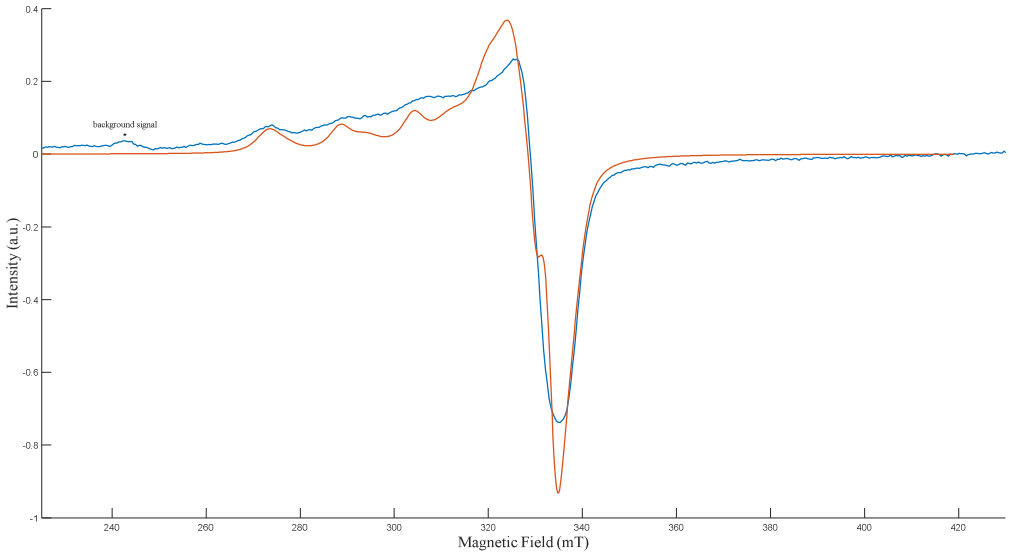

Figure 4.11. VRY5 sample: simulated spectrum (red line) and experimental spectrum (blue line).

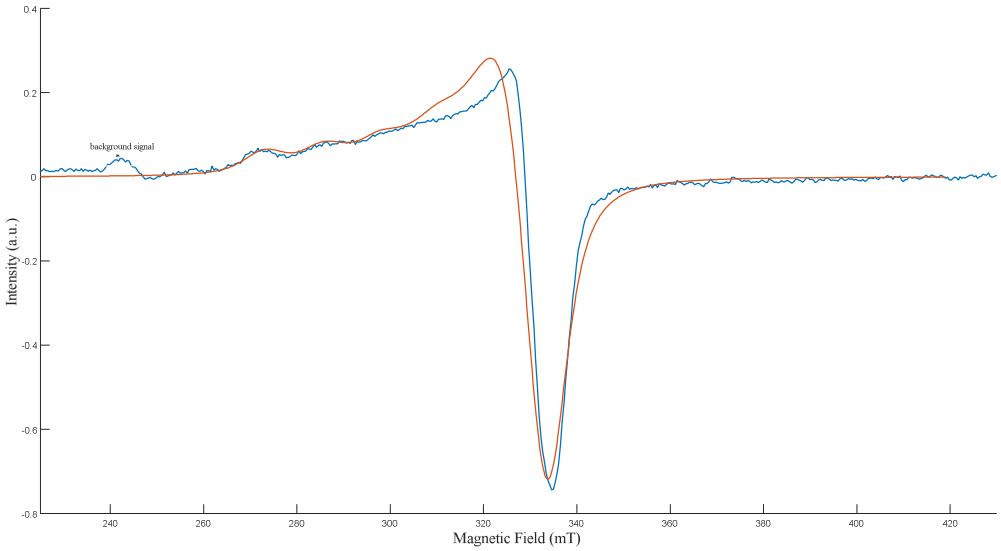

Figure 4.12. VREY5 sample: simulated spectrum (red line) and experimental spectrum (blue line).

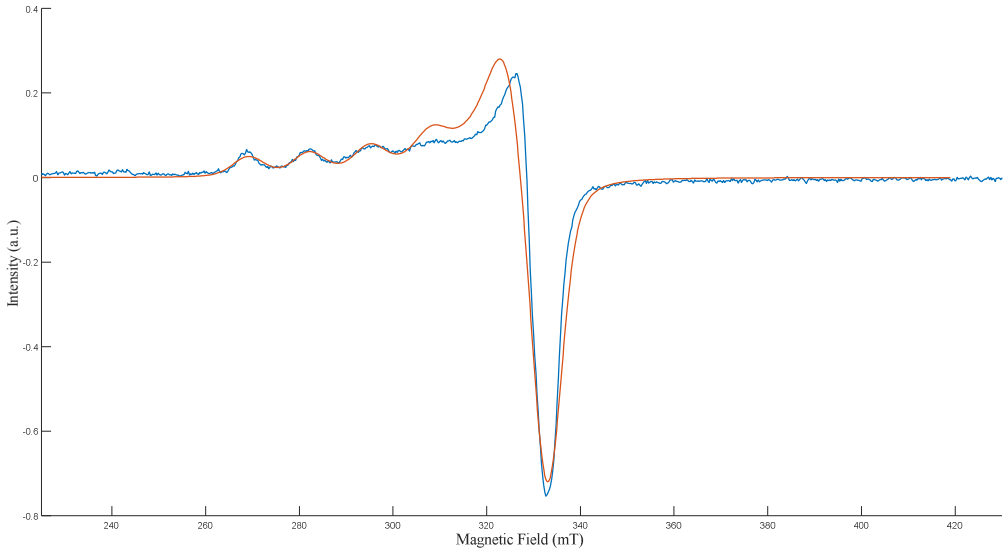

Figure 4.13. VRG5 sample: simulated spectrum (red line) and experimental spectrum (blue line).

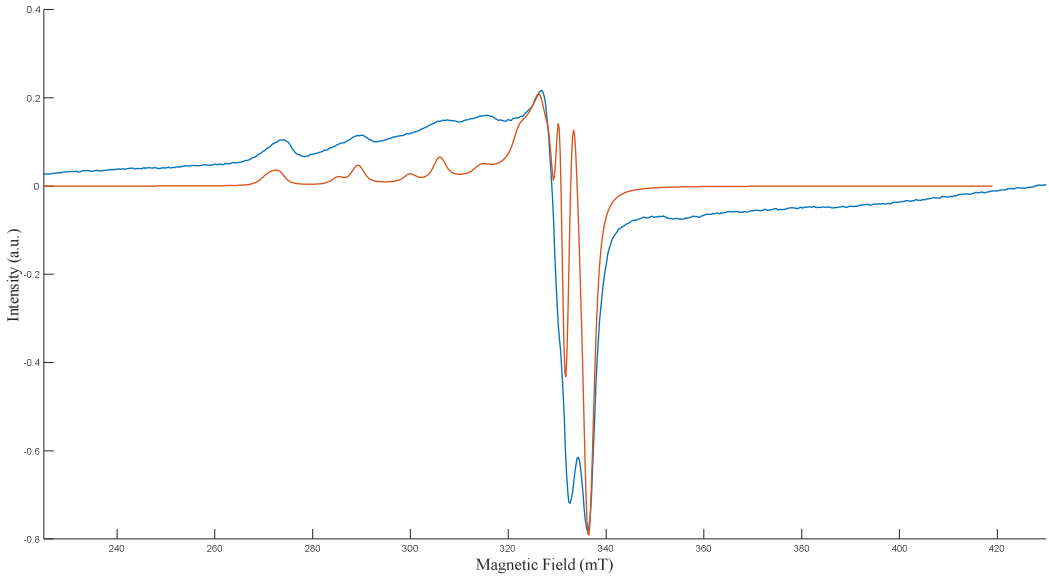

Figure 4.14. VRO5 sample: simulated spectrum (red line) and experimental spectrum (blue line).

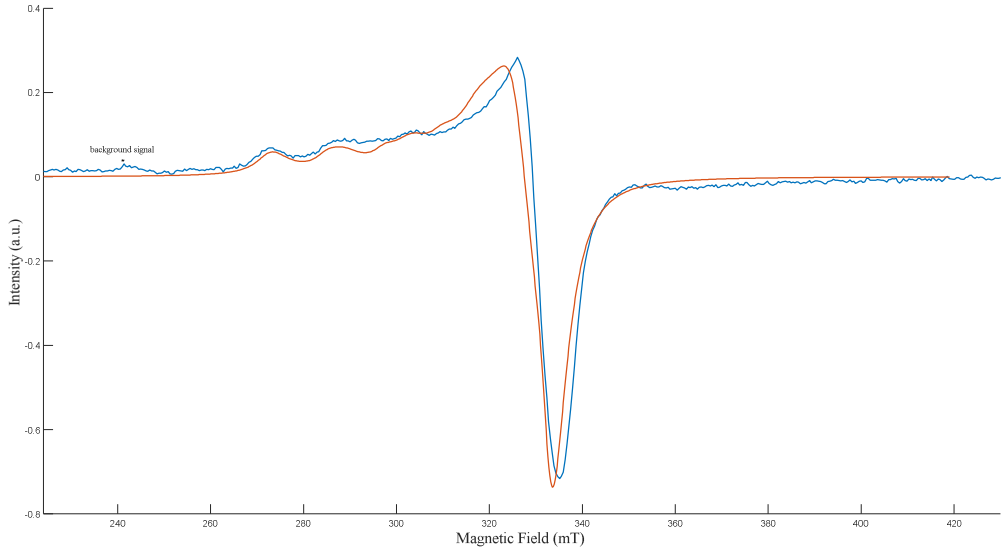

Figure 4.15. VREW5 sample: simulated spectrum (red line) and experimental spectrum (blue line).

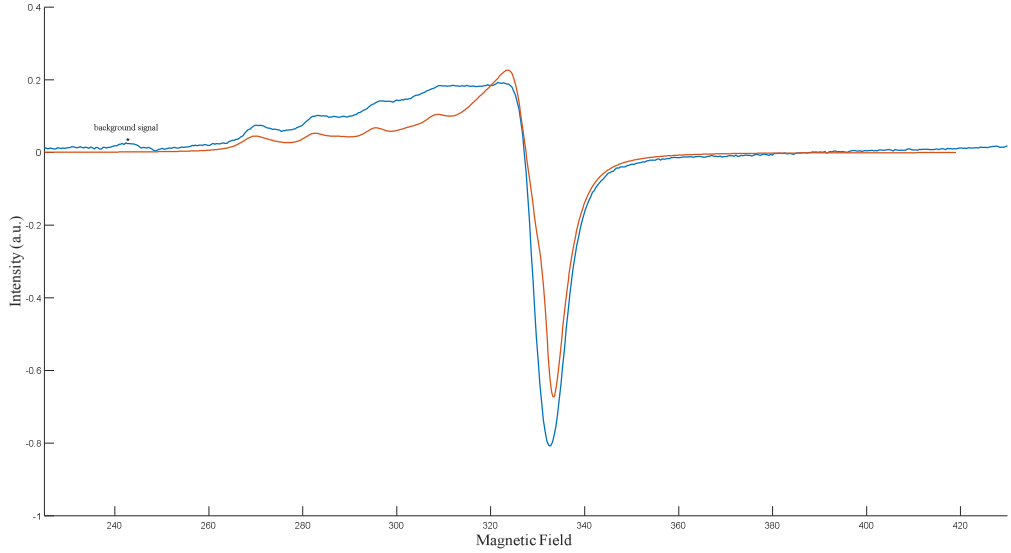

Figure 4.16. VRC5 sample: simulated spectrum (red line) and experimental spectrum (blue line).

All simulation parameters are collected in **Table 4.3**.

Sample	VRO5		VRG5	VRC5		VREW5		VRY5		VREY5	
Species	1	2	1	1	2	1	2	1	2	1	2
g_x	2.06	2.06	2.07	2.07	2.07	2.07	2.07	2.07	2.07	2.07	2.07
g_y	2.06	2.06	2.07	2.07	2.07	2.07	2.07	2.07	2.07	2.07	2.07
g_z	2.29	2.33	2.36	2.36	2.31	2.34	2.31	2.25	2.30	2.34	2.30
A_x (MHz)	58	58	50	50	58	50	58	50	58	50	58
A_y (MHz)	34	34	50	50	34	50	34	50	34	50	34
A_z (MHz)	524	470	420	420	480	400	460	550	490	400	460
$gStrain_{x,y}$	0.005	0.005	0.005	0.01	0.005	0.005	0.005	0.005	0.005	0.005	0.005
$gStrain_z$	0.01	0.01	0.01	0.01	0.01	0.01	0.01	0.01	0.01	0.01	0.01
$Astrain_{x,y}$ (MHz)	0.5	0.5	0.5	0.5	0.5	0.5	0.5	0.5	0.5	0.5	0.5
$Astrain_z$ (MHz)	1.0	1.0	1.0	1.0	1.0	1.0	1.0	1.0	1.0	1.0	1.0
Weight	71%	29%	100%	50%	50%	25%	75%	25%	75%	66%	34%

Table 4.3: Simulation parameters for all samples: VRO5, VRG5, VRC5, VREW5, VRY5 and VREY5 at room temperature. The row "weight" indicates the percentage of that species in the simulated spectrum.

Some species, with different binders, have similar simulation parameters, suggesting the formation of similar complexes for the copper center. E.g., VRG5 and the species 1 of VRC5 have the same g and A values. In addition, in the samples VREW5 and VREY5 the simulated species are identical, indicating the formation of the same kind of complexes, although with a different ratio among the species. This suggest that the protein components of the egg white are the binding ones, but the different environment affects the relative amount.

The EPR spectra of the SVRC5 and SVRO5 samples (synthetic pigment) were acquired at room temperature and simulated to confirm features observed in the other samples (**Figure 3.17** and **Figure 3.18**). They represent a fatty mixture (SVRO5) and

a protein mixture (SVRC5) as two limit cases. The simulation parameters are equal to the VRC5 and VRO5 samples, but the weight percentage changes a bit for the SVRC5 sample: the first species is more present (75%) than the second one (25%).

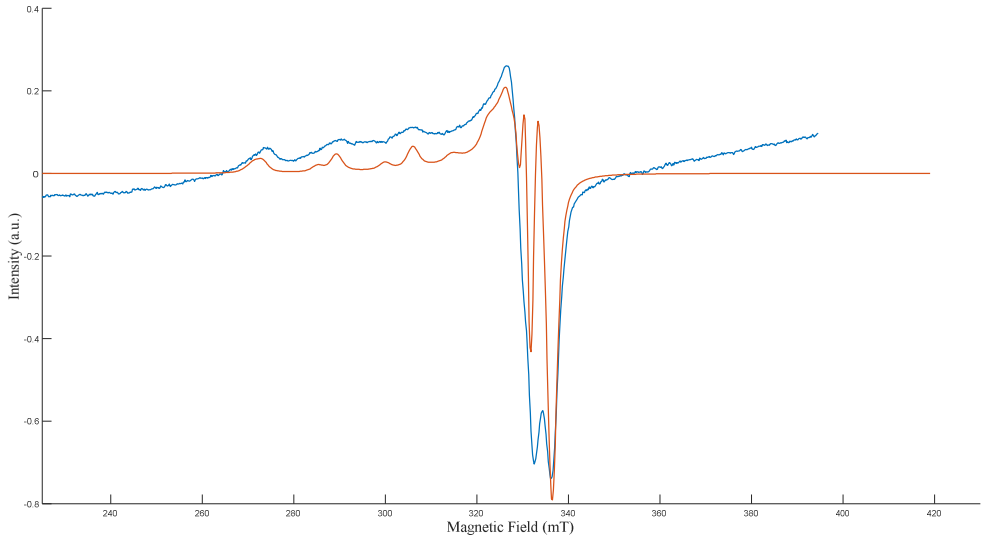

Figure 4.17: SVRO5 sample: simulated spectrum (red line) and experimental spectrum (blue line).

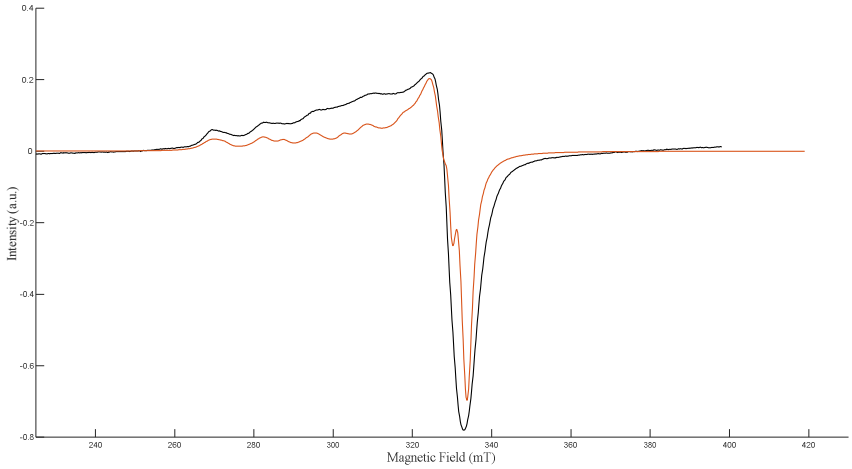

Figure 4.18: SVRC5 sample: simulated spectrum (red line) and experimental spectrum (black line).

According to what reported by Peisach e Blumberg, it is possible to establish which kind of copper complexes are formed with the binder by plotting $A_{//}(A_z)$ against $g_{//}(g_z)$. It can be established the nature of the donating atom and the number of them in the

complex. **Figure 4.18** displays the Peisach-Blumberg assignation diagram with the experimental data plotted for all simulated complexes. The $A_{//}$ (A_z) values, previously obtained in MHz by simulation, are converted in mK according to the following equation (**Eq. 4.1**):

$$A_{//} = 0.04686 g_{//} \Delta H \qquad \textbf{Eq. 4.1}$$

where ΔH is the separation between two lines of the quartet in the copper signal expressed in Gauss [24]. The $A_{//}$ (A_z) are reported in this way in all the Peisach-Blumberg diagrams.

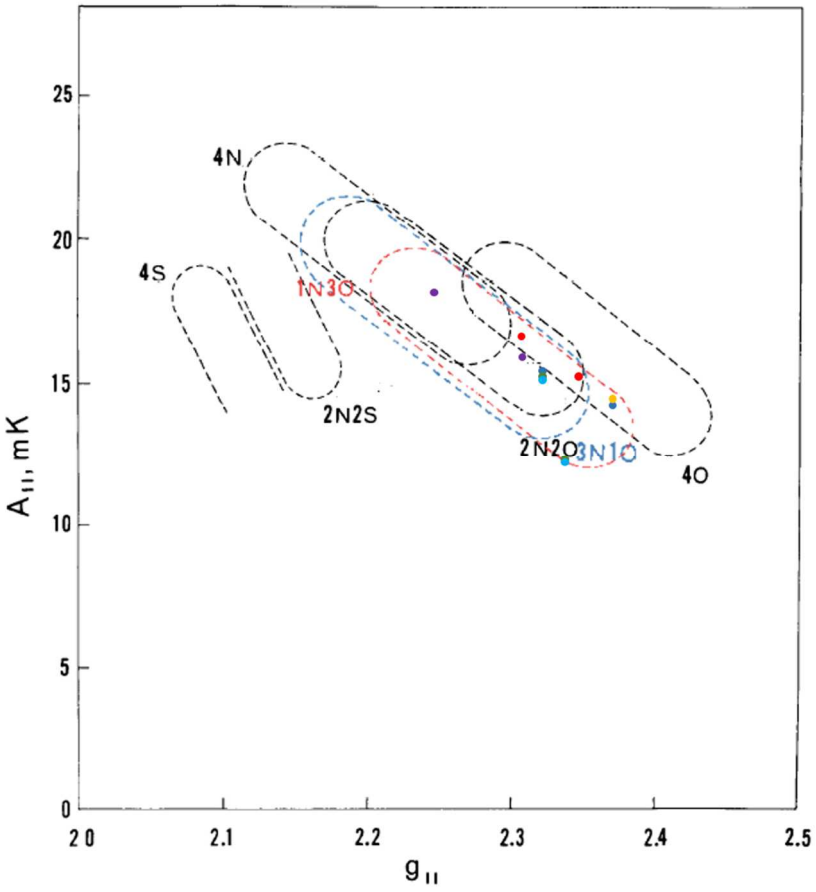

Figure 4.18: Peisach-Blumberg diagram: VRO5 (red dots), VRC5 (blue dots), VRG5 (yellow dots), VREW (green dots), VRY5 (purple dots) and VREY5 (light blue dots).

The VRO5 (red dots) complexes are included in the 4O curve suggesting the formation of two copper complexes with four bonded oxygens, as expected for a fatty acid

matrix, which contains only oxygen atoms as possible donors. The VRG5 complex (yellow dot) has the same assignation, in agreement with the polysaccharides structure. The VRC5 complexes (blue dots) are included in two different regions: one in the 4O region and one in the "nitrogen" region (at least, one coordinating nitrogen). These kinds of signal are expected for a protein binder, showing a complexation that involves nitrogen. The occurrence of Cu-N coupling is in agreement with the small features seen previously in the experimental spectrum of VRC5. The number of nitrogen atoms involved in the complexes is not easy to assess because of the superposition of the assignment regions. The VREW5 sample shows two complexes in the nitrogen region with a variable number of nitrogen atoms. The VREY5 sample has the same kind of complexes. Therefore, the observed copper complexes in VREW5 and VREY5 are likely due to the protein components of egg. Interestingly, the VRY5 complexes are deeply located in the nitrogen region, suggesting a high number of coordinating nitrogen atoms for these complexes (4N or 3N1O).

From the previous data, it can be deduced that the higher the amount of protein, the more nitrogen atoms are involved in the copper complexation. Moreover, the $g_{//}$ and the $A_{//}$ values are influenced also by the global charge of the complex. Therefore, properties of the mixtures such as pH influence the position in the Peisach-Blumberg plot.

Other CW-EPR spectra for the 5% samples were acquired at different temperatures (250 K, 210 K, 180 K and 150 K) to resolve better the hyperfine pattern and to verify if simulation parameters change with temperature (see from **Figure 4.16** to **Figure 4.21**).

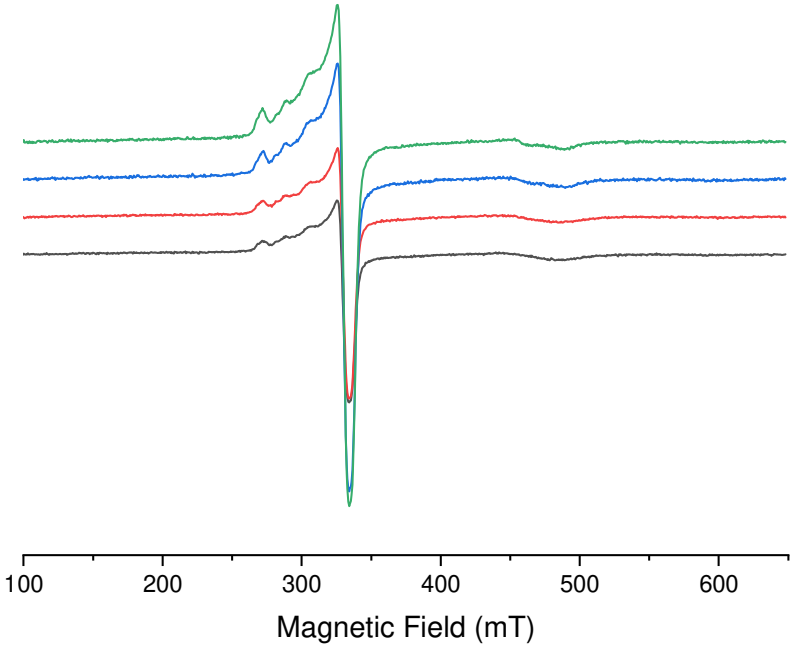

Figure 4.16. VRY5 sample: 150K (green line), 180K (blue line), 210K (red line) and 250K (black line).

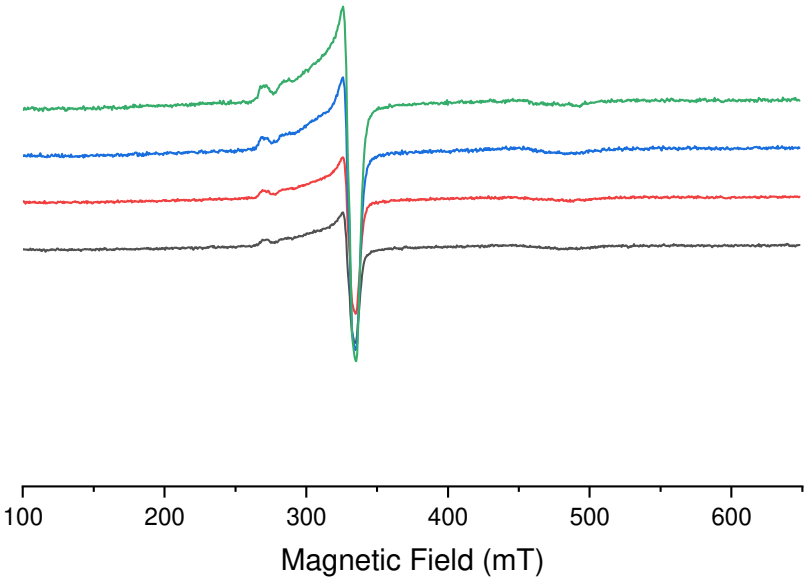

Figure 4.17. VREY5 sample: 150K (green line), 180K (blue line), 210K (red line) and 250K (black line).

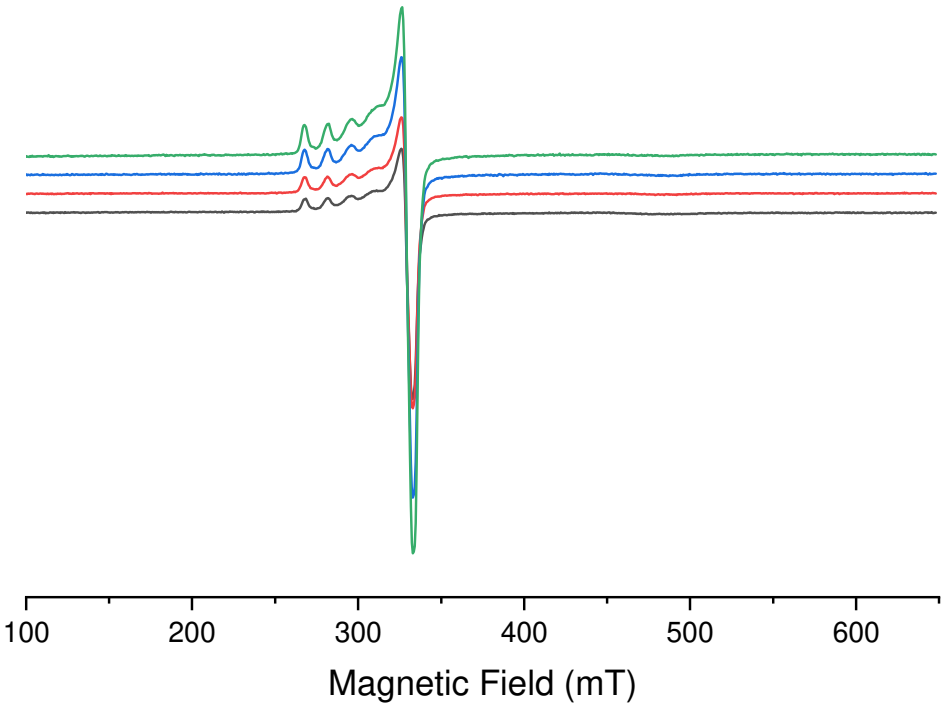

Figure 4.18. VRG5 sample: 150K (green line), 180K (blue line), 210K (red line) and 250K (black line).

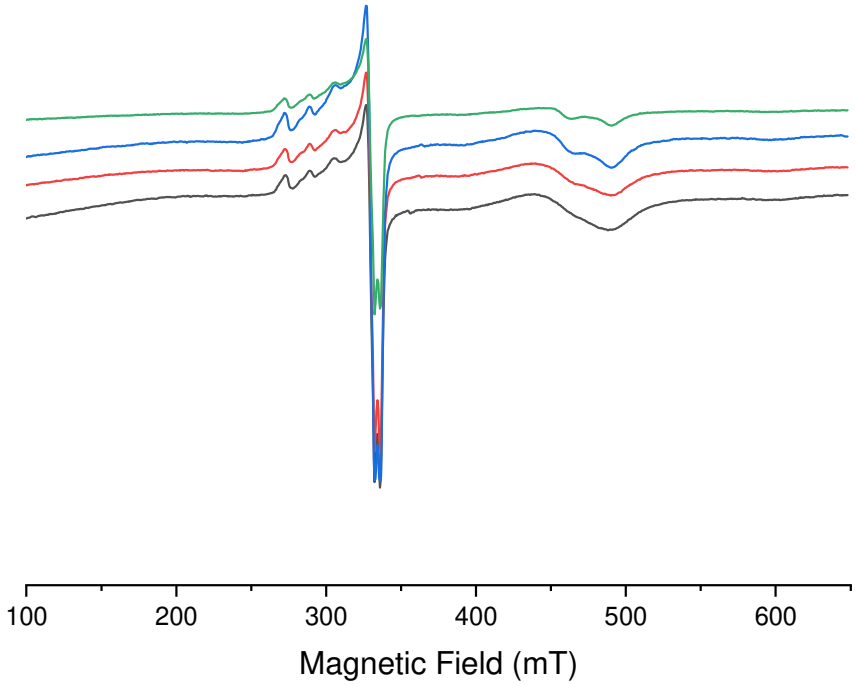

Figure 4.19. VRO5 sample: 150K (green line), 180K (blue line), 210K (red line) and 250K (black line).

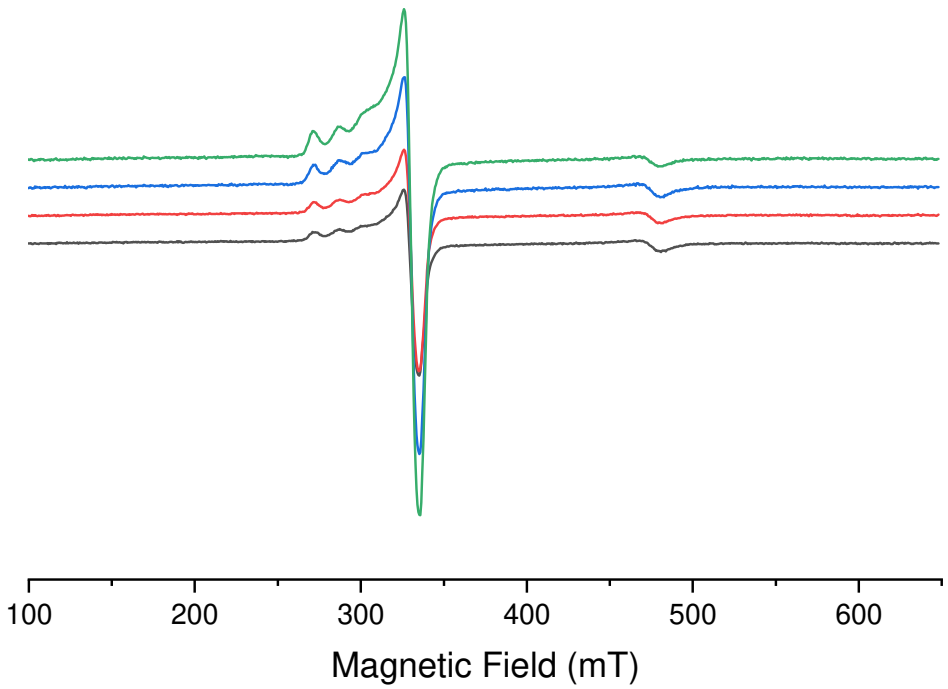

Figure 4.20. VREW5 sample: 150K (green line), 180K (blue line), 210K (red line) and 250K (black line).

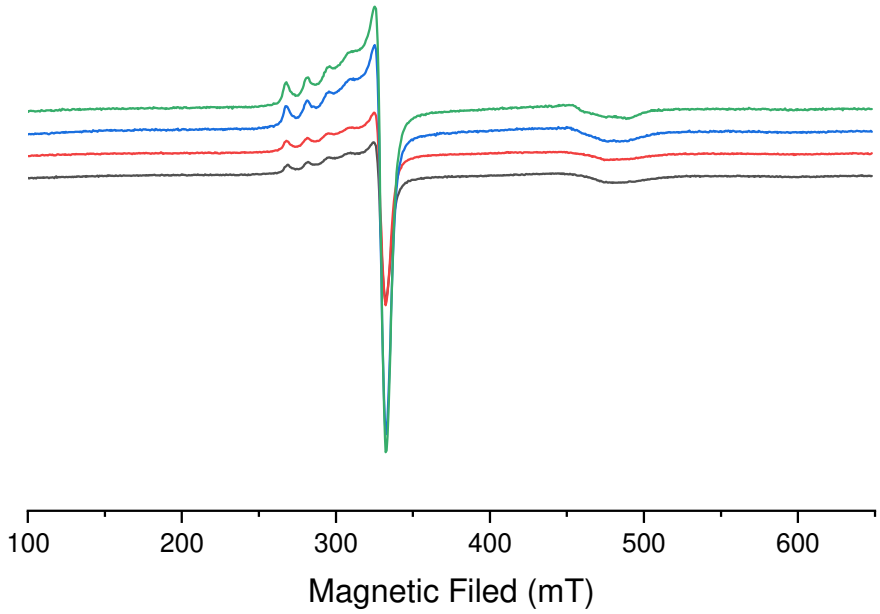

Figure 4.21. VRC5 sample: 150K (green line), 180K (blue line), 210K (red line) and 250K (black line).

The dimer signal at 450 mT, when observed, has a shape depending on temperature: linewidth decreases on lowering temperature, showing what could be a hyperfine

structure around 150 K. The DI of dimer signal was calculated for all the samples that still show the dimer and plotted against temperature (see **Figure 4.22**). Interestingly, for most of the samples, DI does not change, or changes very little with temperature, a behavior expected for a paramagnetic species.

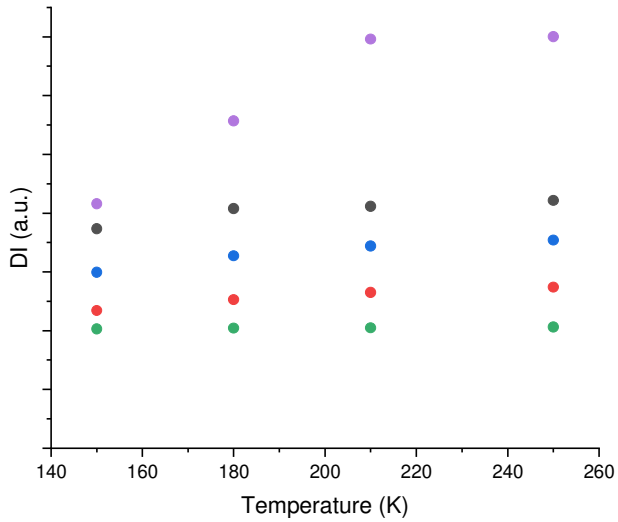

Figure 4.22: DI of dimer signal (450 mT) vs temperature: VRC5 (black dots), VREW5 (red dots), VRY5 (blue dots), VREY5 (green dots) and VRO5 (purple dots).

This indicates that the dimeric signal is mainly related to isolated dimeric species, and not to dimeric species magnetically interacting in a crystal, as observed for the VR sample. On the other side, the VRO5 sample shows a maximum at 210K, and decreases below 210 K, as seen for VR sample. The maximum indicates a residual ferromagnetic behavior, suggesting the presence of small pigment crystals. Therefore, for all the 5% samples, but VRO5, verdigris pigment is completely dissolved in the binder, but a certain amount of dimer is broken, and the copper centers form monomeric complexes, while some amount of dimer is dissolved as itself.

The DI for the monomer signal was calculated, and plotted against the temperature (see **Figure 4.23**)

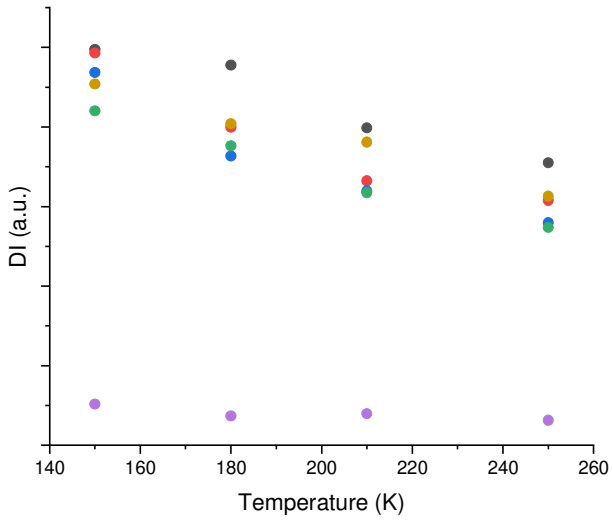

Figure 4.23: DI of monomer signal (330 mT) vs temperature: VRG5 (black dots), VRC5 (red dots), VREW5 (blue dots), VRY5 (green dots), VREY5 (purple dots) and VRO5 (brown dots).

On lowering temperature, the monomer signal DI slightly increases for all the samples: this is an indication that the monomeric species is paramagnetic, and follows the Curie law.

There is another trend to underline: in some cases, the lines of the quartet become broader on lowering temperature. This is the indication that at higher temperatures, the binder is still fluid and the slightly different copper complexes rearrange quickly, dynamically averaging their $g_{//}$ and $A_{//}$ values. At lower temperature, the slow motion causes line broadening. At very low temperature (150 K), the monomer signal could be resolved in an overlap of different signals, corresponding to different copper species.

Therefore, the spectra acquired at 150 K were simulated to verify if there are some differences between complexes at room temperature and 150 K. The simulated spectra are shown from **Figure 4.24** to **Figure 4.29** and the simulation parameters are collected in **Table 4.4**.

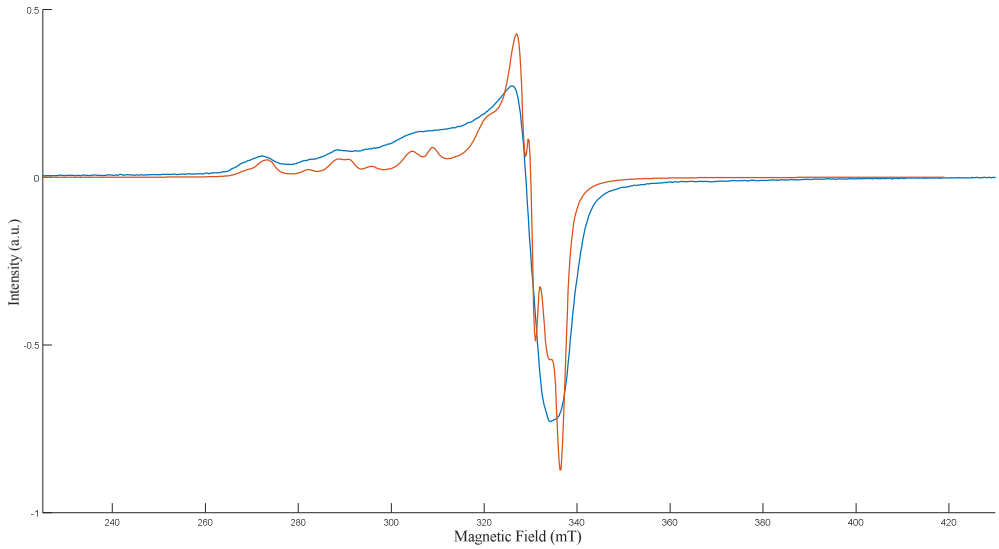

Figure 4.24. VRY5 150K sample: simulated spectrum (red line) and experimental spectrum (blue line).

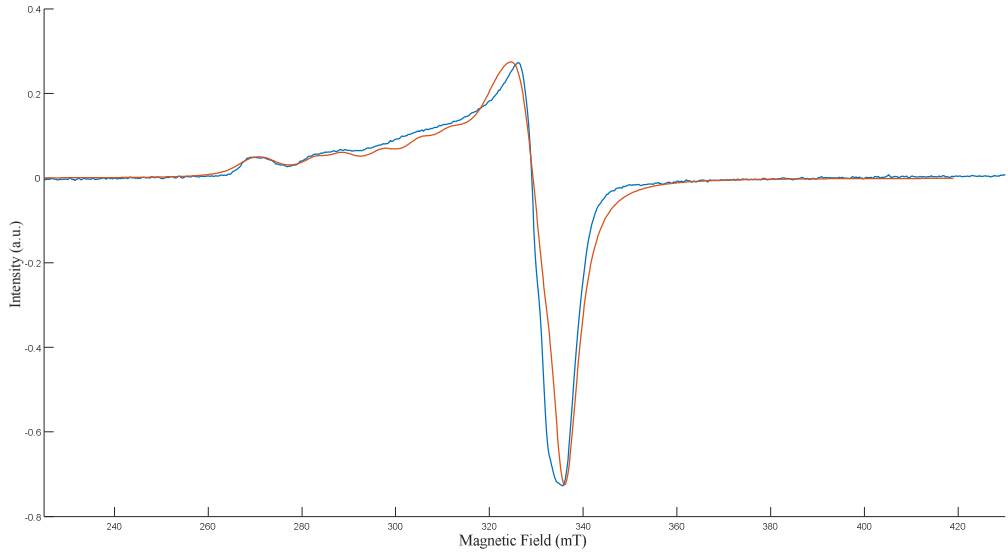

Figure 4.25. VREY5 150K sample: simulated spectrum (red line) and experimental spectrum (blue line).

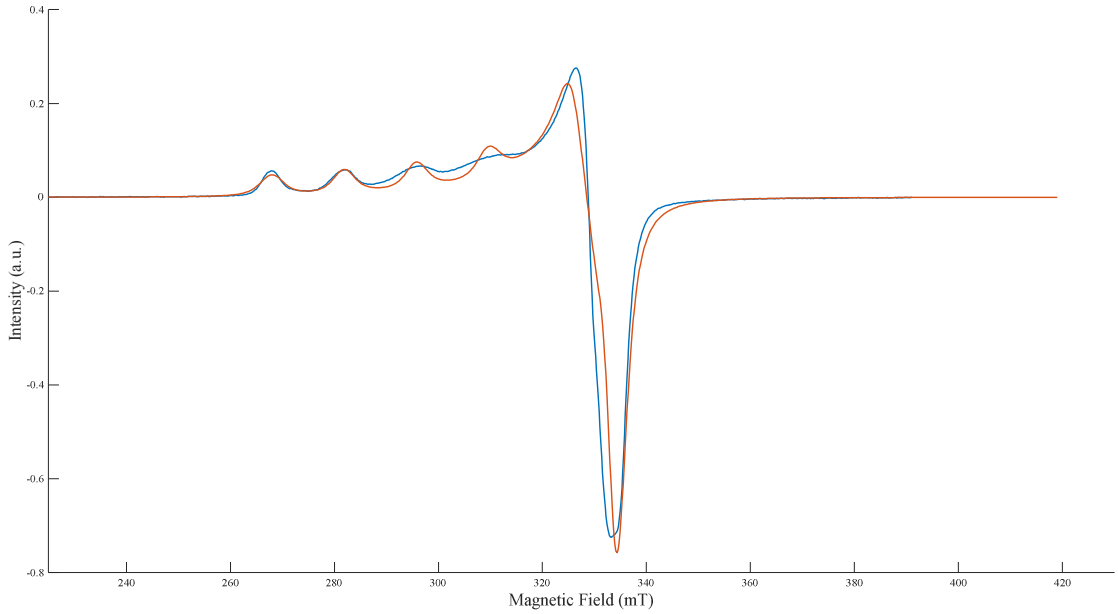

Figure 4.26. VRG5 150K sample: simulated spectrum (red line) and experimental spectrum (blue line).

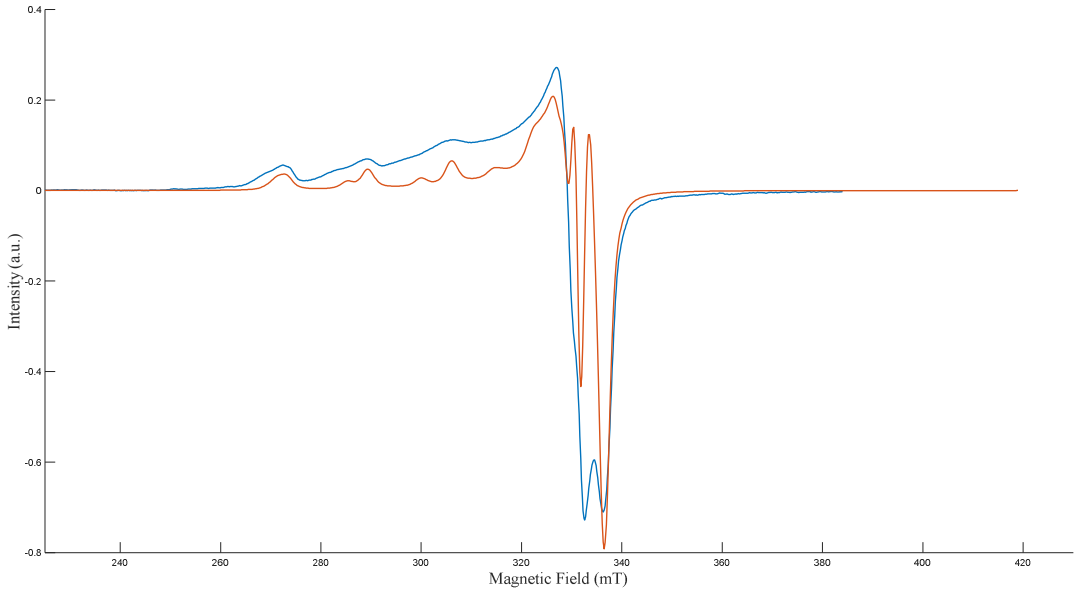

Figure 4.27. VRO5 150K sample: simulated spectrum (red line) and experimental spectrum (blue line).

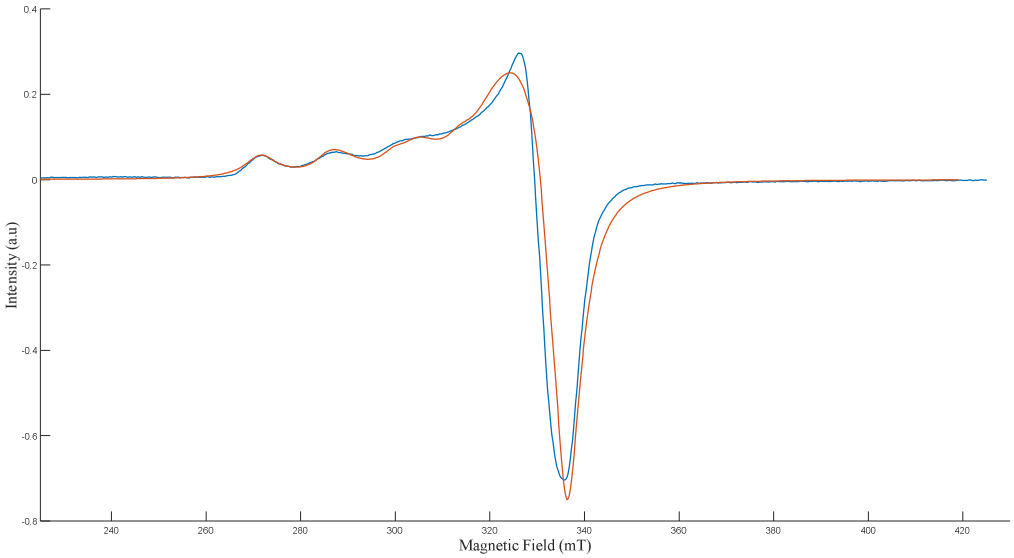

Figure 4.28. VREW5 150K sample: simulated spectrum (red line) and experimental spectrum (blue line).

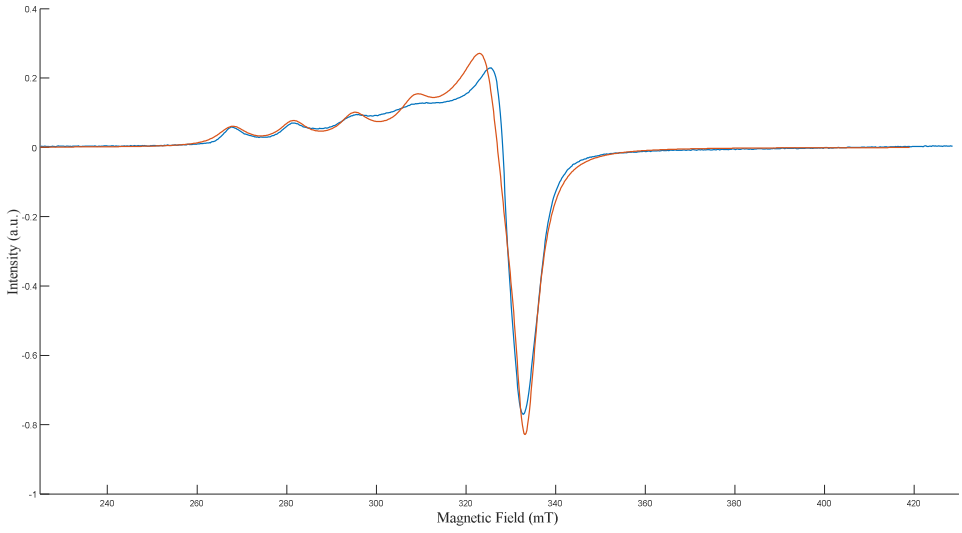

Figure 4.29. VRC5 150K sample: simulated spectrum (red line) and experimental spectrum (blue line).

Sample	**VRO5**		**VRG5**	**VRC5**	**VREW5**		**VRY5**			**VREY5**	
Species	1	2	1	1	1	2	1	2	3	1	2
g_x	2.06	2.06	2.06	2.07	2.05	2.06	2.07	2.07	2.07	2.07	2.07
g_y	2.06	2.06	2.07	2.07	2.05	2.06	2.07	2.07	2.07	2.07	2.07
g_z	2.29	2.33	2.36	2.37	2.33	2.30	2.25	2.30	2.36	2.35	2.30
A_x (MHz)	58	58	50	50	50	58	50	58	50	50	58
A_y (MHz)	34	34	50	50	50	34	50	34	50	50	34
A_z (MHz)	524	470	450	440	450	520	550	490	440	460	520
$gStrain_{x,y}$	0.005	0.005	0.005	0.01	0.005	0.005	0.005	0.005	0.005	0.005	0.005
$gStrain_z$	0.01	0.01	0.01	0.01	0.01	0.01	0.01	0.01	0.01	0.01	0.01
$Astrain_{x,y}$ (MHz)	0.5	0.5	0.5	0.5	0.5	0.5	0.5	0.5	0.5	0.5	0.5
$Astrain_z$ (MHz)	1.0	1.0	1.0	1.0	1.0	1.0	1.0	1.0	1.0	1.0	1.0
Weight	71%	29%	100%	100%	25%	75%	16%	68%	16%	50%	50%

Table 4.4. Simulation parameters for all samples: VRO5, VRG5, VRC5, VREW5, VRY5 and VREY5 at 150K of temperature. The row "weight" indicates the percentage of a species in the simulated spectrum.

The simulation parameters for the mixtures at 150 K and at room temperature do not have big differences. In some cases, the A_z constant becomes larger at low temperature: this is probably due to the stabilization of slightly different complexes. Therefore, there are many species not simulated but included and averaged with the species used to reproduce experimental spectrum. In fact, one the most challenging problem in the simulation of spectra is to reproduce the line broadening. Therefore, further improvements of the program used to simulate the spectra are needed.

The ATR-IR spectra for the pure binders (**Figure 4.30**) and the samples (**Figure 4.31**) have been also acquired.

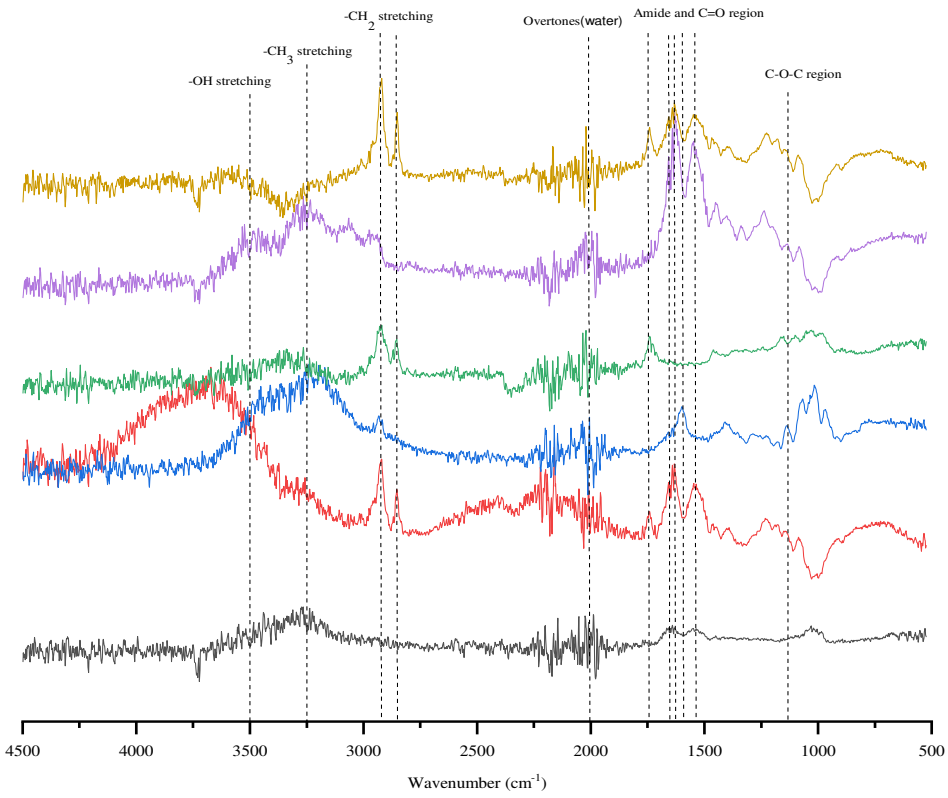

Figure 4.30. ATR-IR spectra of: egg white (black line), egg white and yolk (red line), arabic gum (blue line), rabbit glue (purple line) and yolk (yellow line).

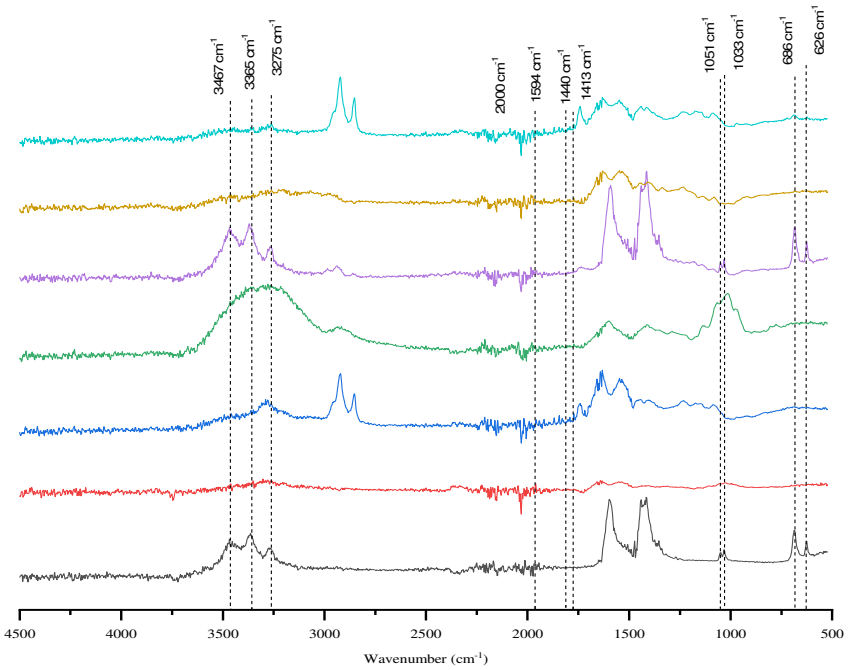

Figure 4.31: ATR-IR spectra of: VR (black line), VREW5 (red line), VREY5 (blue line), VRG5 (green line), VRO5 (purple line), VRC5 (yellow line) and VRY5 (turquoise line).

The ATR-IR spectra of the samples confirm some indications obtained from the EPR data: the VRO5 spectrum still shows the typical verdigris signals (**Table 4.2**), while in the other samples these features are not present. This confirm that linseed oil molecules are not a strong ligand for the copper center, and that verdigris is dispersed, and not dissolved, in this binder. On the other hand, the other samples do not show bands related to verdigris. The spectra clearly show the signals of the binders. This indicates that the pigment is actually dissolved in the binder matrix. Small changes in the IR spectra are observed in the region around 1600 cm^{-1}, where carboxylate signals are expected. This indicates a different chemical environment for the binder molecules and therefore suggests the formation of binder-copper complexes.

The ATR-IR spectra for the SVRO5 and the SVRC5 sample were acquired. The signals of SVRO5 and SVRC5 signals are equal to the VRO5 and VRC5 signals respectively (see **Figure 4.32**).

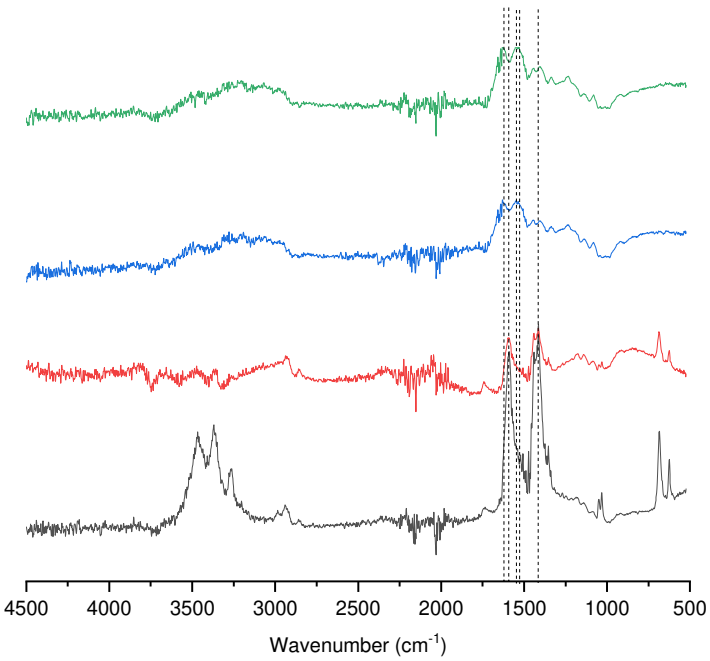

Figure 4.32: ART-IR spectra: VRO5 (black line), SVRO5 (red line), SVRC5 (blue line) and VRC5 (green line).

4.2 Copper resinate

4.2.1 Raw pigment (RR sample)

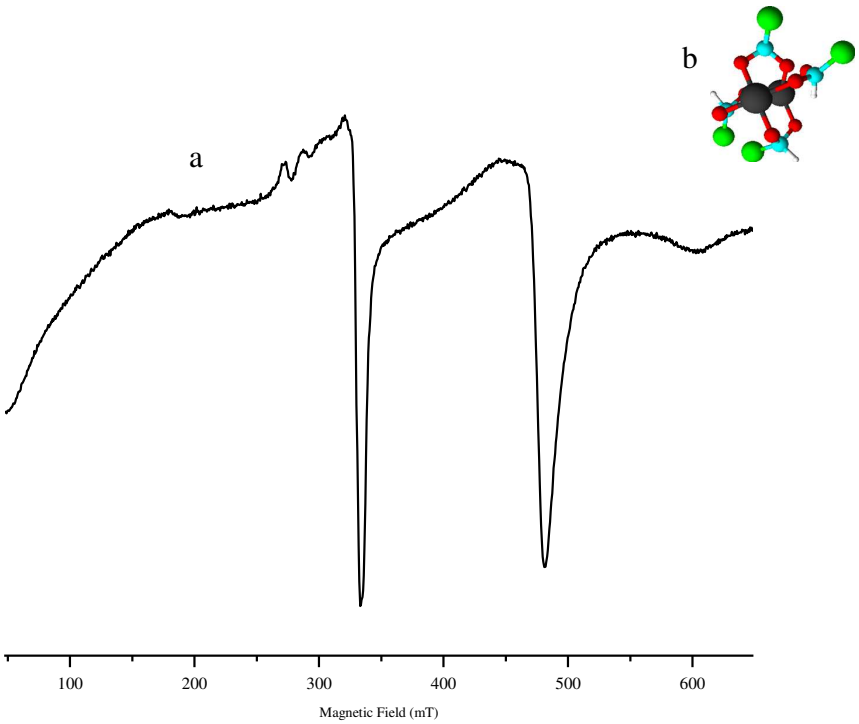

Figure 4.33: a) EPR spectrum of RR b) Copper resinate 3D structure (see **Chapter 2**).

Figure 4.33a displays the spectrum of pure copper resinate (RR). There are four main signals: one in the range 100-140 mT, one at 470 mT, one at 600 mT, and finally one at 330 mT. The first three signals suggest a copper dimer, as seen for the VR sample, while the last one suggests the presence of a copper monomer. The copper resinate, as discussed in the **Chapter 2**, is prepared by mixing verdigris pigment with some natural resin, generating a dimer structure (see **Figure 3.32 b**). Therefore, the signal at 330 mT suggests that the natural resin can complex the copper atoms and form monomer species. An XRF spectrum was acquired for the RR sample (**Figure 4.34**) to exclude the presence of other EPR-active metals.

The XRF spectrum clearly shows only copper signals, ruling out other possible EPR-detectable species.

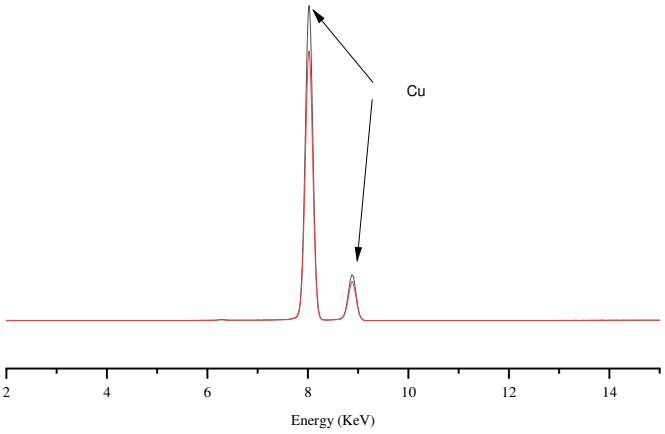

Figure 4.34: XRF spectrum of RR sample.

The CW-EPR spectrum of RR sample was simulated to obtain g and A values for the dimer and the monomer signals. The two simulations were performed separately to avoid software artifacts (see **Figure 4.35** and **Figure 3.36**).

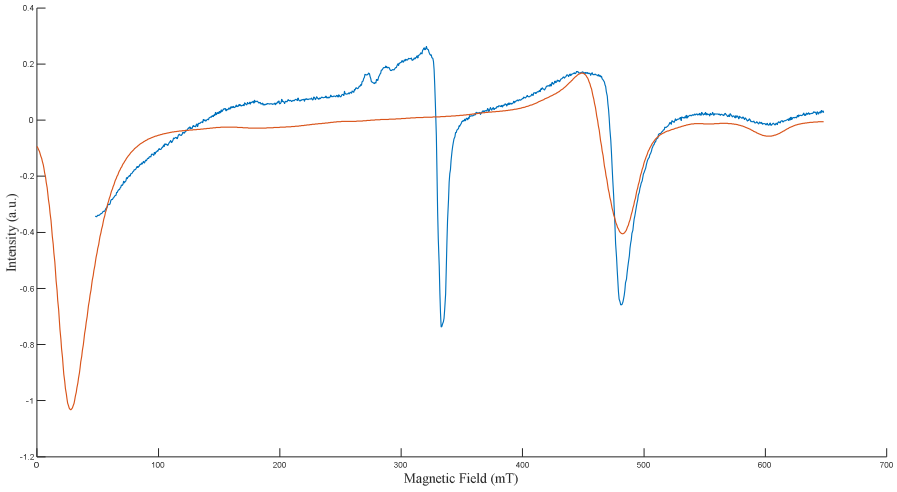

Figure 4.36: RR dimer: simulated spectrum (red line) and experimetnal spectrum (blue line).

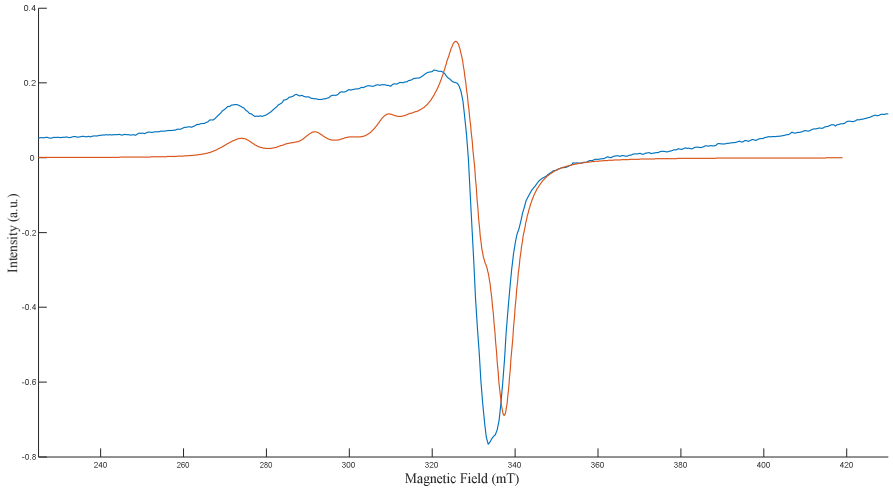

Figure 4.36: RR monomer: simulated spectrum (red line) and experimental spectrum (blue line).

Sample	g_x	g_y	g_z	A_x (MHz)	A_y (MHz)	A_z (MHz)	D (MHz)	E (MHz)
RR	2.05	2.05	2.30	15	15	200	9900	175

Table 4.5: RR dimer simulation parameters

Sample	g_x	g_y	g_z	A_x (MHz)	A_y (MHz)	A_z (MHz)	$gStrain_{x,y}$	$gStrain_z$	$Astrain_{x,y}$	$Astrain_z$	Weight
RR	2.07	2.07	2.29	50	50	540	0.01	0.01	0.05	1.0	70%
RR	2.06	2.06	2.33	50	50	470	0.01	0.01	0.05	1.0	30%

Table 4.6: RR monomer simulation parameters. The column "weight" indicates the percentage of a species in the simulated spectrum.

The RR dimer values, reported in **Table 4.5**, are slightly different from the VR dimer (see **Table 4.1**) suggesting a different dimer structure. In fact, the distance between the two paramagnetic centers in the copper resinate is slightly longer than in copper acetate due to the different structure of the ligands: the steric hindrance affects the Cu(II)-Cu(II) distance. These values are slightly different from those reported by Binet [16].

Concerning the monomer signal, the best simulation is obtained supposing the presence of at least two different species, whose EPR parameters are reported in **Table**

4.6. As discussed previously, the nature of the monomer complexes (number and nature of donor atoms) can be extrapolated from the Peisach-Blumberg diagrams. The $g_{//}$ (g_z) and $A_{//}$ (A_z) values are plotted in the diagram (black points, **Figure 4.37**).

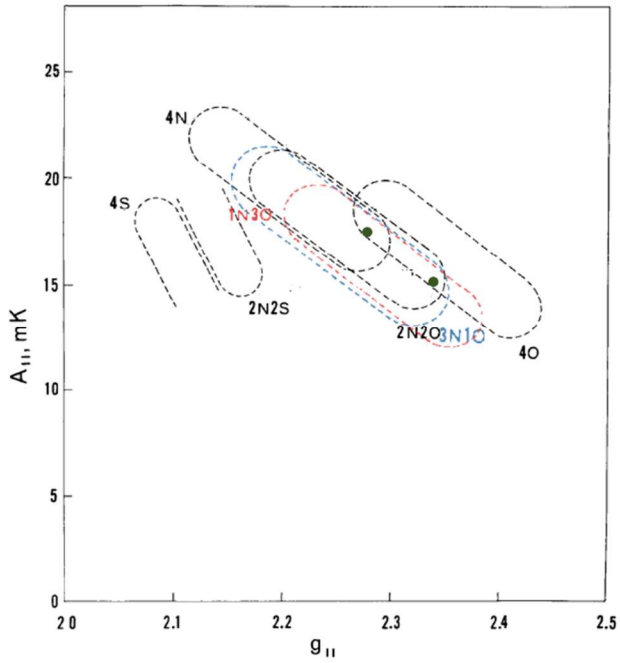

Figure 4.37: Peisach-Blumberg diagram: RR monomer. The black dots mark the g_Z and A_Z values for the monomer copper species present in RR.

The position in the diagram is compatible with different types of equatorial coordination: however, the absence of nitrogen atoms in the resinate indicates a coordination with four oxygen atoms, but with a good covalence character. The resins are mainly composed by diterpenoids such as abietic acid, or isopimaric acid, that have carboxylic functions, and so oxygen atoms, that can complex copper centers. Simulation parameters are similar to VRO5 ones, indicating the same kind of coordination.

EPR spectra for the RR sample were acquired at different temperature (300 K, 250 K, 210 K, 180 K, and 150 K) as shown in **Figure 4.38**.

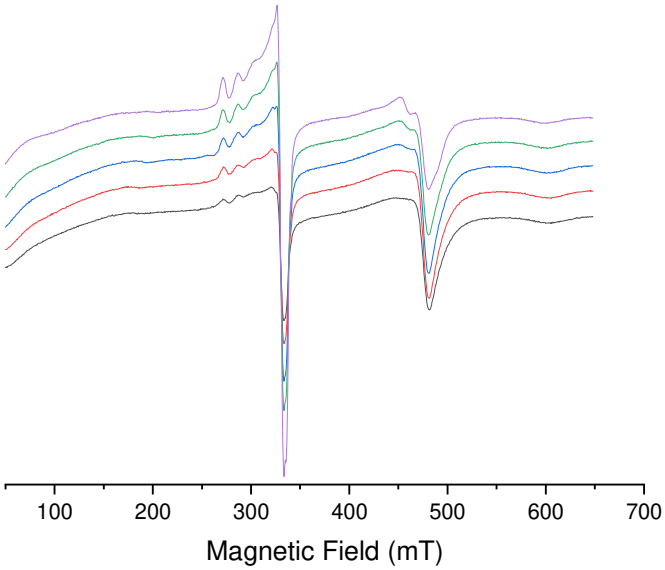

Figure 4.38: RR sanple: 300 K (black line), 250 K (red line), 210 K (blue line), 180 K (green line), and 150 K (purple line**).**

The EPR signals (monomer and dimer) were double integrated to obtain DI, and DI values were plotted against the temperature.

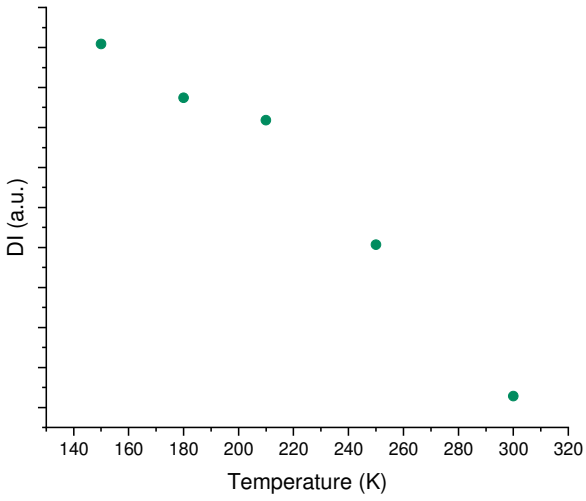

Figure 4.39: DI monomer signal against temperature.

As shown in **Figure 4.39**, the DI values of the monomer signal increase as the

temperature drops down and this trend confirms the paramagnetic nature of the copper monomer according to the Curie law.

Figure 4.40 displays DI trend for the dimer signals at 470 mT (black dots) and 600 mT (red dots).

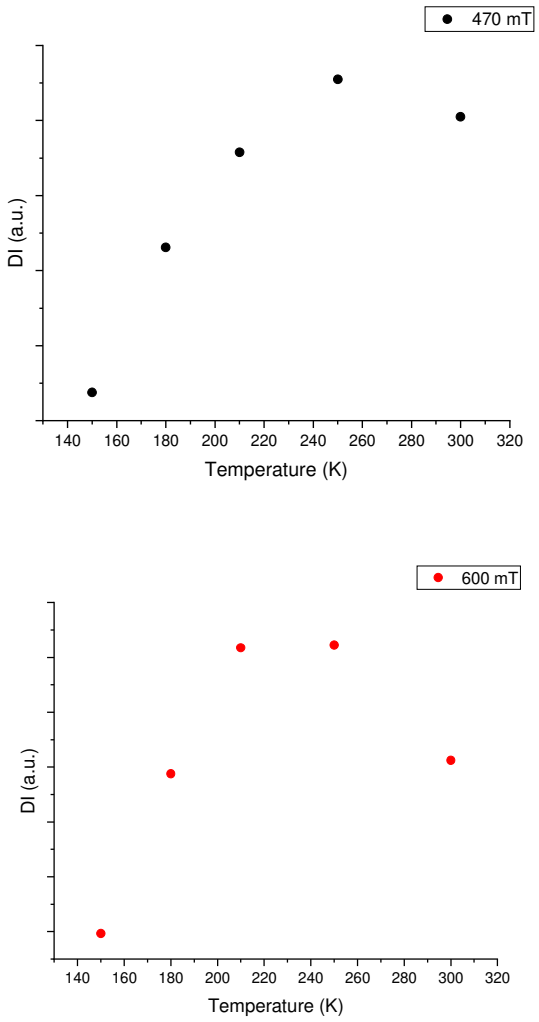

Figure 4.40: DI dimer signal vs temperature: 470 mT (black dots) and 600 mT (red dots)**.**

According to **Figure 4.40**, the DI trends against temperature are equal to those reported for the VR sample: the DI values increase as the temperature goes down until 210K and then decrease under this temperature. Therefore, there is a ferromagnetic-antiferromagnetic transition cooling down the system under 210 K.

The ATR-IR spectrum of RR sample was acquired, and it is shown in **Figure 4.41.**

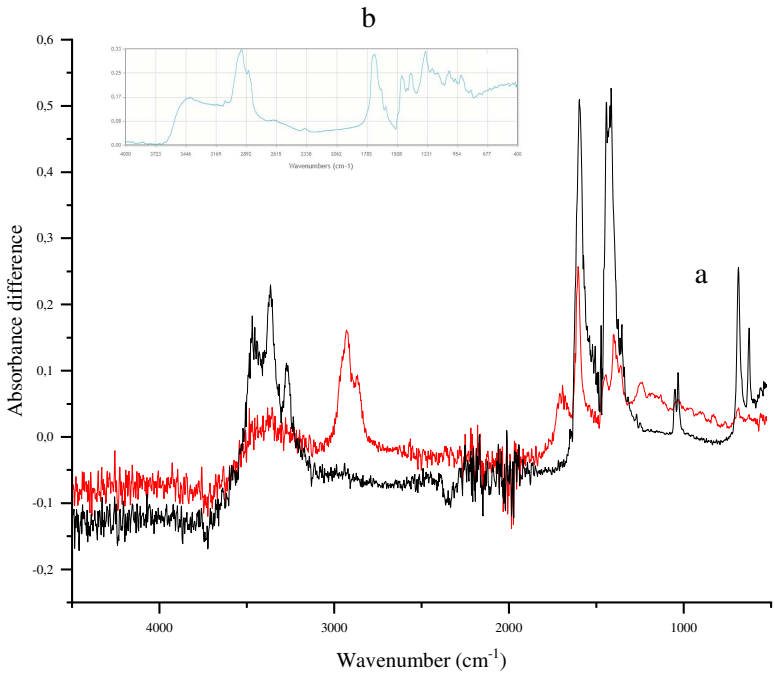

Figure 4.41: a) RR spectrum (red line) and VR spectrum (black line) b) Venice turpentine (natural resin) spectrum from IRUG database.

The ATR-IR spectrum of RR sample is characterized by typical signals of copper carboxylate (see **Table 4.2**). Moreover, the characteristic signals of natural resin (Venice turpentine) are evident in the spectrum comparing the experimental spectrum with the reference one (**Figure 4.41 b**).

4.2.2 Copper resinate mixtures

The EPR spectra of pigment/binder with a 1:3 ratio were acquired at room temperature and are collected in **Figure 4.42**.

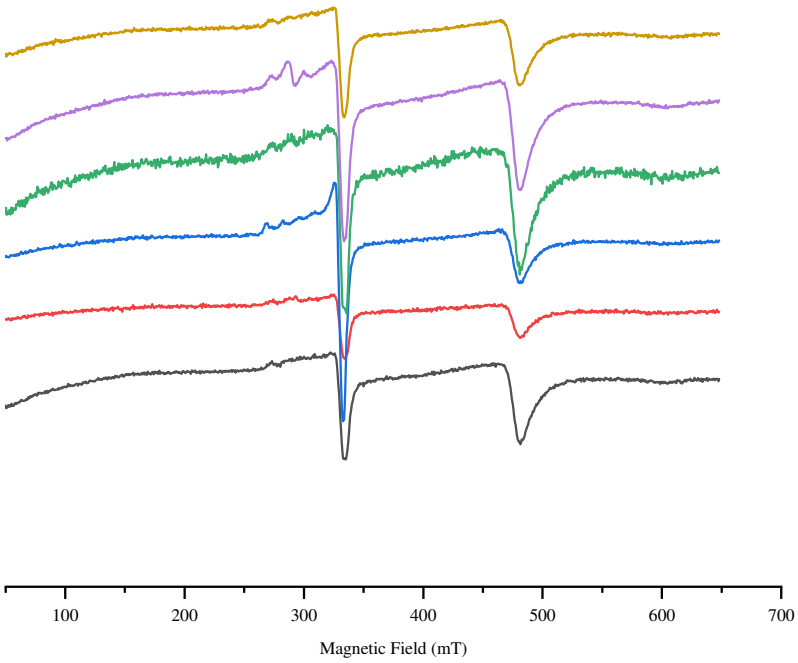

Figure 4.42: CW-EPR (X-band) spectra at room temperature: RRY (yellow line), RREY (purple line), RRO (green line), RRG (blue line), RREW (red line) and RRC (black line).

Same consideration made for the verdigris samples can be done also for copper resinate ones. The spectrum changes with different binders, confirming the different way and strength of the binder to complex the copper atoms. Linseed oil seems one more time to be the worst binder looking at dimer signal intensity. Therefore, fatty acids are not able to complex efficiently single copper centers, breaking the dimer species. Moreover, the dimer signals remain quite intense due to the high pigment/binder ratio, as observed for verdigris-binder combination. The monomer signals are quite intense, but this is due to the monomer already detected in the raw pigment, and derives from the natural resin complexation.

The CW-EPR spectra at room temperatures of the samples with 5% pigment/binder ratio were acquired (**Figure 4.43**). The large amount of binder should give rise to even more intense monomer signal.

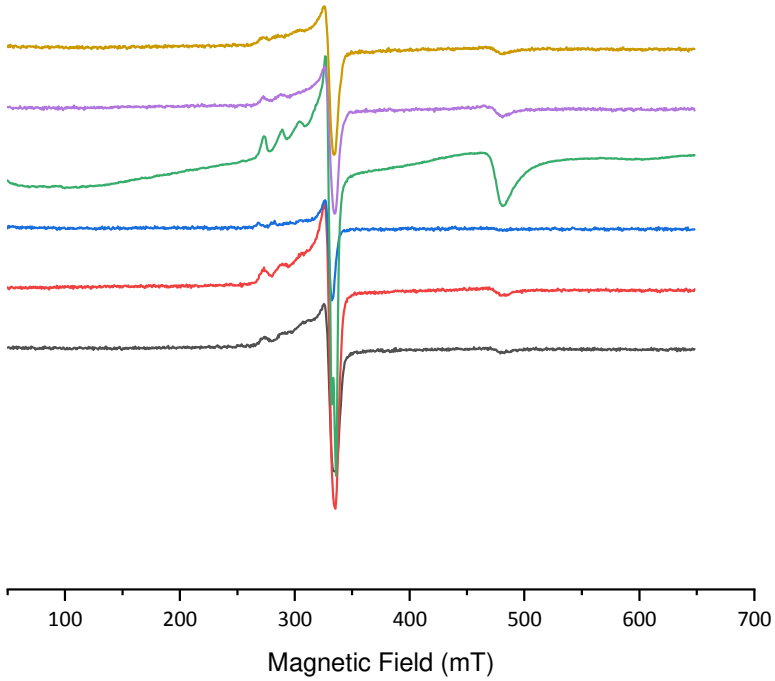

Figure 4.43: CW-EPR (X-band) spectra at room temperature: RRY5 (yellow line), RREY5 (purple line), RRO5 (green line), VRG5 (blue line), RREW5 (red line) and RRC5 (black line).

As expected, and observed for the verdigris-binder combinations, the dimer signals decrease their intensity until almost disappear in most cases, especially the signal at 600 mT, and at the same time, the monomer signals increase. The spectra are reported in **Figure 4.44** in the 225 – 430 mT spectral region to display the monomer region and its typical quartet pattern.

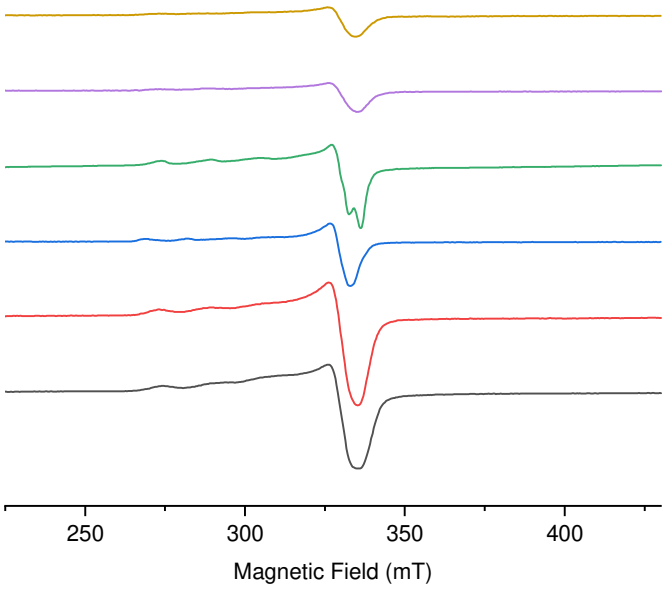

Figure 4.44: CW-EPR (X-band) spectra at room temperature: RRY5 (yellow line), RREY5 (purple line), RRO5 (green line), RRG5 (blue line), RREW5 (red line) and RRC5 (black line).

The quartet pattern is evident in all spectra. It is also clear that changing the binder, the pattern of the signal changes. The spectra were simulated to estimate factor g and hyperfine constant A values. Simulation graphs are listed below (**Figure 4.45 – 4.50)** and the simulation parameters are collected in **Table 4.7**.

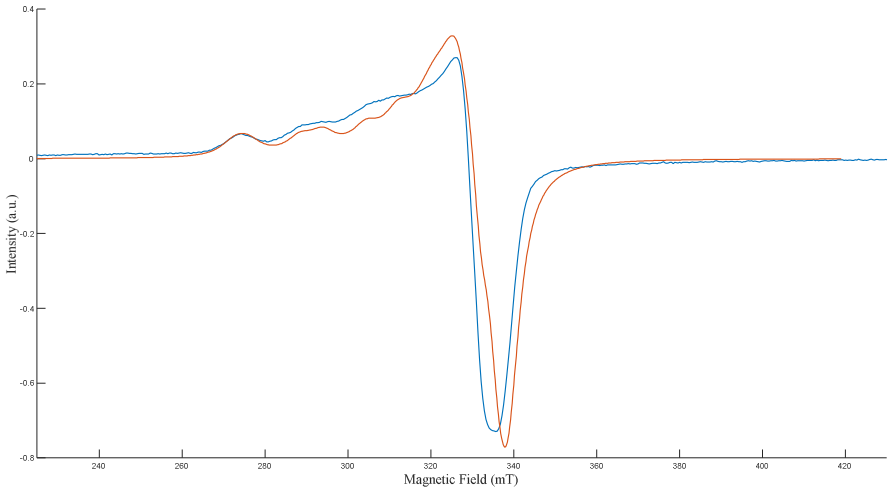

Figure 4.45: RRY5 sample: simulated spectrum (red line) and experimental spectrum (blue line).

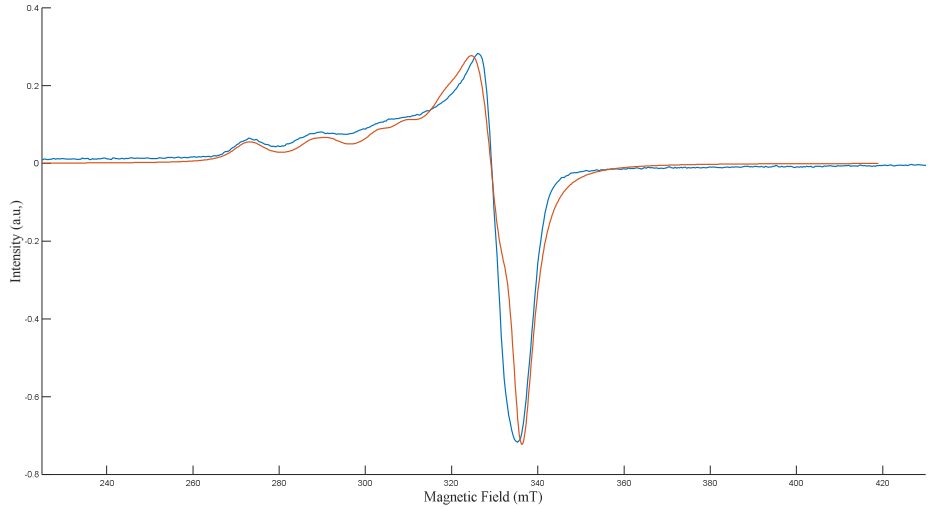

Figure 4.46: **R**REY5 sample: simulated spectrum (red line) and experimental spectrum (blue line).

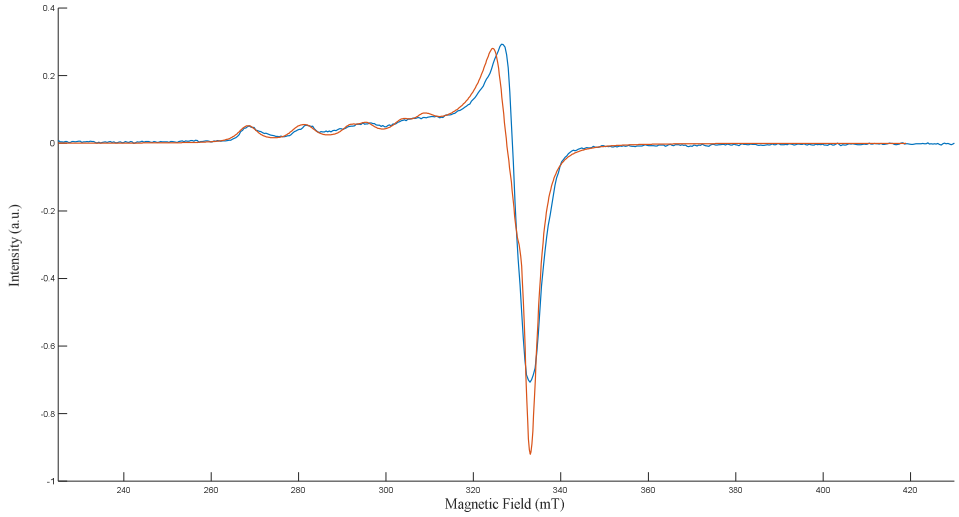

Figure 4.47: RRG5 sample: simulated spectrum (red line) and experimental spectrum (blue line).

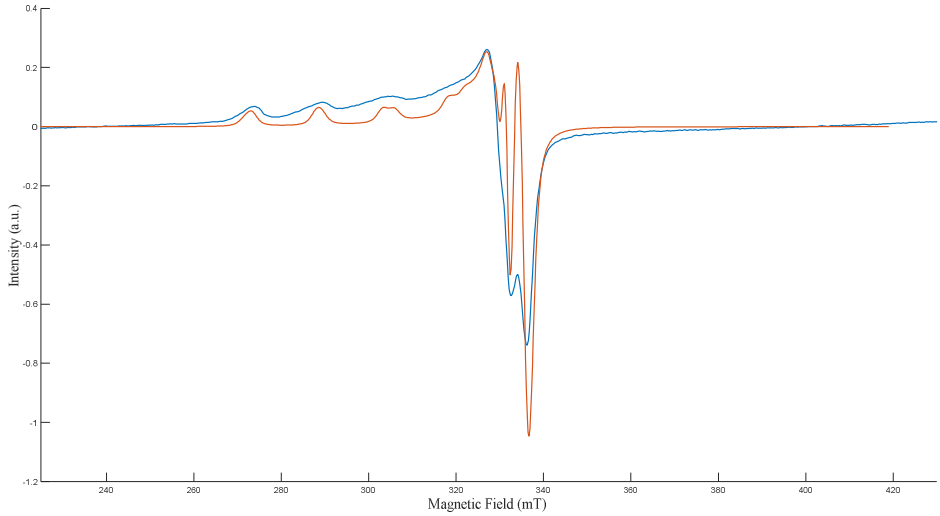

Figure 4.48: RRO5 sample: simulated spectrum (red line) and experimental spectrum (blue line).

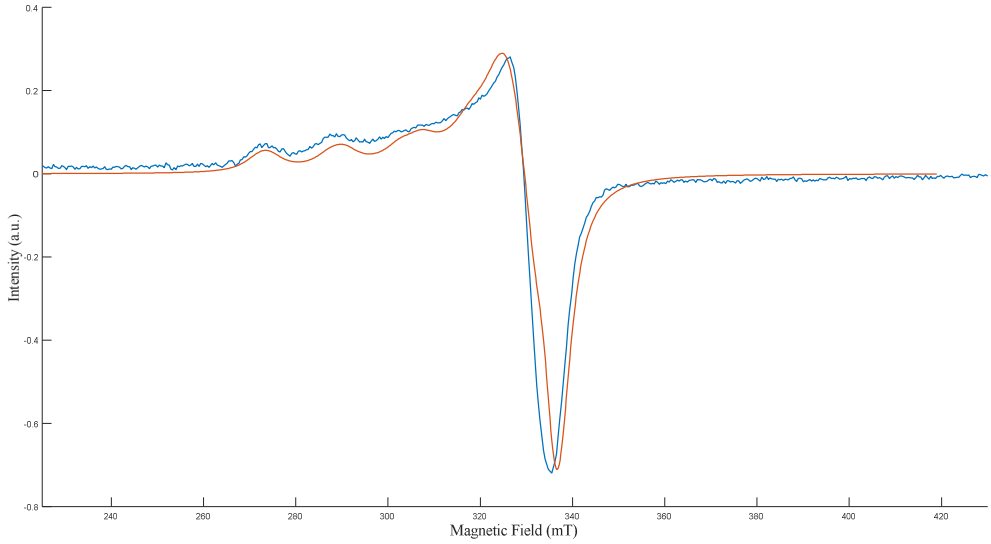

Figure 4.49: **R**REW5 sample: simulated spectrum (red line) and experimental spectrum (blue line).

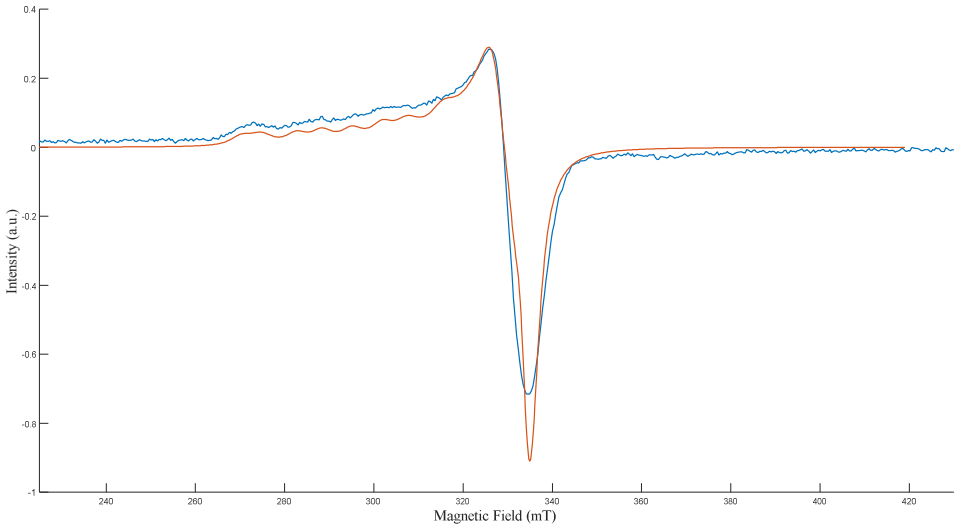

Figure 4.50: RRC5 sample: simulated spectrum (red line) and experimental spectrum (blue line).

Sample	**RRO5**		**RRG5**		**RRC5**		**RREW5**		**RRY5**		**RREY5**	
Species	1	2	1	2	1	2	1	2	1	2	1	2
g_x	2.06	2.06	2.07	2.07	2.06	2.06	2.06	2.06	2.06	2.06	2.06	2.07
g_y	2.06	2.06	2.07	2.07	2.06	2.06	2.06	2.06	2.06	2.06	2.06	2.07
g_z	2.29	2.31	2.36	2.39	2.36	2.31	2.31	2.29	2.25	2.30	2.31	2.27
A_x (MHz)	58	58	50	50	50	58	50	58	50	58	50	58
A_y (MHz)	34	34	50	50	50	34	50	34	50	34	50	34
A_z (MHz)	520	480	430	390	400	430	480	520	560	500	490	520
$gStrain_{x,y}$	0.005	0.005	0.005	0.005	0.005	0.005	0.005	0.005	0.005	0.005	0.005	0.005
$gStrain_z$	0.01	0.01	0.01	0.01	0.01	0.01	0.01	0.01	0.01	0.01	0.01	0.01
$Astrain_{x,y}$ (MHz)	0.5	0.5	0.5	0.5	0.5	0.5	0.5	0.5	0.5	0.5	0.5	0.5
$Astrain_z$ (MHz)	1.0	1.0	1.0	1.0	1.0	1.0	1.0	1.0	1.0	1.0	1.0	1.0
Weight	56%	44%	50%	50%	50%	50%	50%	50%	50%	50%	56%	44%

Table 4.7: Simulation parameters for all samples: RRO5, RRG5, RRC5, RREW5, RRY5 and RREY5 at room temperature. The row "weight" indicates the percentage of a species in the simulated spectrum.

Comparing **Table 4.6** and **Table 4.7**, the monomeric complexes present in the raw copper resinate have different magnetic parameters than in the pigment-binder combinations. Some binders have similar magnetic parameters (e.g., RRO5 and RREY5) suggesting the same kind of complexation. Some parameters are equal to some verdigris complexes (see **Table 4.3**): this suggests that the binder complexes the copper center in the same way, regardless of the starting pigment. The A_z ($A_{//}$) and the g_z ($g_{//}$) for the copper resinate-binder complexes are plotted in the Peisach-Blumberg diagram (**Figure 4.51**).

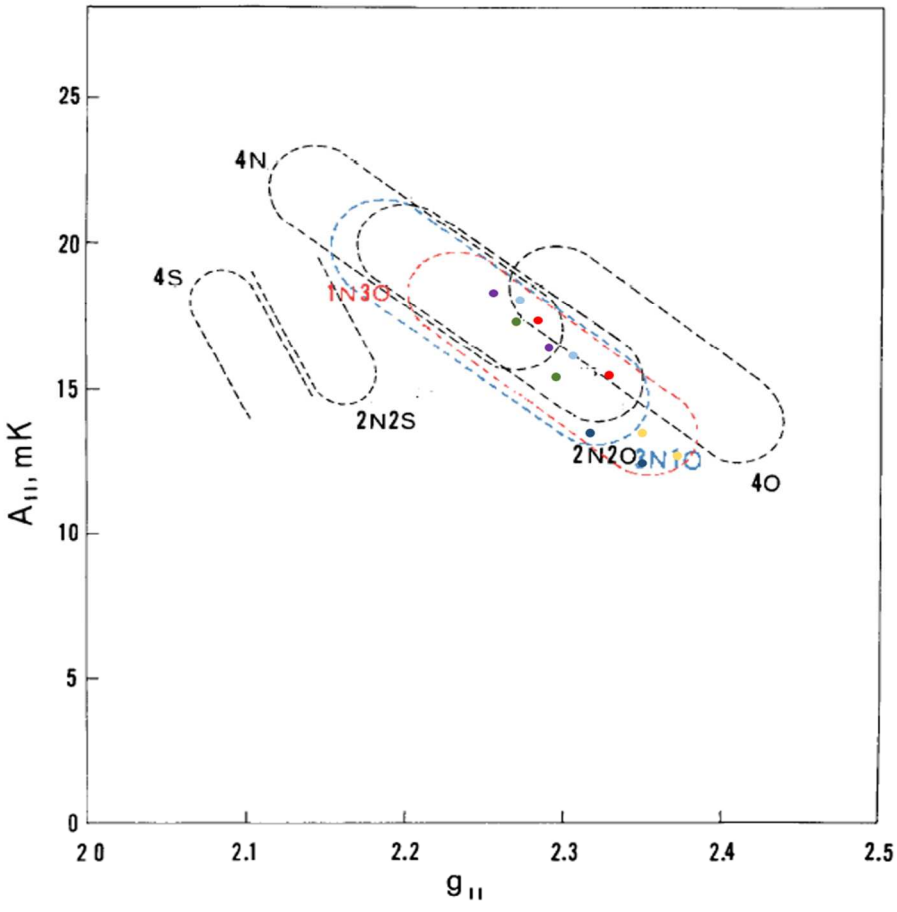

Figure 4.51: Peisach-Blumberg diagram: RRO5 (red dots), RRC5 (blue dots), RRG5 (yellow dots), RREW (green dots), RRY5 (purple dots) and RREY5 (light blue dots).

The considerations made for verdigris are valid also for copper resinate. The different binders give rise to the same kind of complexes simulated with verdigris. Therefore, fatty acid binders involve more oxygen atoms in the complexation, while protein binders more nitrogen atoms. The number of oxygen and nitrogen atoms involved in the complexes is difficult to establish clearly because of overlapping assignment regions.

Other CW-EPR spectra for the 5% pigment/binder ratio samples were acquired at different temperatures (250 K, 210 K, 180 K, and 150 K) to resolve better the hyperfine pattern and to verify if simulation parameters change with temperature (see from **Figure 4.52** to **Figure 4.57**): the 150 K spectra were simulated.

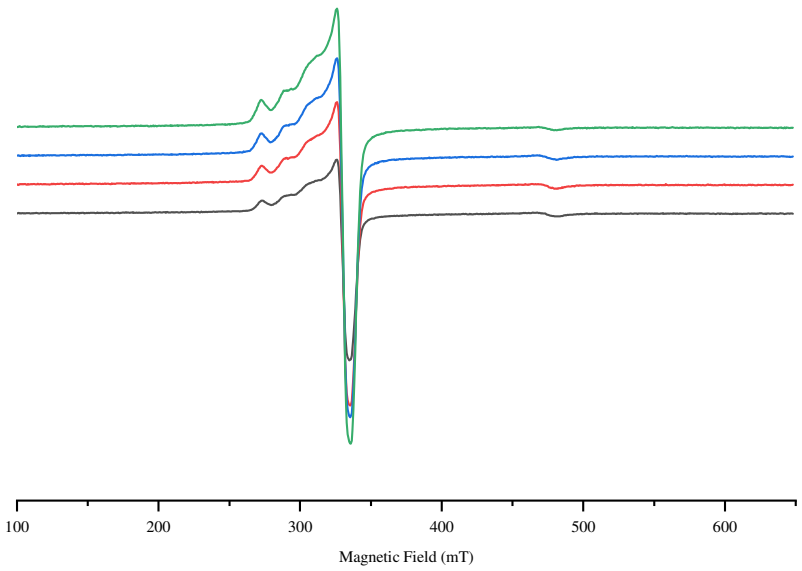

Figure 4.52: RRY5 sample: 150K (green line), 180K (blue line), 210K (red line) and 250K (black line).

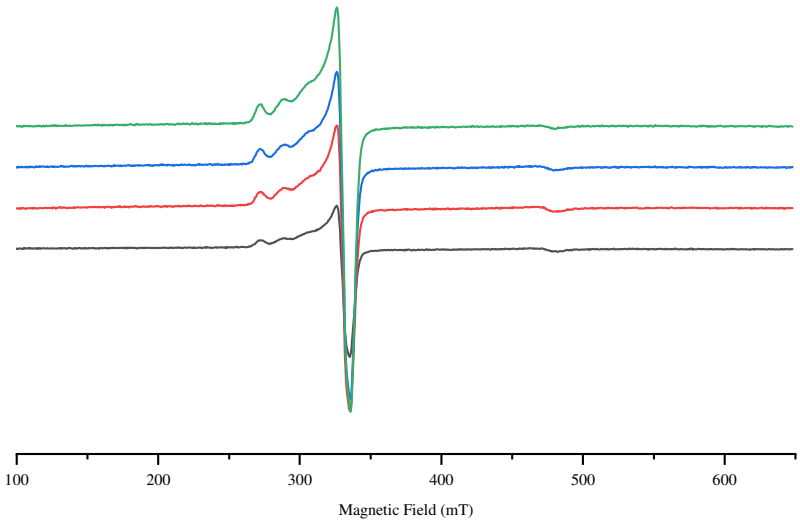

Figure 4.53: RREY5 sample: 150K (green line), 180K (blue line), 210K (red line) and 250K (black line).

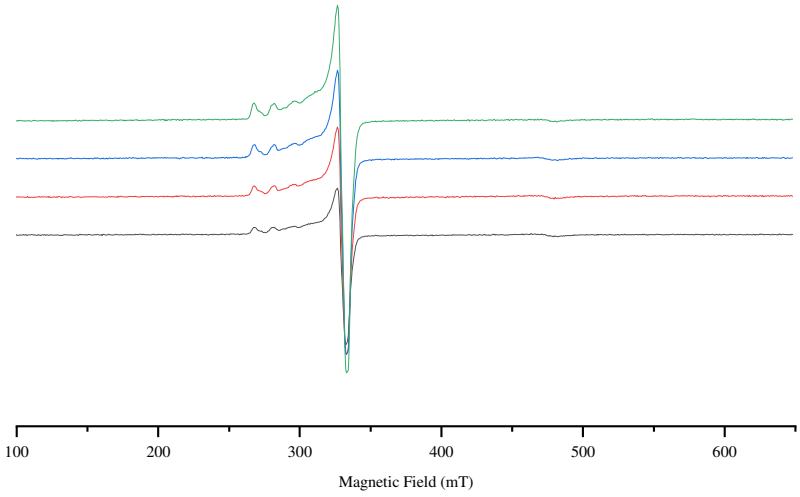

Figure 4.54: RRG5 sample: 150K (green line), 180K (blue line), 210K (red line) and 250K (black line).

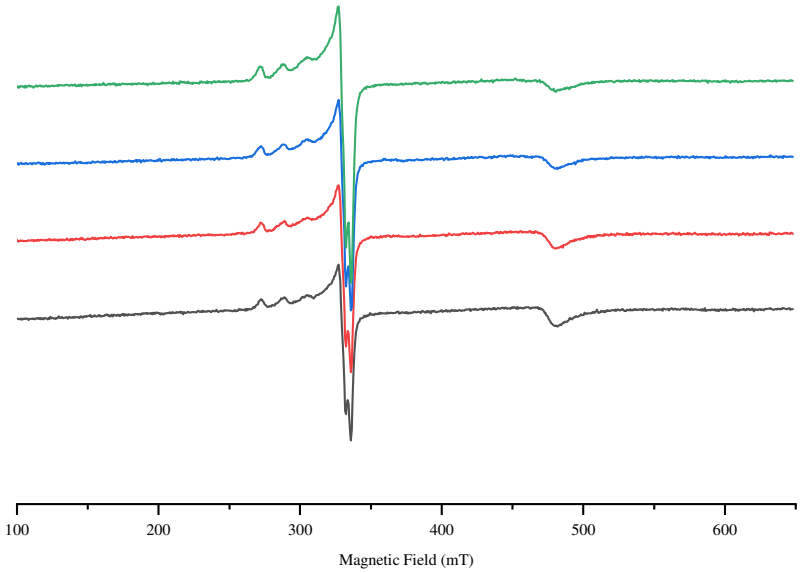

Figure 4.55: RRO5 sample: 150K (green line), 180K (blue line), 210K (red line) and 250K (black line).

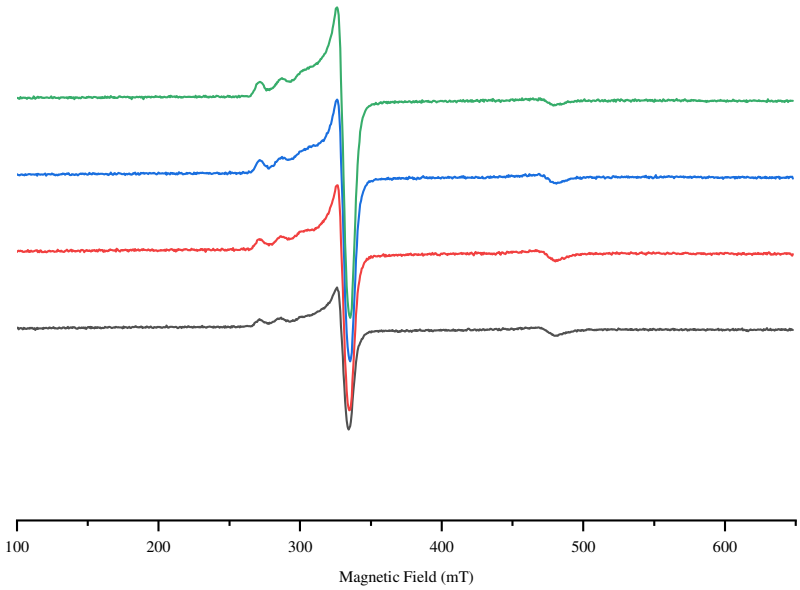

Figure 4.56: RREW5 sample: 150K (green line), 180K (blue line), 210K (red line) and 250K (black line).

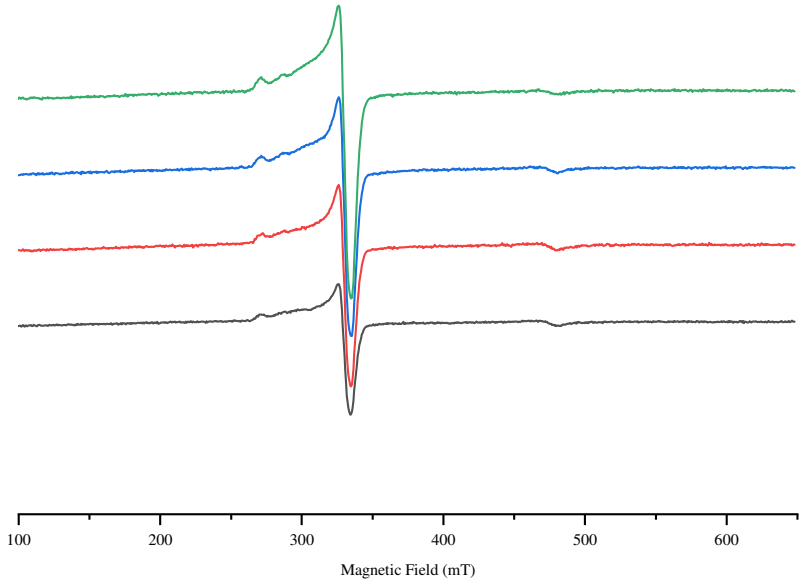

Figure 4.57: RRC5 sample: 150K (green line), 180K (blue line), 210K (red line) and 250K (black line).

On lowering temperature, the same trend for the verdigris samples is observed: the dimer signal decreases its intensity, while the monomer one increases in all samples. As seen in verdigris samples, the quartet lines of the monomeric species become broader lowering the temperature, indicating that at high temperature the copper complexes rearrange quickly, with dynamical averaging of the magnetic parameters and motional narrowing. The DI values for both monomer (**Figure 4.58**) and dimer (**Figure 4.59**) signals were calculated and plotted against the temperature.

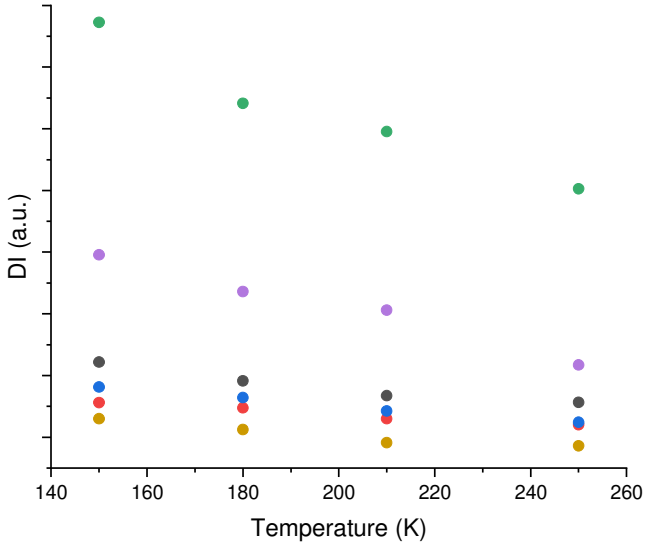

Figure 4.58: DI of monomer signal (330 mT) vs temperature: RRC5 (red dots), RREW5 (blue dots), RRY5 (green dots), RREY5 (purple dots) and RRO5 (yellow dots).

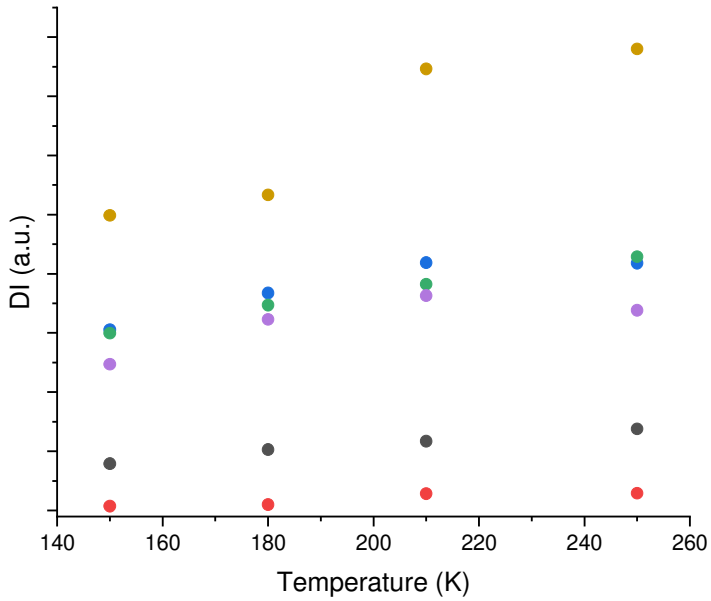

Figure 4.59: DI of dimer signal (470 mT) vs temperature: RRC5 (red dots), RREW5 (blue dots), RRY5 (green dots), RREY5 (purple dots) and RRO5 (yellow dots).

The general trend of the monomer signals is to increase when the temperature goes down; this indicated the paramagnetic nature of the monomer according to the Curie

law. Meanwhile, the trends observed for the dimer signals are a bit different from those observed for verdigris mixtures. The strongest DI changes are observed for the RRO5 sample, but there is no clear evidence of an antiferromagnetic-ferromagnetic transition (no DI maximum at 210 K). On the other hand, the dimer present in the other samples shows a decrease of DI on lowering temperature, indicative of an antiferromagnetic interaction (i.e., the stable state is antiferromagnetic, with the ferromagnetic state being the excited one).

The simulations of the spectra at 150 K are displayed below (**Figure 4.60-Figure 3.65**), and the simulation parameters are collected in **Table 4.8**.

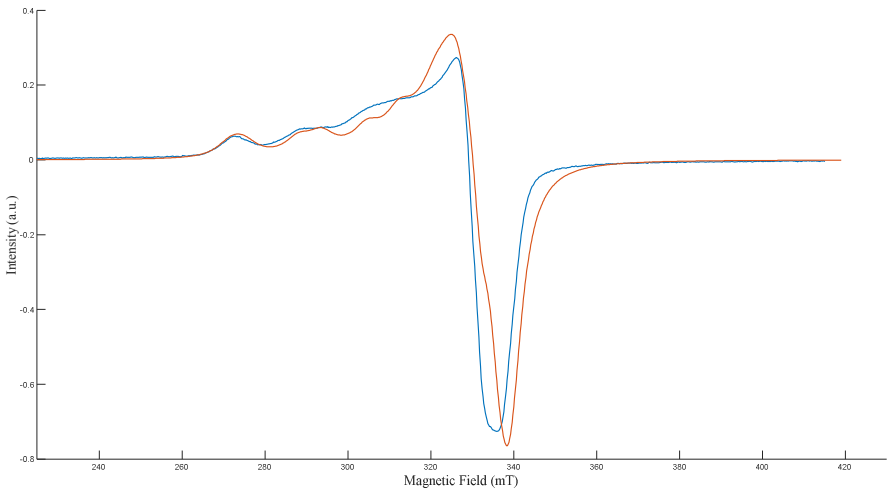

Figure 4.60: RRY5 150K sample: simulated spectrum (red line) and experimental spectrum (blue line).

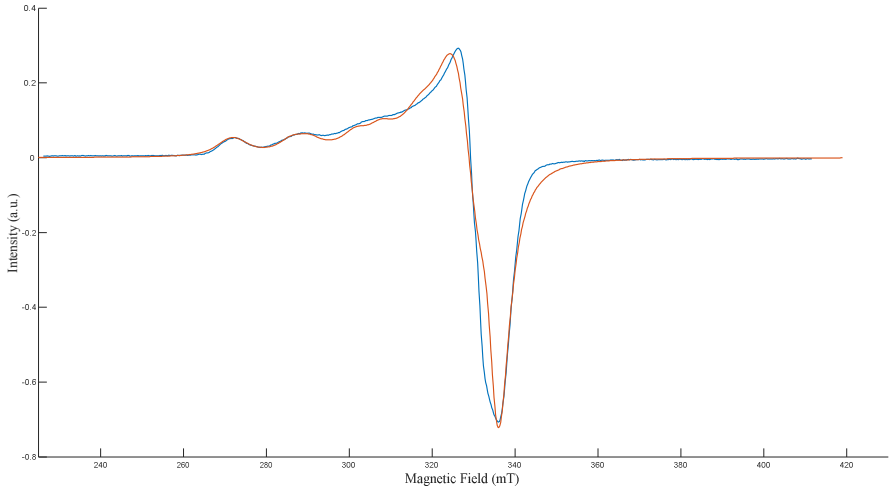

Figure 4.61: RREY5 150K sample: simulated spectrum (red line) and experimental spectrum (blue line).

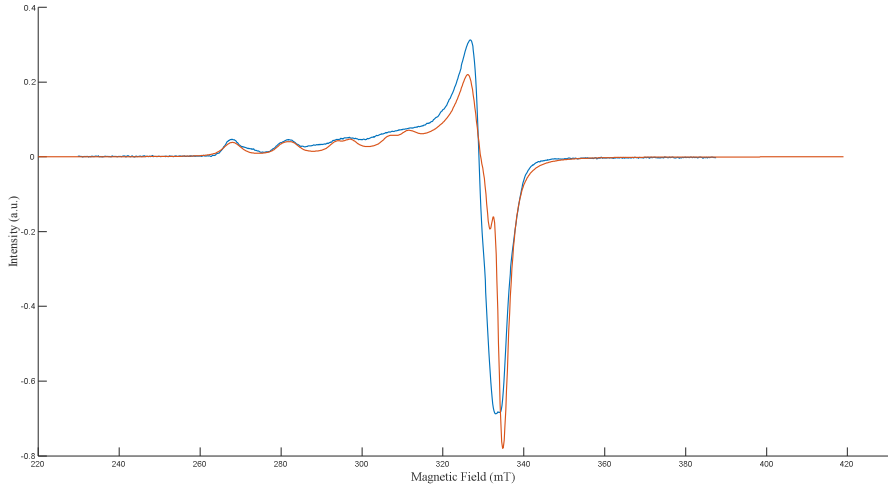

Figure 4.62: RRG5 150K sample: simulated spectrum (red line) and experimental spectrum (blue line).

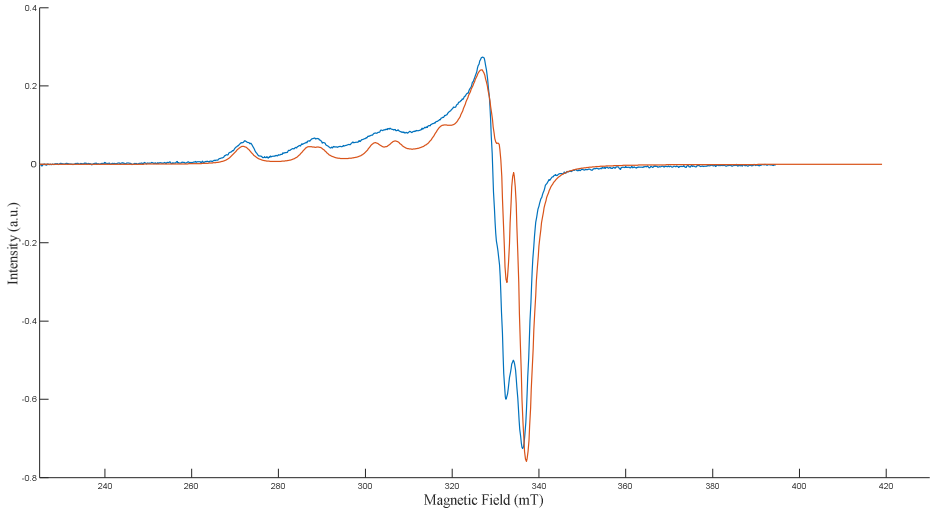

Figure 4.63: RRO5 150K sample: simulated spectrum (red line) and experimental spectrum (blue line).

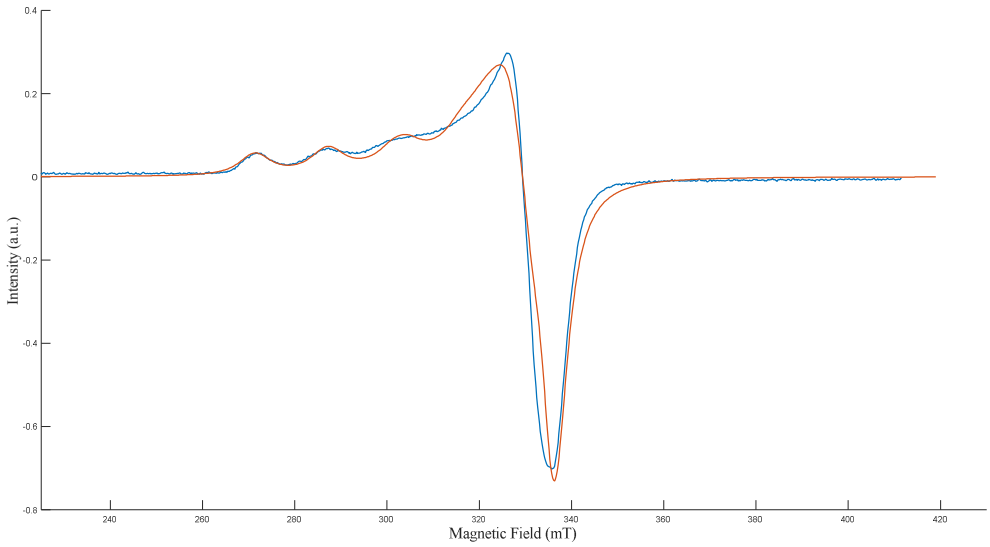

Figure 4.64: RREW5 150K sample: simulated spectrum (red line) and experimental spectrum (blue line).

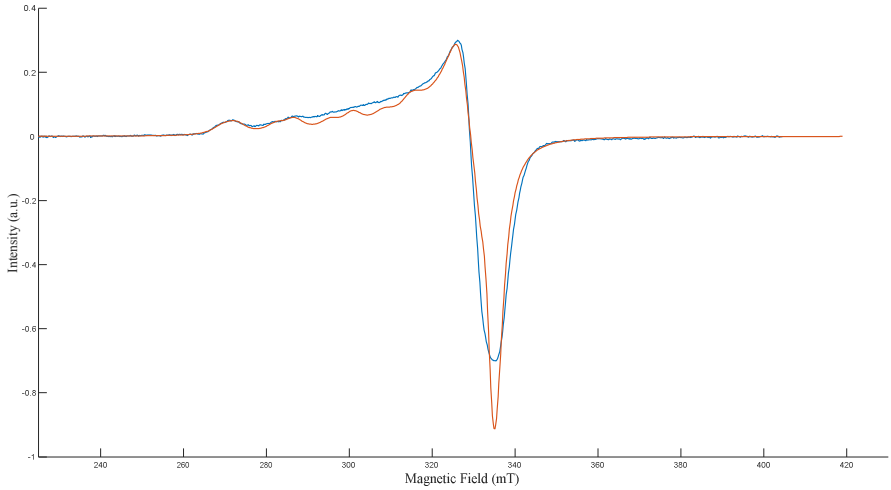

Figure 4.65: VRC5 150K sample: simulated spectrum (red line) and experimental spectrum (blue line).

Sample	**RRO5**		**RRG5**		**RRC5**		**RREW5**		**RRY5**		**RREY5**	
Species	1	2	1	2	1	2	1	2	1	2	1	2
g_x	2.06	2.06	2.07	2.07	2.06	2.06	2.06	2.06	2.06	2.06	2.06	2.07
g_y	2.06	2.06	2.07	2.07	2.06	2.06	2.06	2.06	2.06	2.06	2.06	2.07
g_z	2.29	2.32	2.35	2.38	2.36	2.32	2.32	2.30	2.25	2.30	2.32	2.28
A_x (MHz)	58	58	50	50	50	58	50	58	50	58	50	58
A_y (MHz)	34	34	50	50	50	34	50	34	50	34	50	34
A_z (MHz)	540	490	460	430	420	450	480	520	580	520	490	540
$gStrain_{x,y}$	0.005	0.005	0.005	0.005	0.005	0.005	0.005	0.005	0.005	0.005	0.005	0.005
$gStrain_z$	0.01	0.01	0.01	0.01	0.01	0.01	0.01	0.01	0.01	0.01	0.01	0.01
$Astrain_{x,y}$ (MHz)	0.5	0.5	0.5	0.5	0.5	0.5	0.5	0.5	0.5	0.5	0.5	0.5
$Astrain_z$ (MHz)	1.0	1.0	1.0	1.0	1.0	1.0	1.0	1.0	1.0	1.0	1.0	1.0
Weight	56%	44%	50%	50%	42%	58%	56%	44%	50%	50%	56%	44%

Table 4.8: Simulation parameters for all samples: RRO5, RRG5, RRC5, RREW5, RRY5 and RREY5 at 150K of temperature. The row "weight" indicates the percentage of a species in the simulated spectrum.

As seen for the verdigris-binder combinations, a slight increase for both g-factor and hyperfine constant is observed on lowering temperature, but the variation is small.

The ATR-IR spectra of the 5% samples were acquired (**Figure 4.66**).

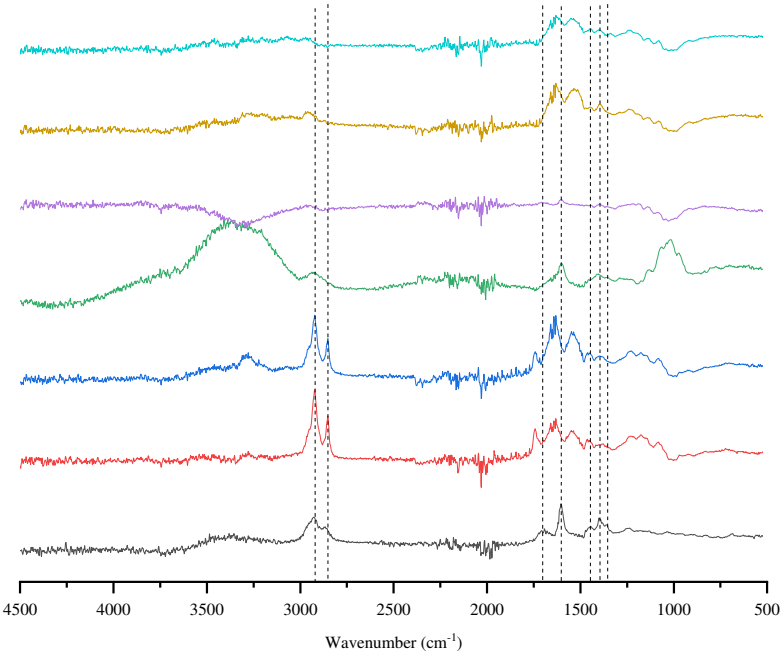

Figure 4.66: ATR-IR spectra: RR (black line), RRY5 (red line), RREY5 (blue line), RRG5 (green line), RRO5 (purple line), RREW5 (yellow line) and RRC5 (turquoise line).

The ATR-IR spectra are consistent with the EPR results. Binder signals are present in the spectra. In some cases, the same signals observed for pure copper resinate are evident, suggesting that the same copper-resinate dimer is still present in the sample, e.g., in RRO5 and RRG5 samples. In the other samples, small differences from the raw pigment are noticeable in the spectral region around 1600 cm^{-1}, as shown for verdigris. These spectral peculiarities suggest the different bonding of ligands and therefore indicate the formation of new complexes with respect to the complexes observed in the raw copper-resinate pigment.

4.3 Malachite

4.3.1 Raw pigment (LM and SLM samples)

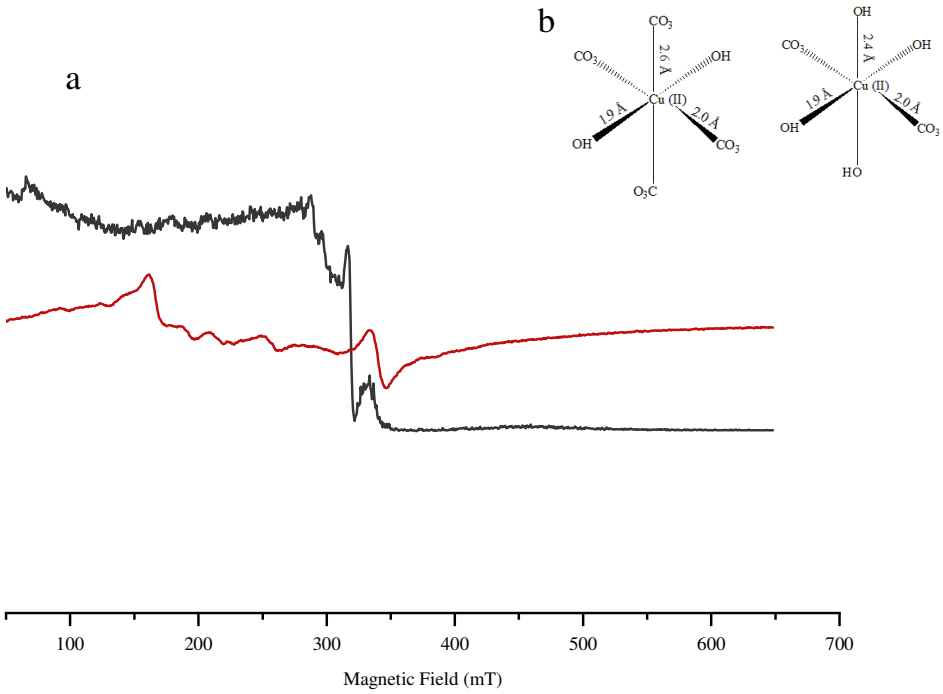

Figure 4.67: a) CW-EPR spectrum (X-band) of LM (red line) and SLM (black line), b) structure of the copper centers in malachite.

Figure 4.67 displays the natural malachite spectrum (red line). The spectrum is quite complicated: the signal at 350 mT is a typical pseudo-octahedral Fe(III) signal. In the region below 300 mT, the spectrum is very crowded with many signals difficult to assign. Probably these features are related to the presence of iron and copper oxides (superparamagnetic species), commonly present in the natural pigment. At 150 mT appears a signal from rhombic Fe(III). The synthetic malachite spectrum is quite different from the natural one. The pseudo-octahedral Fe (III) signal is shifted at lower magnetic fields while the features under 300 mT seem to be less intense but still present. The rhombic Fe (III) signal seems not to be present. Both the synthetic and

the natural malachite spectra do not show copper typical features, indicating a dominating antiferromagnetic interaction between the Cu(II) ions.

The XRF spectra of LM and SLM samples confirm the presence of iron (see **Figure 4.68** and **Figure 4.69**) even in if the amount in the SLM sample is smaller.

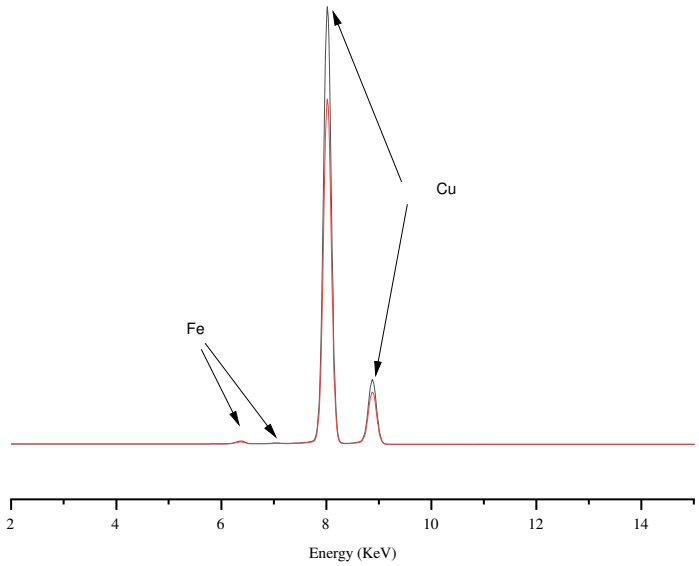

Figure 4.68: XRF spectrum of LM sample.

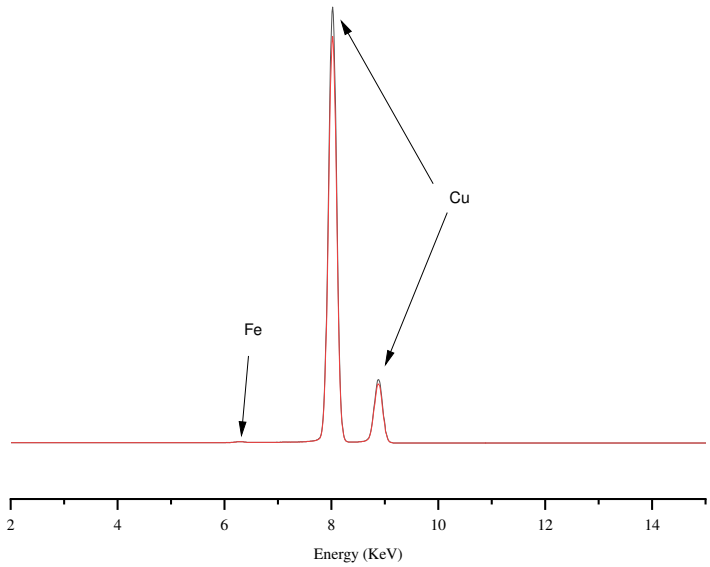

Figure 4.69: XRF spectrum of SLM sample.

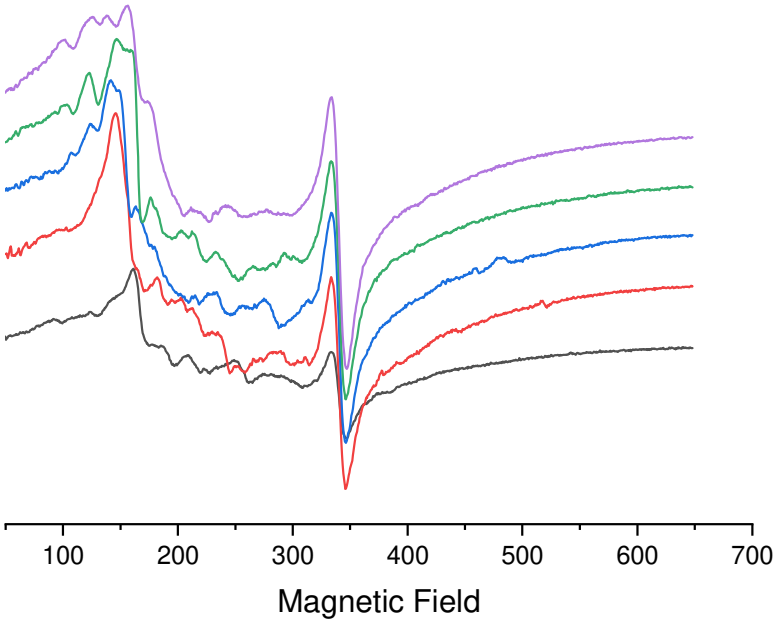

Figure 4.70: LM sample: 300K (black line), 250K (red line), 210K (blue line), 180K (green line) and 150K (purple line).

Figure 4.70 displays the EPR spectra of the sample LM acquired at different temperature (300 K, 250 K, 210 K, 180 K and 150 K). The pseudo-octahedral Fe (III) signal increases its intensity on lowering temperature, while the rhombic it is partially covered by iron oxides signals. In the spectral region below 300 mT the assignation is practically impossible: the spectrum is very crowded, and each signal has its own trend. In any case, a signal at 230 mT seems not to change so much, this confirms the presence of copper oxides [30, 31].

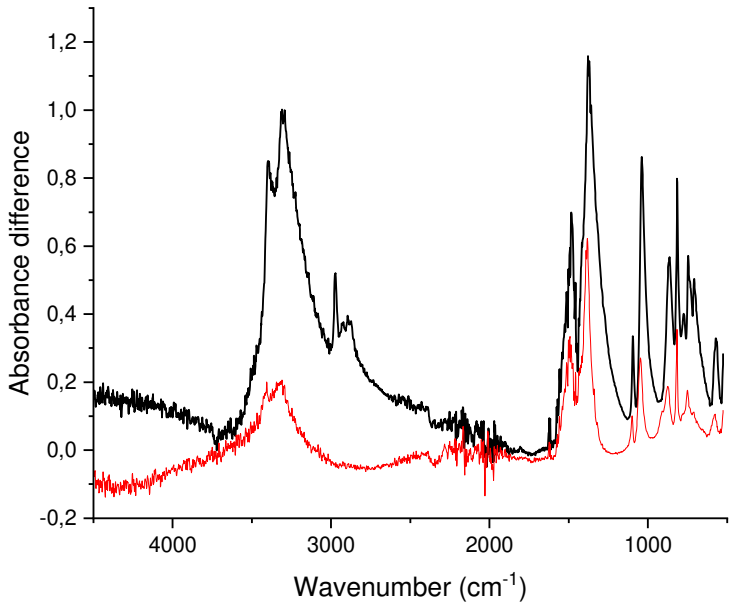

Figure 3.71: LM (black line) and SLM ATR-IR spectrum (red line).

The ATR-IR spectra of LM and SLM sample are shown in **Figure 4.71**. There is no difference between them in the spectral region below 2000 cm^{-1}: both show typical signals related to a carbonate compound. In the LM spectrum, there are some signals around 3000 cm^{-1} assignable to impurities (probably, organic compounds). Principal vibrational modes are listed in **Table 4.9**.

Signal wavenumber (cm^{-1})	**Chemical function**	**Type of vibration**
3000-3500	-OH	Stretching
1494 and 1380	$-CO_3^{2-}$	Asymmetric stretching
1097	$-CO_3^{2-}$	Symmetric stretching
1047 and 869	-OH	Out-of-plan bending
815	$-CO_3^{2-}$	In-plane bending
748 and 712	$-CO_3^{2-}$	Out-of-plane bending
578	Cu-O	Stretching

Table 4.9: ATR-IR signals of LM and SLM sample [32].

4.3.2 Malachite mixtures

The EPR spectra of pigment/mixtures with a 1:3 ratio were acquired at room temperature and are collected in **Figure 4.72**.

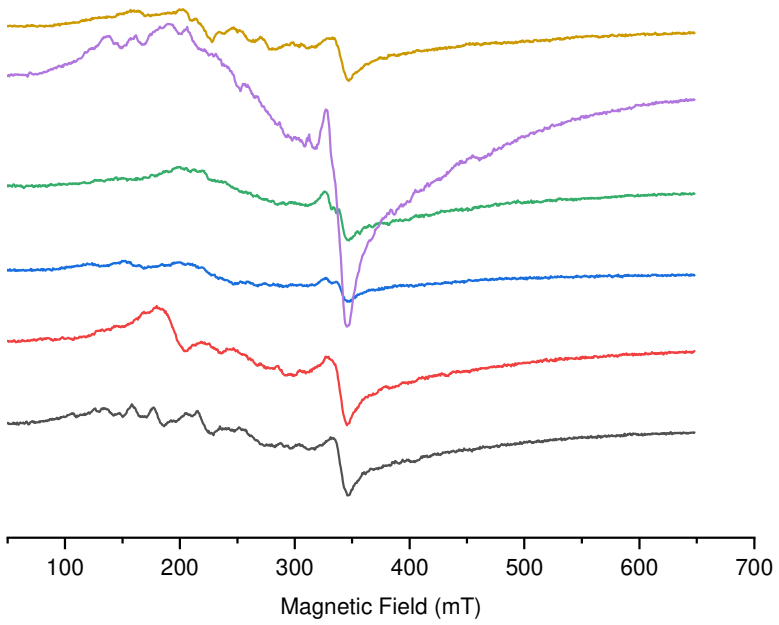

Figure 4.72: CW-EPR (X-band) spectra at room temperature: LMY (yellow line), LMEY (purple line), LMO (green line), LMG (blue line), LMEW (red line) and LMC (black line).

It is very difficult to appreciate significant changes in the spectra with different binders, due to the many spurious signals of the malachite pigment. Probably there are some features related to copper complexes but are covered by the strong pseudo-octahedral Fe (III) signal. It is still noticeable the rhombic Fe (III) signal in many spectra. Surely, the spectra seem to become more complicated by adding the binder to the raw pigment.

The CW-EPR spectra at room temperatures of the samples with 5% pigment/binder ratio were acquired (**Figure 4.73**). In some spectra, the features related to copper monomers appear, in particular with protein-based binders, but the signal is still

heavily affected by the Fe(III) signal. Arabic gum shows a good complexation strength. Oxides features are still observable even if less intense. For these reasons, only a few spectra were simulated with EasySpin software in order to obtain factor g and hyperfine constant A values (see from **Figure 4.74** to **Figure 4.77**).

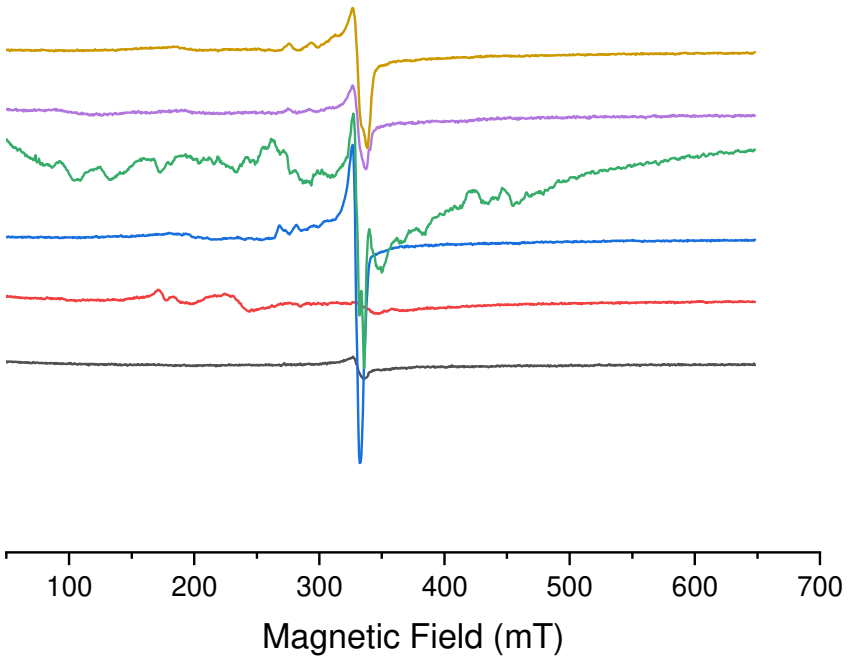

Figure 4.73: CW-EPR (X-band) spectra at room temperature: LMY5 (yellow line), LMEY5 (purple line), LMO5 (green line), LMG5 (blue line), LMEW5 (red line) and LMC5 (black line).

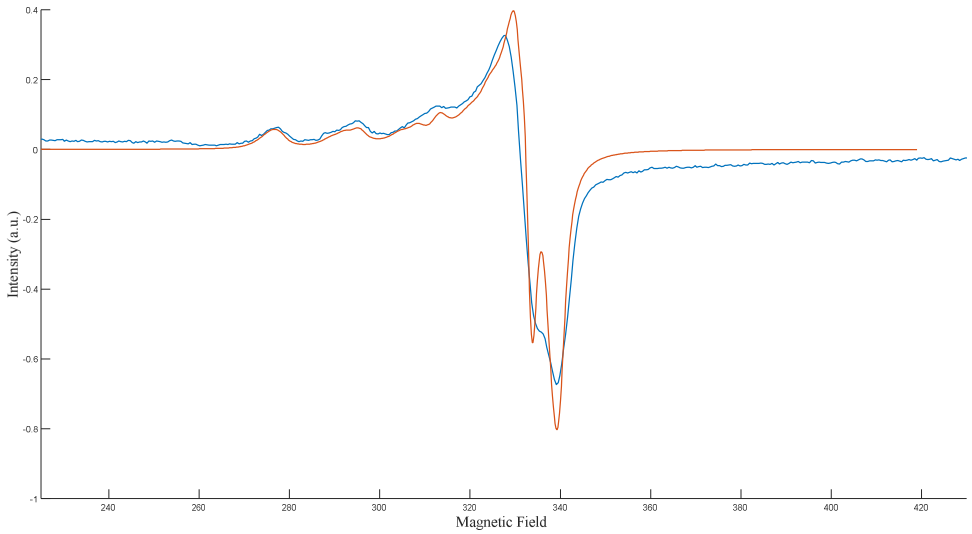

Figure 4.74: LMY5 sample: simulated spectrum (red line) and experimental spectrum (blue line).

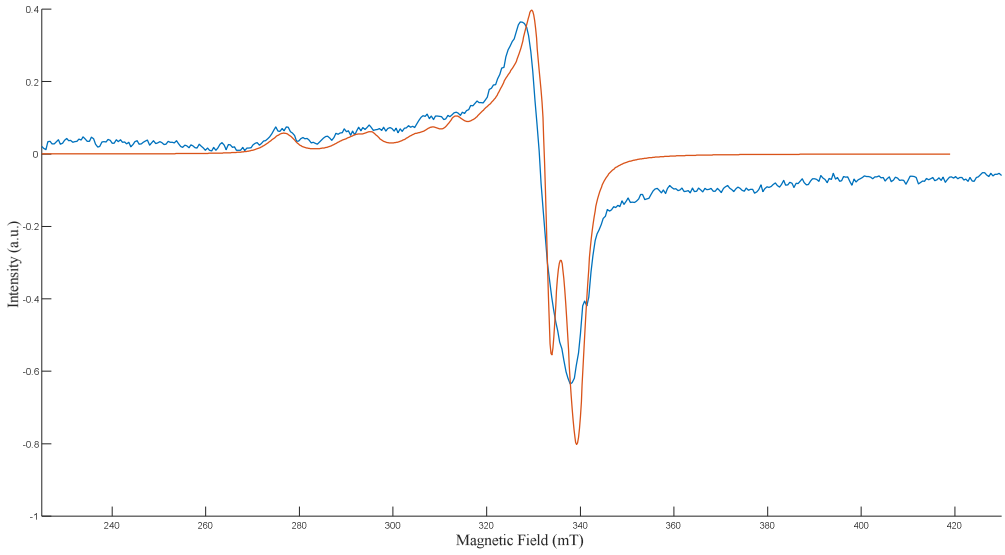

Figure 4.75: LMEY5 sample: simulated spectrum (red line) and experimental spectrum (blue line).

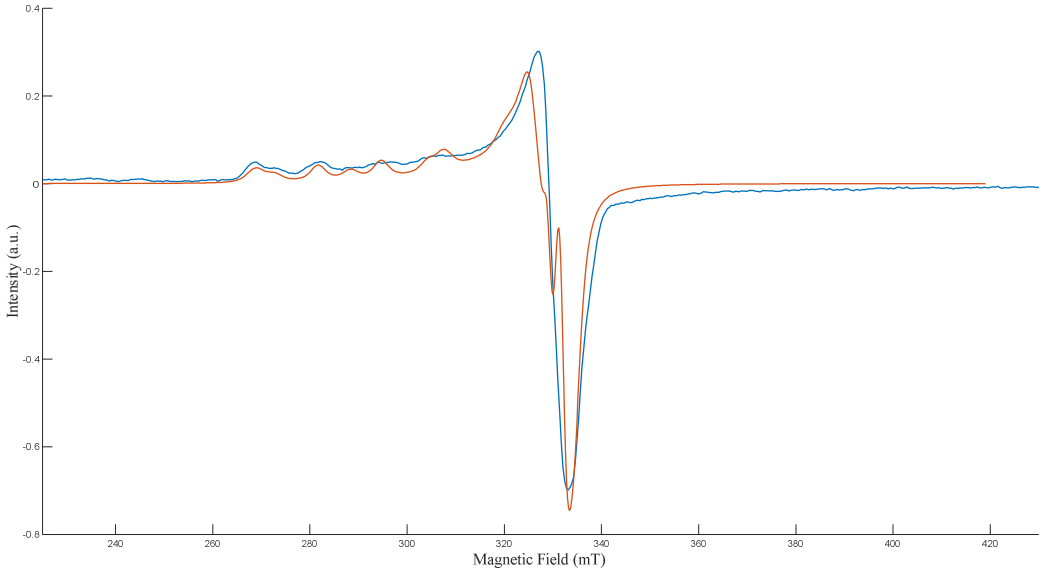

Figure 4.76: LMG5 sample: simulated spectrum (red line) and experimental spectrum (blue line).

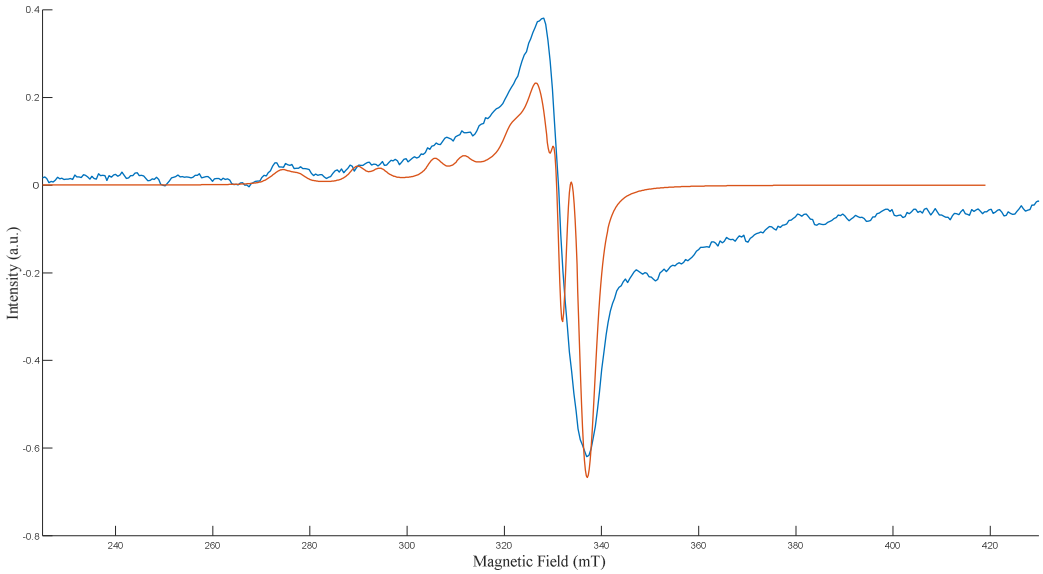

Figure **4.77**: LMC5 sample: simulated spectrum (red line) and experimental spectrum (blue line).

In **Table 4.10** are listed the simulation parameters.

Sample	LMG5		LMC5		LMEY5			LMY5		
Species	1	2	1	2	1	2	3	1	2	3
g_x	2.07	2.07	2.06	2.07	2.07	2.07	2.07	2.07	2.07	2.07
g_y	2.07	2.07	2.06	2.07	2.07	2.07	2.07	2.07	2.07	2.07
g_z	2.37	2.30	2.25	2.29	2.30	2.27	2,25	2.30	2.27	2,25
A_x (MHz)	50	50	50	58	50	58	50	50	58	50
A_y (MHz)	50	50	50	34	50	34	50	50	34	50
A_z (MHz)	420	500	530	500	480	500	550	480	500	550
$gStrain_{x,y}$	0.005	0.005	0.01	0.005	0.005	0.005	0.005	0.005	0.005	0.005
$gStrain_z$	0.01	0.01	0.01	0.01	0.01	0.01	0.01	0.01	0.01	0.01
$Astrain_{x,y}$ (MHz)	0.5	0.5	0.5	0.5	0.5	0.5	0.5	0.5	0.5	0.5
$Astrain_z$ (MHz)	1.0	1.0	1.0	1.0	1.0	1.0	1.0	1.0	1.0	1.0
Weight	66%	33%	60%	40%	37%	26%	37%	37%	26%	37%

Table 3.10: Simulation parameters for all samples: LMG5, LMC5, LMY5 and LMEY5 at room temperature. The row "weight" indicates the percentage of a species in the simulated spectrum.

The EPR spectra of SLMC5 and SLMO5 (synthetic malachite pigment) were acquired at room temperature and simulated (**Figure 4.78**).

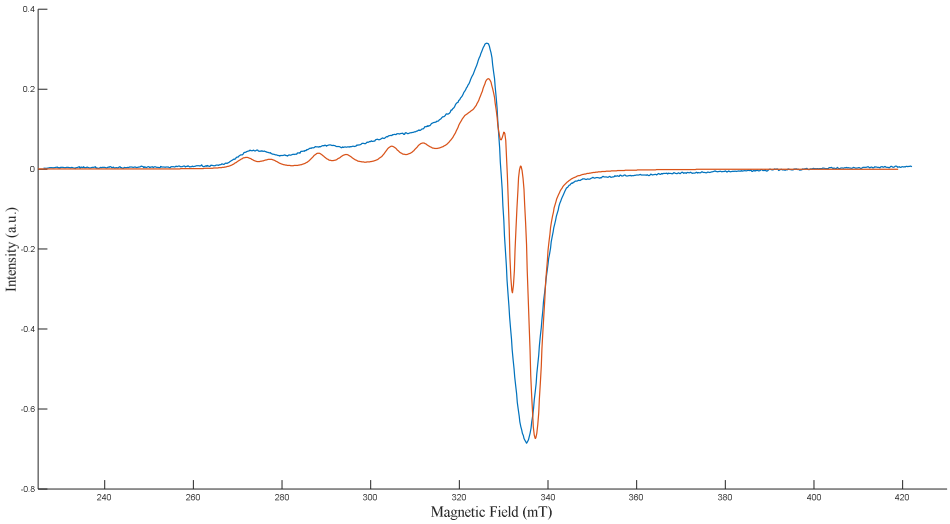

Figure 4.78: SLMC5 sample: simulated spectrum (red line) and experimental spectrum (blue line).

The simulation parameters are equal to those reported in **Table 4.10** for the LMC sample. The SLMO5 spectrum was not simulated because copper monomer features were completely covered by the pseudo-octahedral Fe (III) signal. Many parameters are slightly different from those reported in **Table 4.3** and **Table 4.7** for verdigris and copper acetate samples. This suggests that many complexes are formed with the same binder, even starting from different pigments. However, there are also copper complexes obtained with malachite and not observed with verdigris. This suggests that different pigments have some peculiarities, maybe related to the different chemical structure of the raw pigments (e.g., one or more copper ligands could be carbonate ions, present in malachite and not in verdigris). In addition, malachite and verdigris can induce a different pH in the binder matrix.

Simulation parameters for the different species were plotted in the Peisach-Blumberg diagram (see **Figure 4.79**).

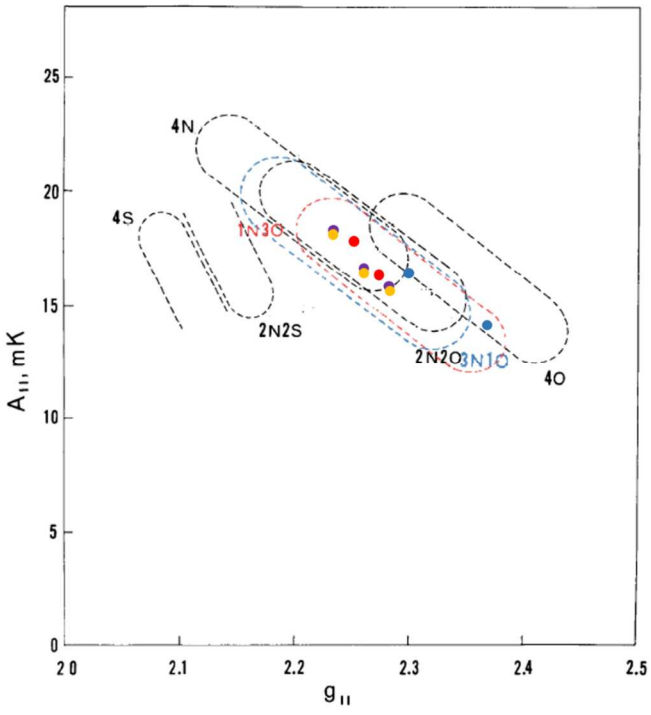

Figure 4.79: Peisach-Blumberg diagram: LMC5 (red dots), LMG5 (blue dots), LMEY5 (purple dots) and LMY5 (orange dots).

Essentially, binders induce the same type of complexation observed for verdigris and copper resinate pigments. The arabic gum complexes show, as expected, a 4O coordination, while protein-based ligands induce a coordination to the copper with a variable number of nitrogen atoms. As noticed previously, the yolk induces copper complexes with more nitrogen atoms than other binders do.

The CW-EPR spectra of these samples were acquired at different temperature (250 K, 210 K, 180 K and 150 K). The figures below show spectra sorted by pigment (from **Figure 4.80** to **Figure 4.85**).

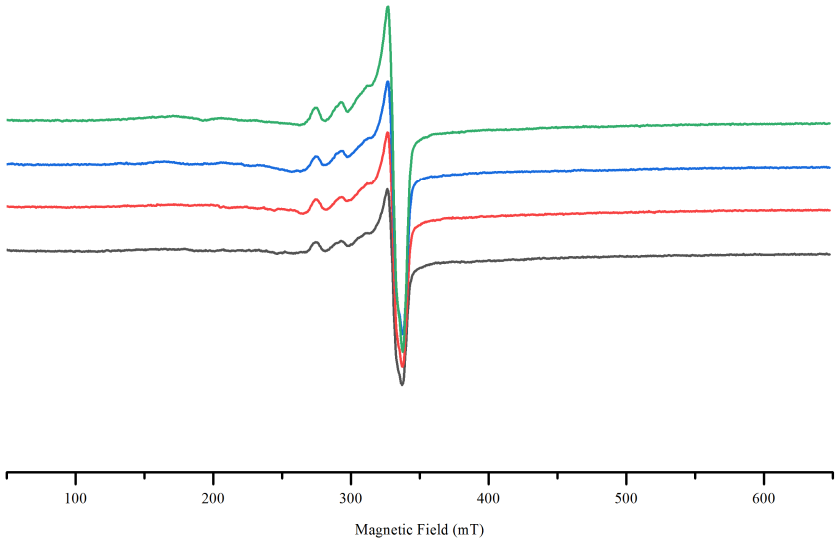

Figure 4.80: LMY5 sample: 150 K (green line), 180 K (blue line), 210 K (red line), and 250 K (black line).

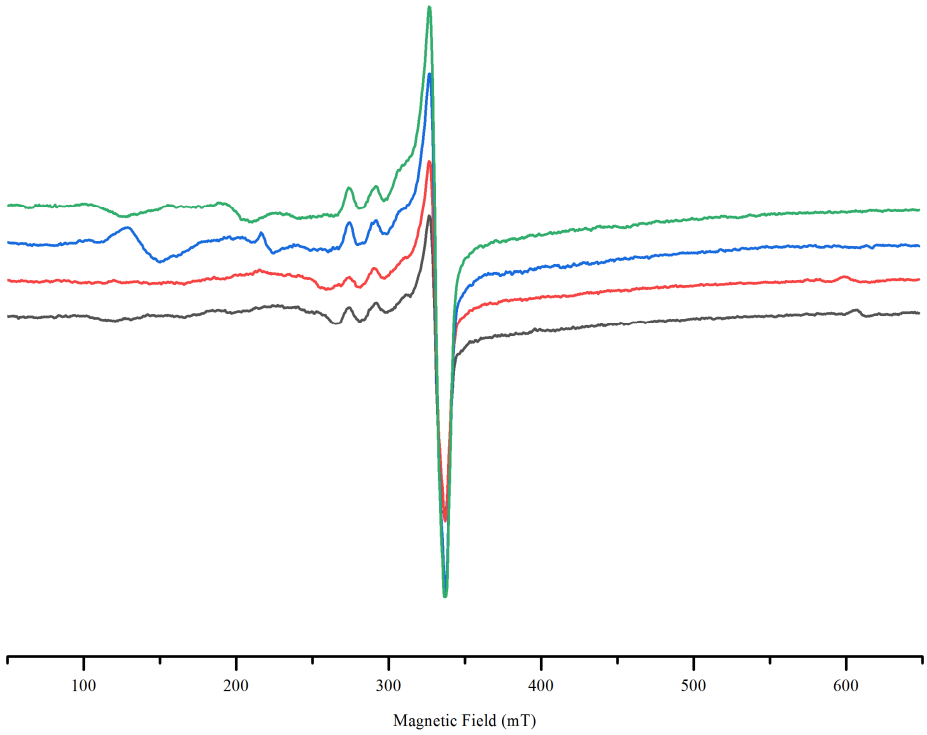

Figure 4.81: LMEY5 sample: 150 K (green line), 180 K (blue line), 210 K (red line), and 250 K (black line).

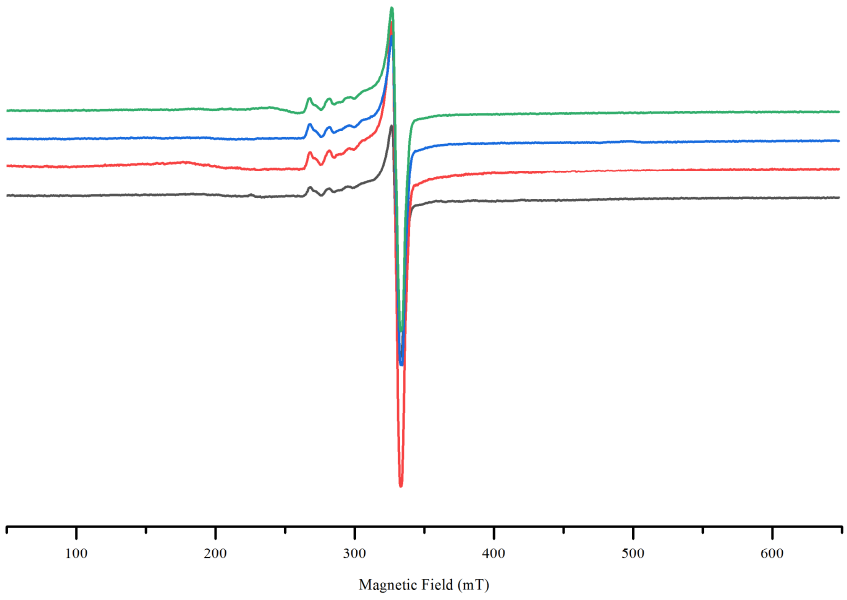

Figure 4.82: LMG5 sample: 150 K (green line), 180 K (blue line), 210 K (red line), and 250 K (black line).

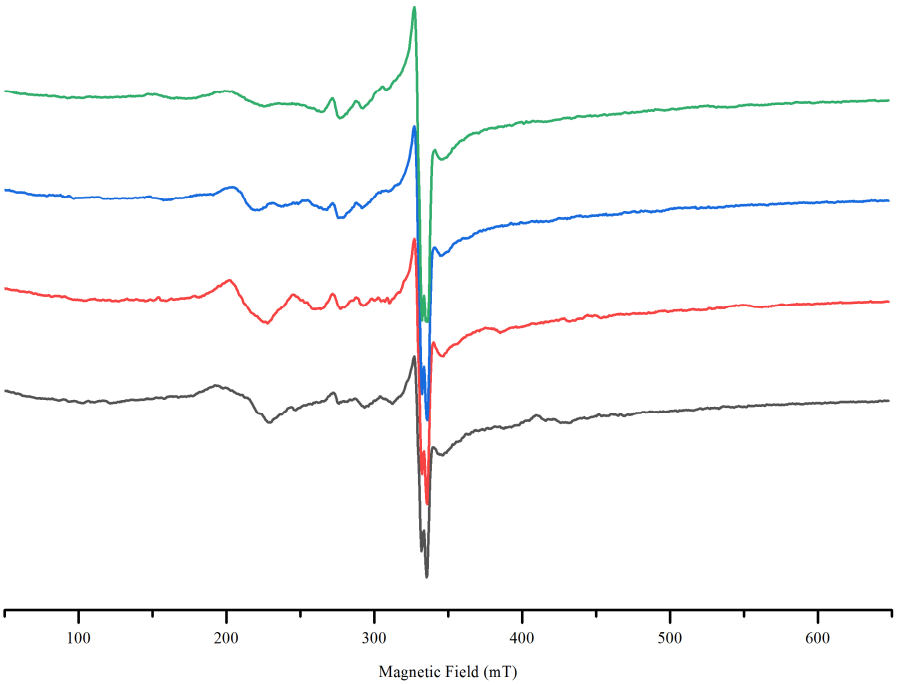

Figure 4.83: LMO5 sample: 150 K (green line), 180 K (blue line), 210 K (red line), and 250 K (black line).

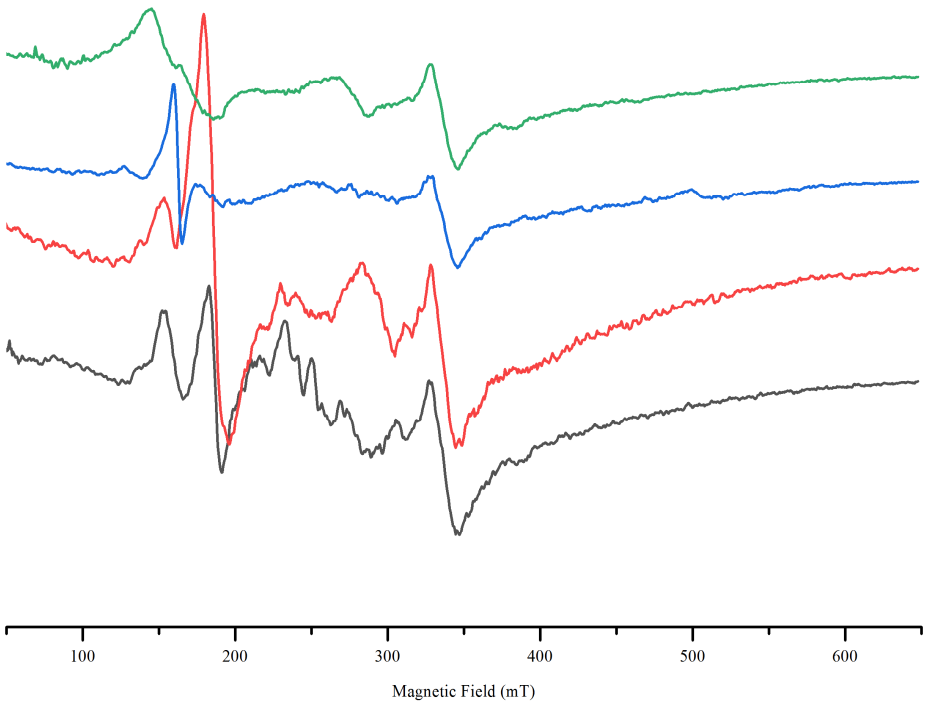

Figure 4.84: LMEW5 sample: 150 K (green line), 180 K (blue line), 210 K (red line), and 250K (black line).

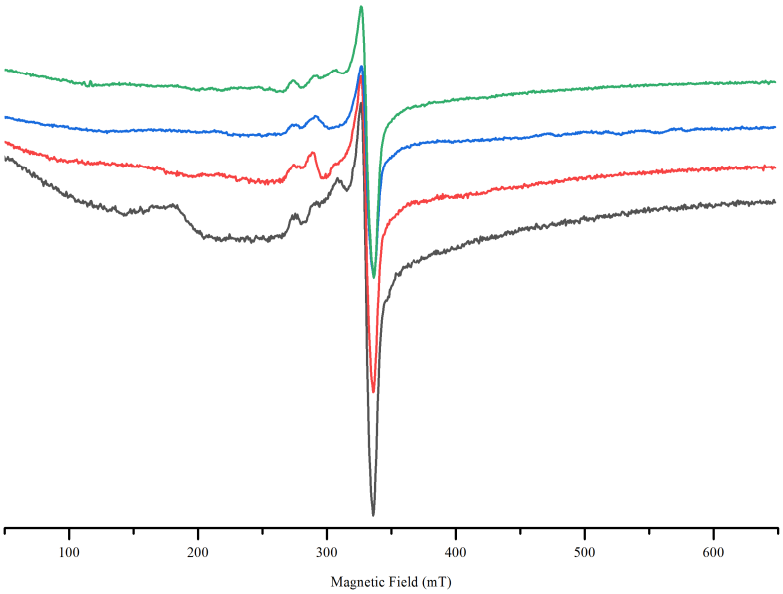

Figure 4.85: LMC5 sample: 150 K (green line), 180 K (blue line), 210 K (red line), and 250 K (black line).

Only the spectra at 150 K of LMC5, LMG5, LMEY5 and LMY5 were simulated to see whether some difference emerged from the simulation values obtained at room temperature (see from **Figure 4.86** to **Figure 4.89**). Simulation parameters are collected in **Table 4.11** and simulation figures are displayed below.

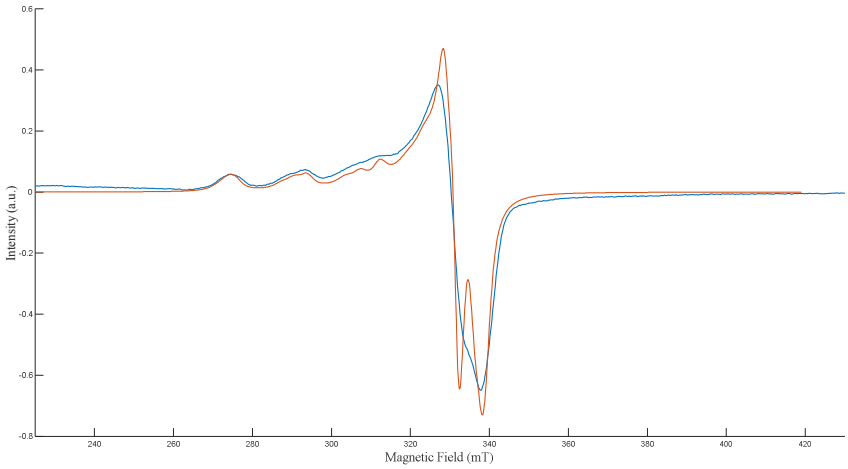

Figure 4.86: LMY5 sample 150 K: simulated spectrum (red line) and experimental spectrum (blue line).

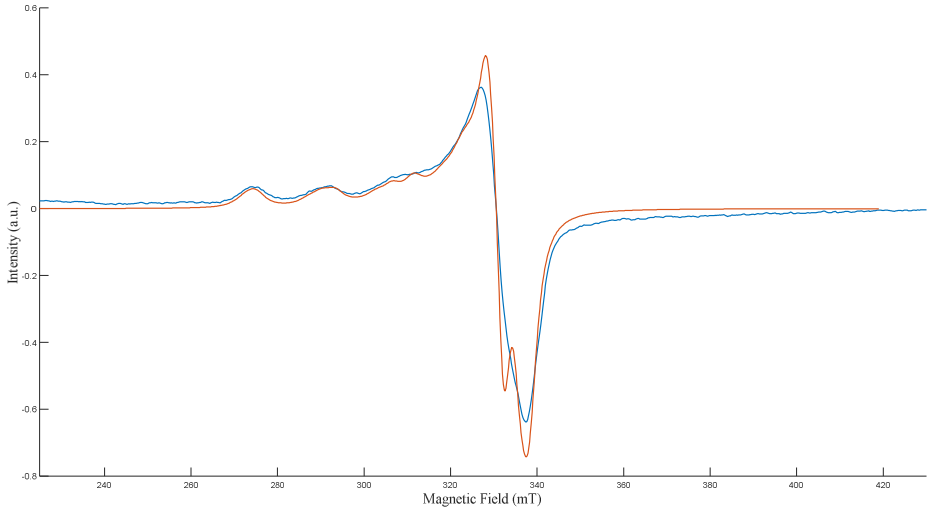

Figure 4.87: LMEY5 sample 150 K: simulated spectrum (red line) and experimental spectrum (blue line).

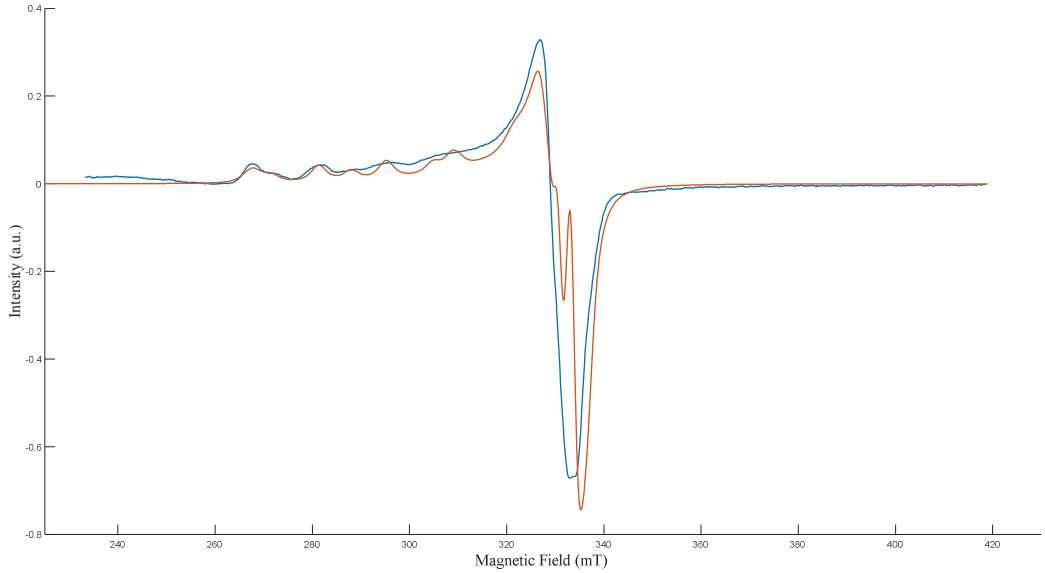

Figure 4.88: LMG5 sample 150 K: simulated spectrum (red line) and experimental spectrum (blue line).

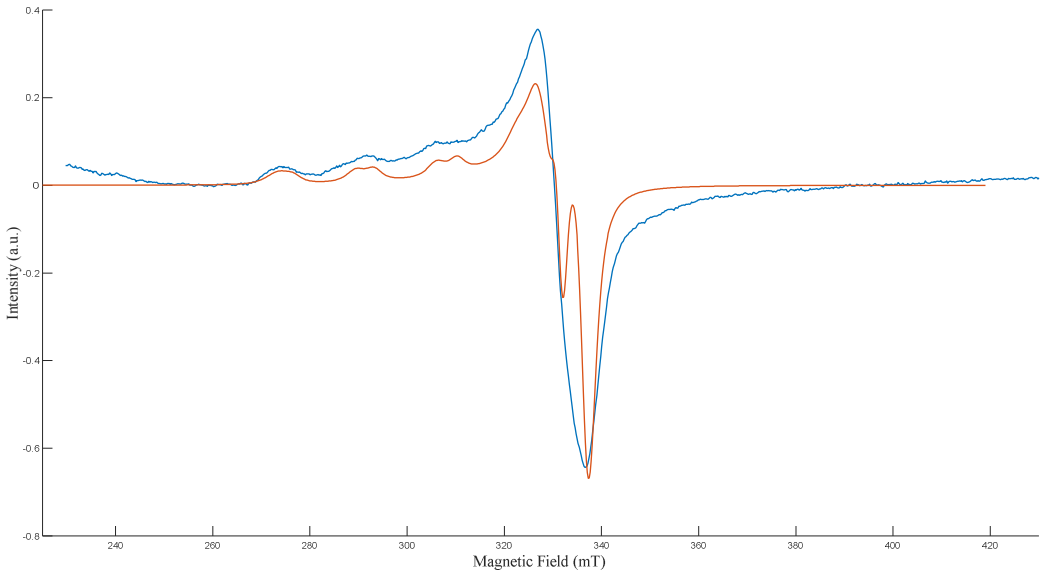

Figure 4.89: LMC5 sample 150 K: simulated spectrum (red line) and experimental spectrum (blue line).

Sample	**LMG5**		**LMC5**		**LMEY5**			**LMY5**		
Species	1	2	1	2	1	2	3	1	2	3
g_x	2.07	2.07	2.06	2.07	2.07	2.07	2.07	2.07	2.07	2.07
g_y	2.07	2.07	2.06	2.07	2.07	2.07	2.07	2.07	2.07	2.07
g_z	2.37	2.30	2.25	2.29	2.31	2.27	2,25	2.30	2.27	2,25
A_x (MHz)	50	50	50	58	50	58	50	50	58	50
A_y (MHz)	50	50	50	34	50	34	50	50	34	50
A_z (MHz)	450	530	540	520	490	520	560	490	520	570
$gStrain_{x,y}$	0.005	0.005	0.01	0.005	0.005	0.005	0.005	0.005	0.005	0.005
$gStrain_z$	0.01	0.01	0.01	0.01	0.01	0.01	0.01	0.01	0.01	0.01
$Astrain_{x,y}$ (MHz)	0.5	0.5	0.5	0.5	0.5	0.5	0.5	0.5	0.5	0.5
$Astrain_z$ (MHz)	1.0	1.0	1.0	1.0	1.0	1.0	1.0	1.0	1.0	1.0
Weight	66%	33%	60%	40%	37%	26%	37%	37%	26%	37%

Table 4.11: Simulation parameters for all samples: LMG5, LMC5, LMY5 and LMEY5 at 150K. The row "weight" indicates the percentage of a species in the simulated spectrum.

Small differences are observed in the hyperfine parameters between room and low temperature, related to a different dynamic averaging of the magnetic parameters. In any case, the differences between simulation parameters at room temperature and at 150 K are very small suggesting that the complexes are quite stable with temperature.

The DI (Double Integral) was calculated only for those samples that clearly showed the copper monomer feature and were less affected by Fe(III) signal. DI was plotted against temperature (see **Figure 4.90**).

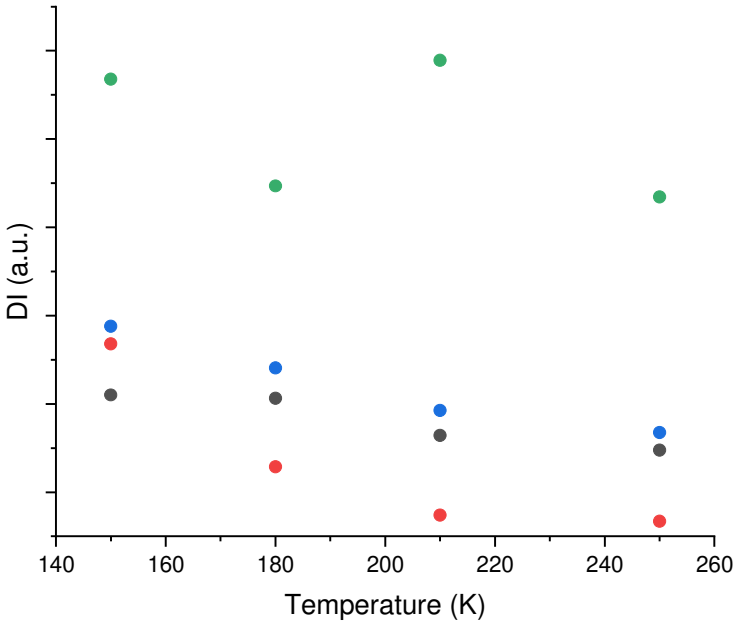

Figure 3.90: DI of the copper-complex signal (330 mT) vs. temperature: LMG5 (black dots), LMC5 (red dots), LMY5 (blue dots) and LMEY5 (green dots).

According to DI values, the trend for a paramagnetic species is respected for all the combinations pigment-binder, even if the trends have a great variability: this is probably due to an unavoidable contribution from the iron signal, which was not easy to subtract in the calculation of the double integral.

The ATR-IR spectra for the 5% samples were acquired (see Figure 3.30 for the ATR-IR spectra of binders and **Figure 4.91**).

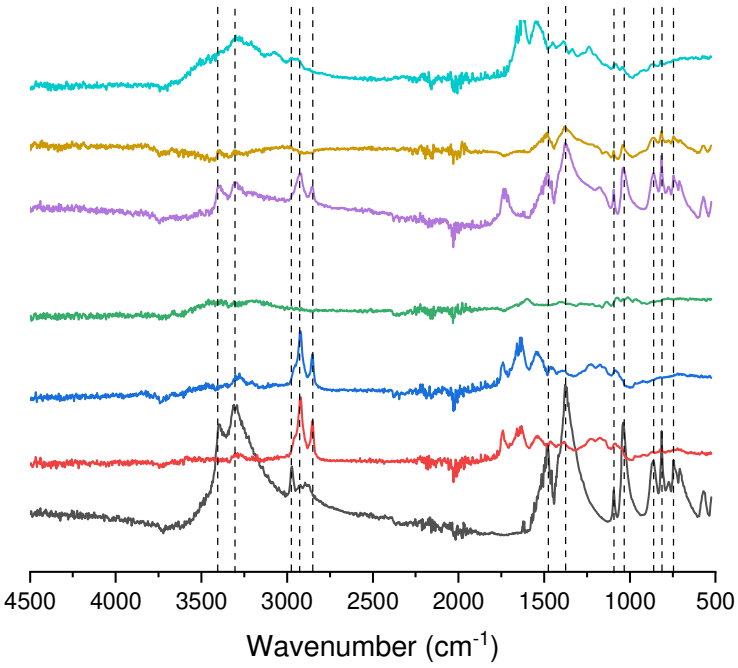

Figure 4.91: ATR-IR spectra: LM (black line), LMY5 (red line), LMEY5 (blue line), LMG5 (pink line), LMO5 (green line), LMEW5 (dark blue line), and LMC5 (turquoise line).

The signals of binders are evident in all the pigment-binder combinations. In some spectra (e.g., LMO5 and LMEW5), the signals of raw malachite are still evident, suggesting a weak complexation strength of the binder. In the pigment-binder combinations, small features are often observed below 1600 cm^{-1}, which are different from either the pigment or the binder alone: these features are likely related to the copper-binder complexes.

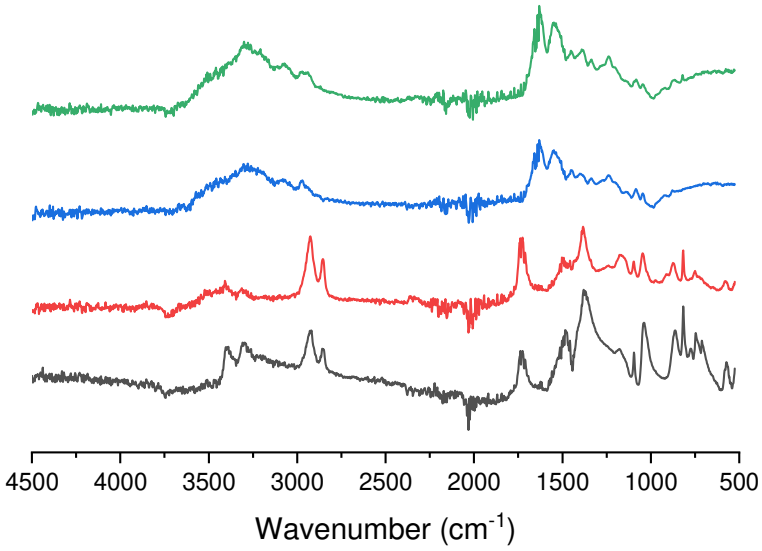

Figure 4.92: ART-IR spectra: LMO5 (black line), SLMO5 (red line), SLMC5 (blue line) and LMC5 (green line).

The ATR-IR spectra for the SLMO5 and the SLMC5 sample were acquired. As shown in **Figure 4.92**, natural and synthetic samples show the same spectral features. Just minor differences, related to slightly different pigment/binder ratios, are observed between LMO5 and SLMO5.

4.4 Azurite

4.4.1 Raw pigment (AZ and SAZ samples)

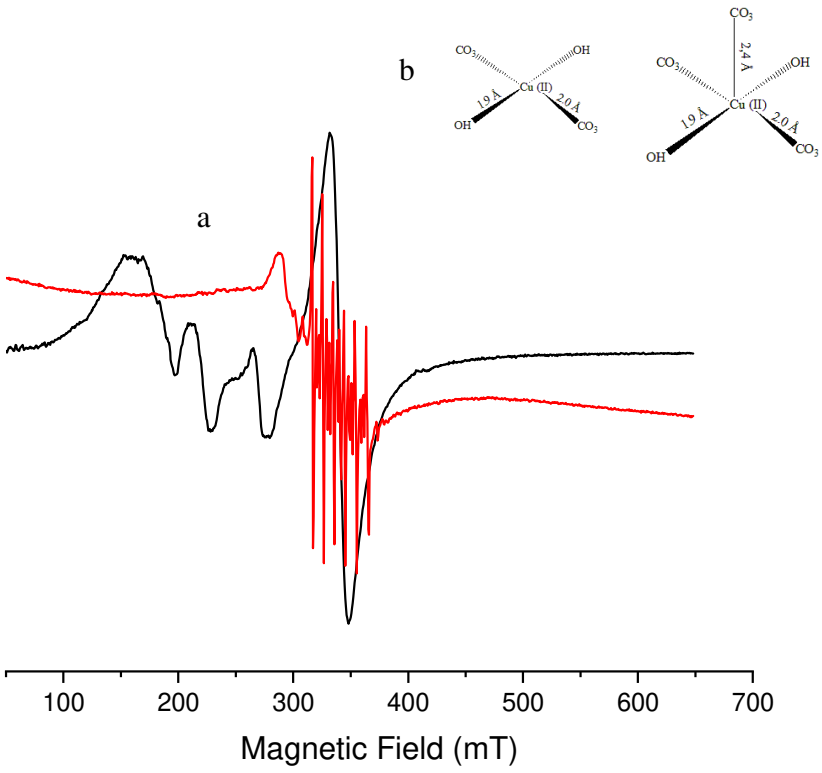

Figure 4.93: a) CW-EPR spectrum (X-band) of LM (black line) and SLM (red line), b) structure of the copper centers in azurite.

The EPR spectrum of natural azurite (**Figure 4.93a** black line) shows the same features seen for the malachite sample (LM): both have a carbonate nature and similar chemical structure. Moreover, like in LM, many signals are observed below 300 mT, attributable to superparamagnetic species, suggesting the presence of iron and copper oxides. The rhombic Fe(III) signal is not present, or it is covered by oxide signals. On the other hand, some particular features characterize the SAZ spectrum (**Figure 4.93a** red line): in addition to the pseudo-octahedral Fe(III) signal, Mn(II) signal features are evident. This observations are partially verified by XRF experiments (**Figure 4.94** and **Figure 4.95**).

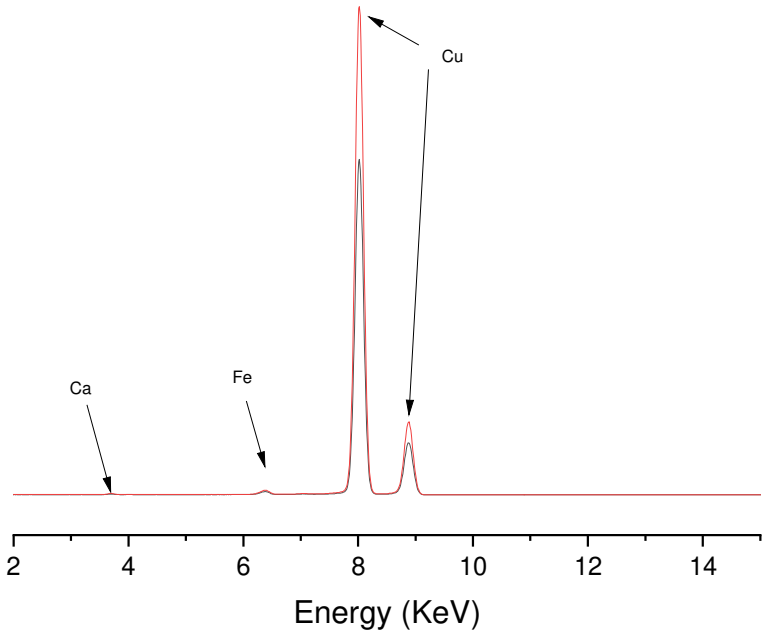

Figure 4.94: XRF spectrum of AZ sample.

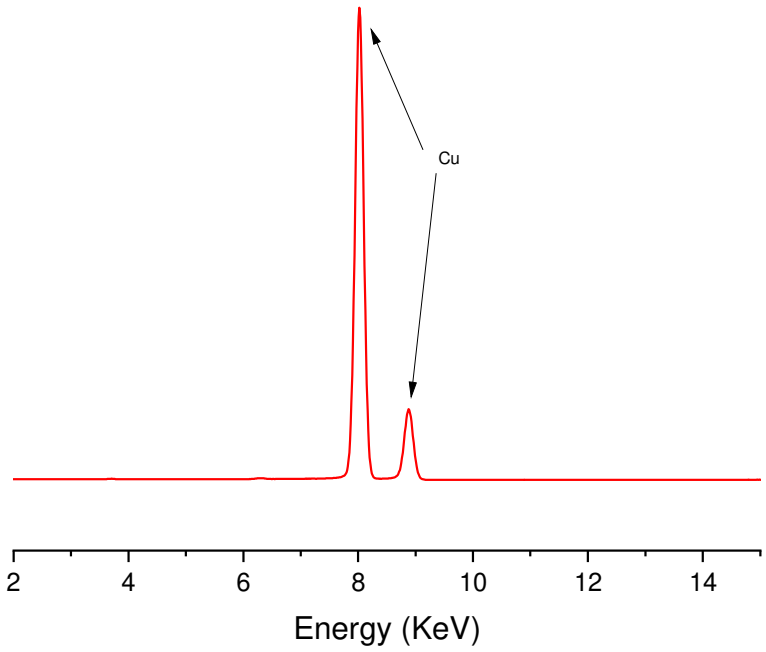

Figure 4.95: XRF spectrum of SAZ sample.

The iron presence is verified for AZ sample, while the manganese signals do not appear. However, the EPR technique is much more sensitive to Mn(II) species than the sensitivity of XRF to manganese. The SAZ sample does not show any iron XRF signal.

The EPR spectra for the AZ sample were acquired also at different temperature (250 K, 210 K, 180 K, and 150 K) and are displayed in **Figure 4.96**.

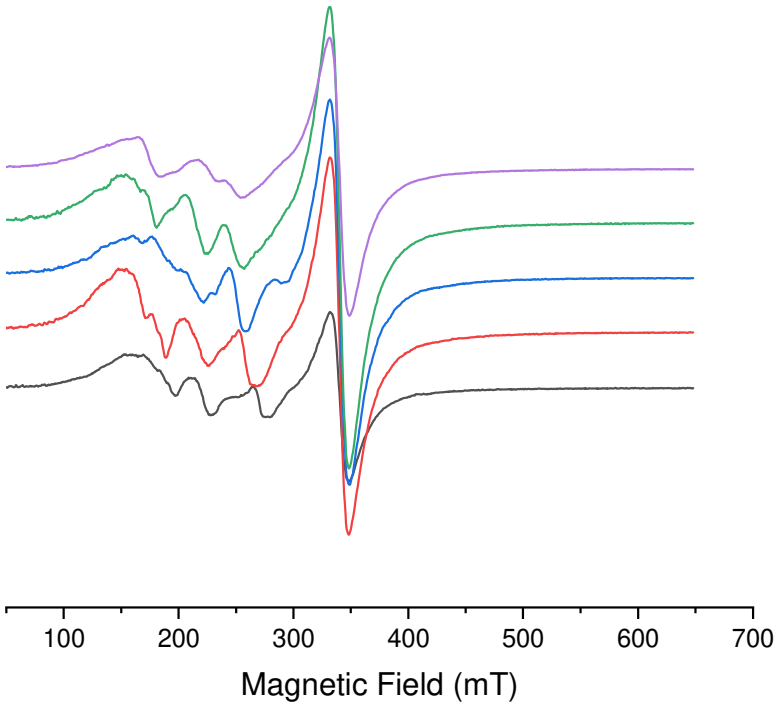

Figure 4.96: AZ sample: 300 K (black line), 250 K (red line), 210 K (blue line), 180 K (green line) and 150 K (purple line).

The superparamagnetic signals below 300 mT do not change very much: this suggests that likely the superparamagnetic species are mainly copper oxides, because the signals due to superparamagnetic particles of iron oxides broaden very much and shift to low fields.

As expected, the paramagnetic signal due to pseudo-octahedral Fe(III) does not shift..

The ATR-IR spectra for AZ and SAZ samples are shown in **Figure 4.97**.

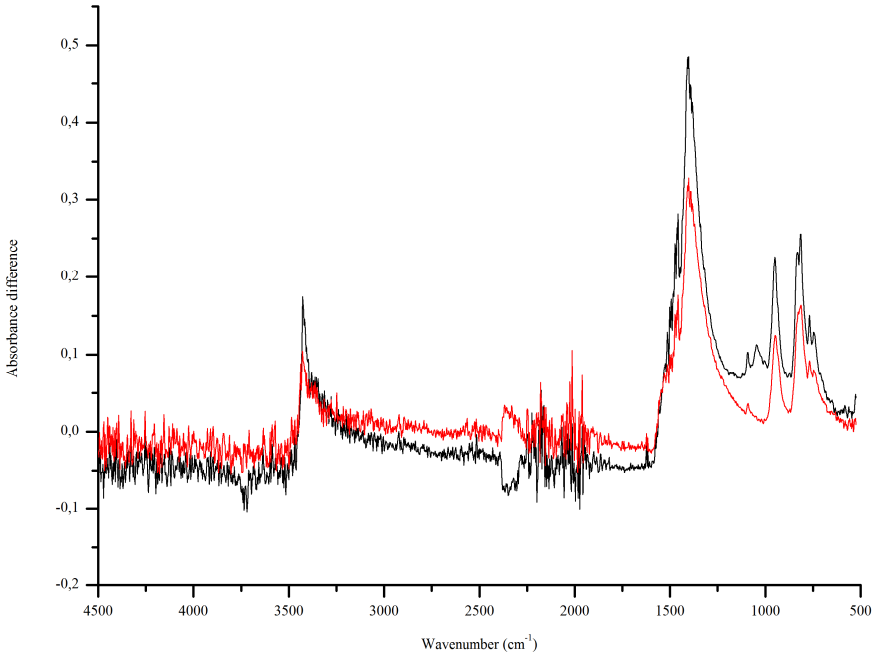

Figure 4.97: ATR-IR: AZ spectrum (black line) and SAZ spectrum (red line).

The two spectra show the same features. The assignment for the vibrational modes is the same reported for malachite (**Table 4.9**), due to the common carbonate structure. The azurite signals are slightly shifted at lower wavenumbers.

4.3.2 Azurite mixtures

The EPR spectra of pigment/binder combinations with a 1:3 ratio, acquired at room temperature, are shown in **Figure 4.98.**

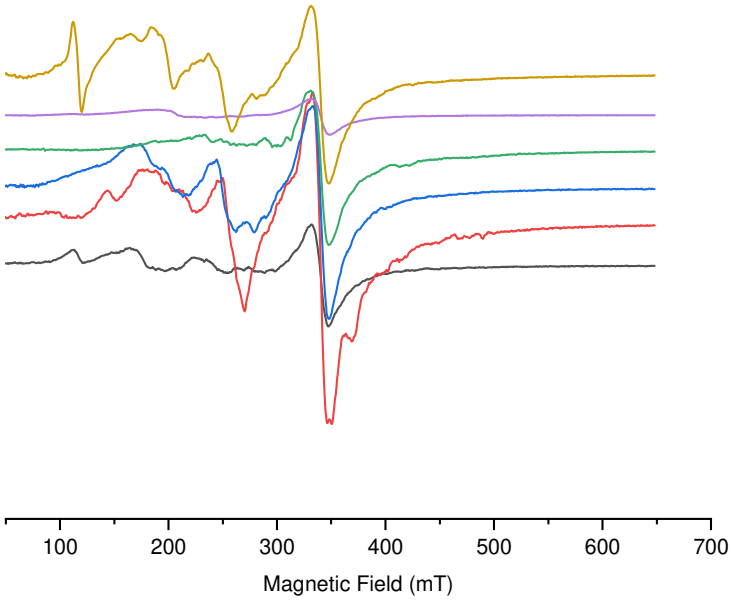

Figure 4.98: CW-EPR (X-band) spectra at room temperature: AZY (yellow line), AZEY (purple line), AZO (green line), AZG (blue line), AZEW (red line) and AZC (black line).

The spectra are dominated by pseudo-octahedral Fe(III) signal. Therefore, the features due to copper monomers are hard to visualize. The CW-EPR spectra at room temperatures of the samples with 5% pigment/binder ratio are shown in **Figure 4.99**.

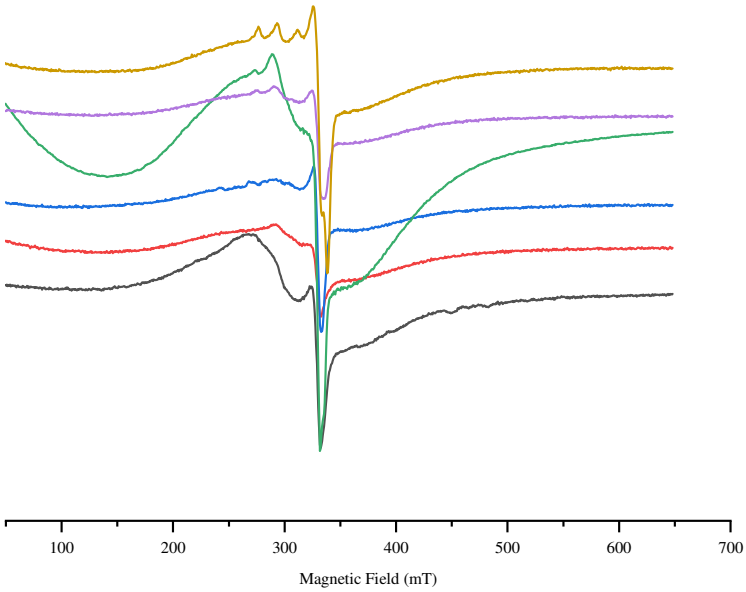

Figure 4.99: CW-EPR (X-band) spectra at room temperature: AZY5 (yellow line), AZEY5 (purple line), AZO5 (green line), AZG5 (blue line), AZEW5 (red line) and AZC5 (black line).

The spectra are still affected by the iron signal, even if the amount of binder is larger. Only in a few cases, the typical features of monomeric copper complexes stand out in the spectra (e.g., AZY5). Due to the iron signal disturbance, it was not possible to simulate reliably the spectra of the monomeric copper species.

EPR spectra for the samples with 5% pigment/binder ratio were acquired at different temperatures (250K, 210K, 180K and 150K). The spectra are displayed below (see from **Figure 4.100** to **Figure 4.105**)

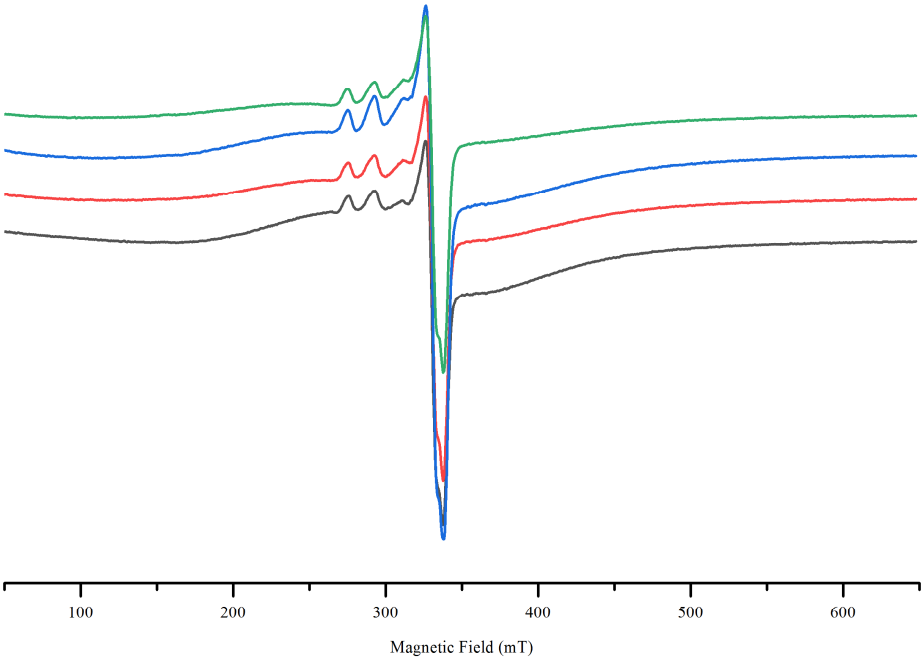

Figure 4.100: AZY5 sample: 150K (green line), 180K (blue line), 210K (red line) and 250K (black line).

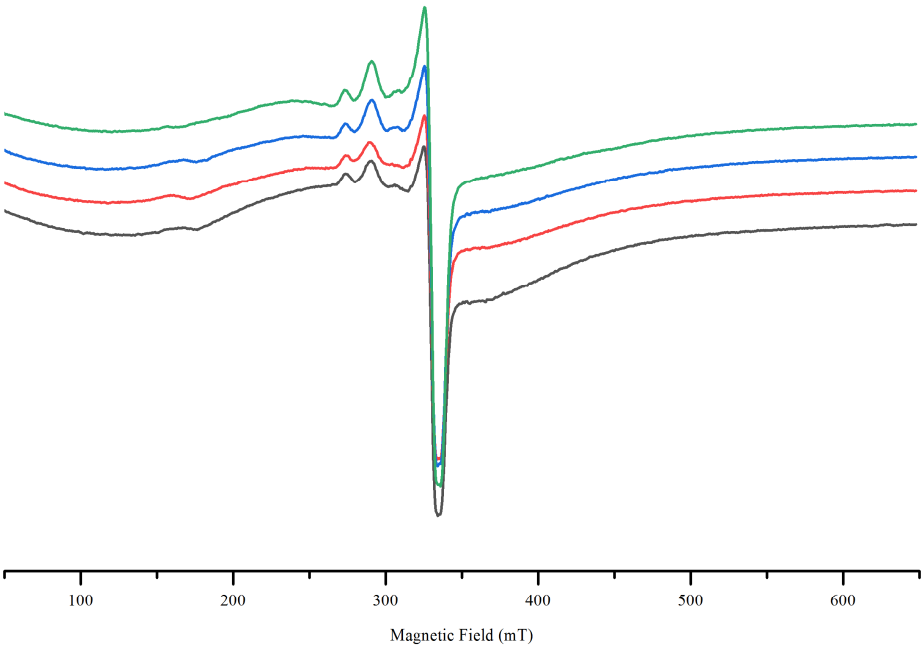

Figure 4.101: AZEY5 sample: 150K (green line), 180K (blue line), 210K (red line) and 250K (black line).

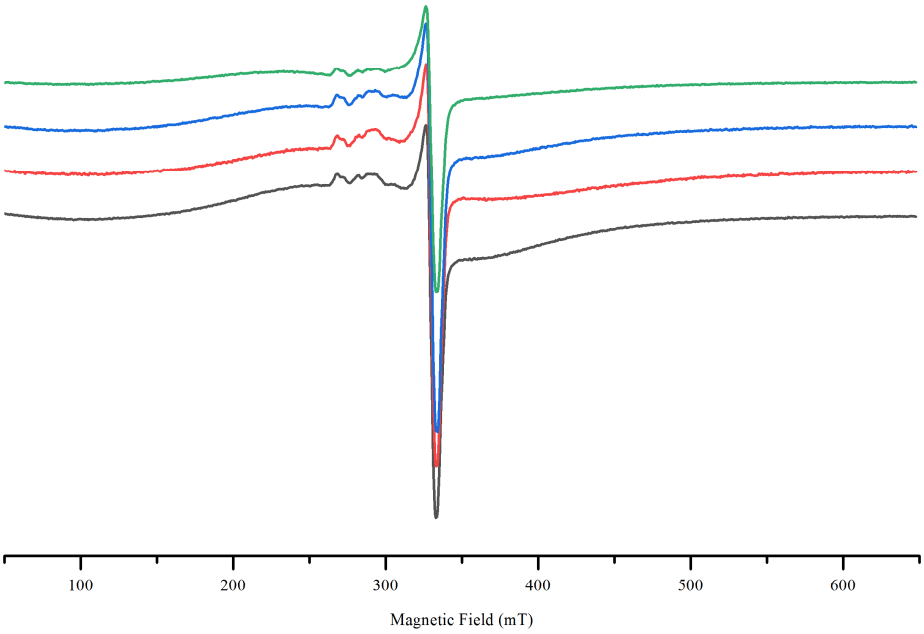

Figure 4.102: AZG5 sample: 150K (green line), 180K (blue line), 210K (red line) and 250K (black line).

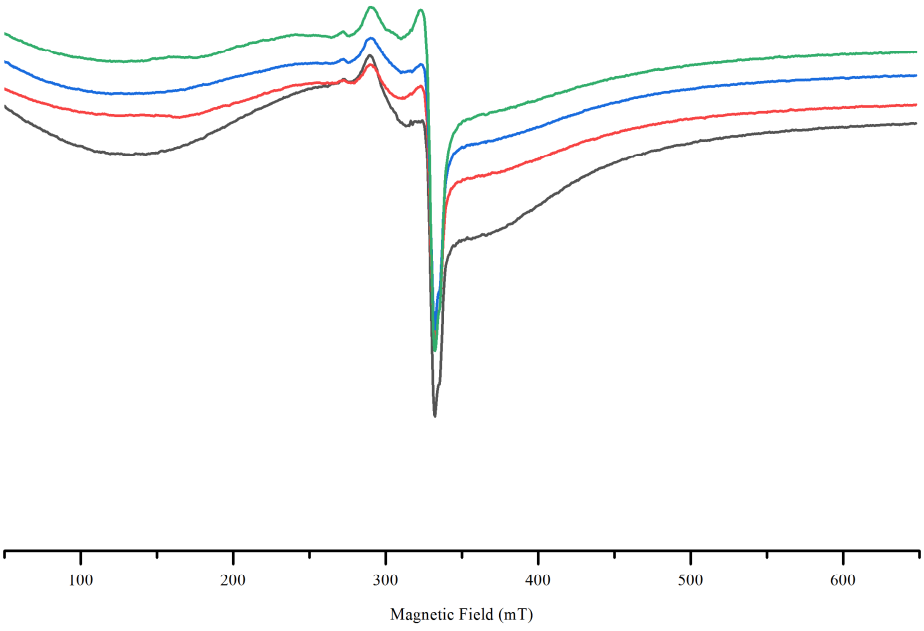

Figure 4.103: AZO5 sample: 150K (green line), 180K (blue line), 210K (red line) and 250K (black line).

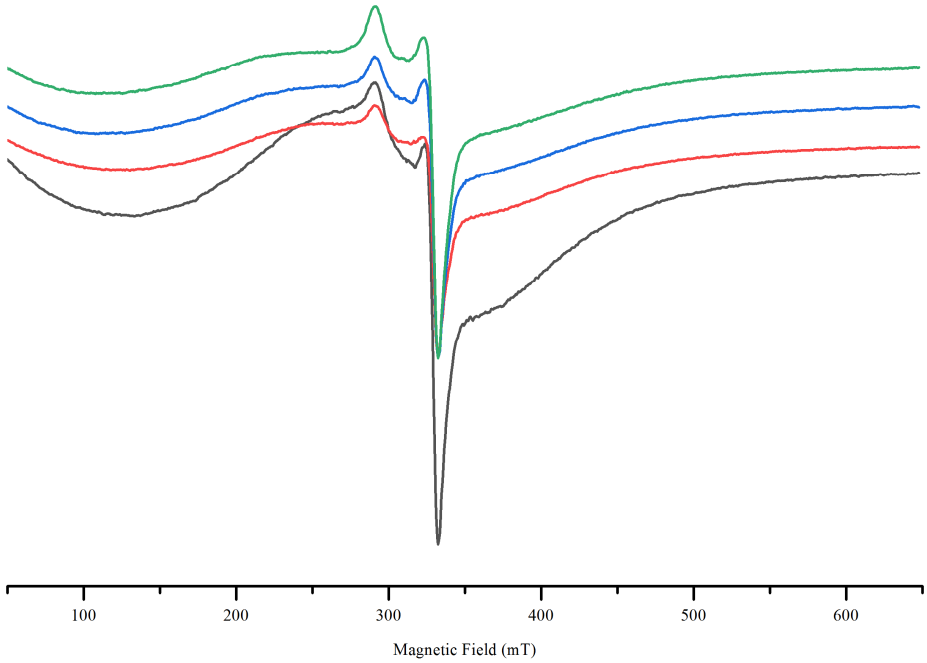

Figure 4.104: AZEW5 sample: 150K (green line), 180K (blue line), 210K (red line) and 250K (black line).

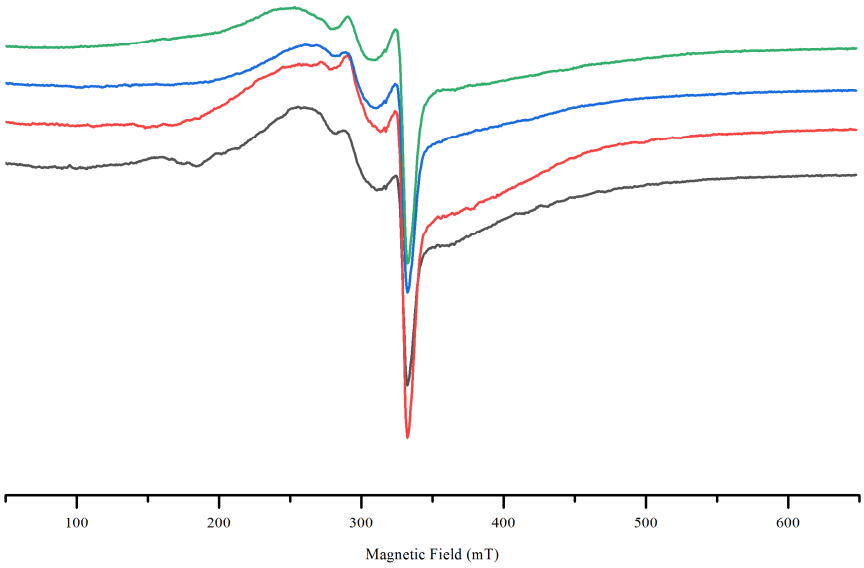

Figure 4.105: AZC5 sample: 150K (green line), 180K (blue line), 210K (red line) and 250K (black line).

Even if cooling down the system some features of monomeric copper species stand out in the spectra, it was impossible to simulate them, because signals were still very affected by the Fe(III) signal, covering the copper signals.

The ATR-IR spectra of the these latter samples were acquired, and are shown in **Figure 4.106**. In some spectra, the raw pigment signals are still present suggesting that the binder is not so effective to form copper complexes. The binders signals are evident (for comparison, see **Figure 4.31**). The main differences are noticeable in the spectral region below 1600 cm^{-1}. As previously done for the malachite pigment, the ATR-IR spectra of SAZO5 was acquired and compared to AZO5 (see **Figure 4.107**). The two spectra are basically equal.

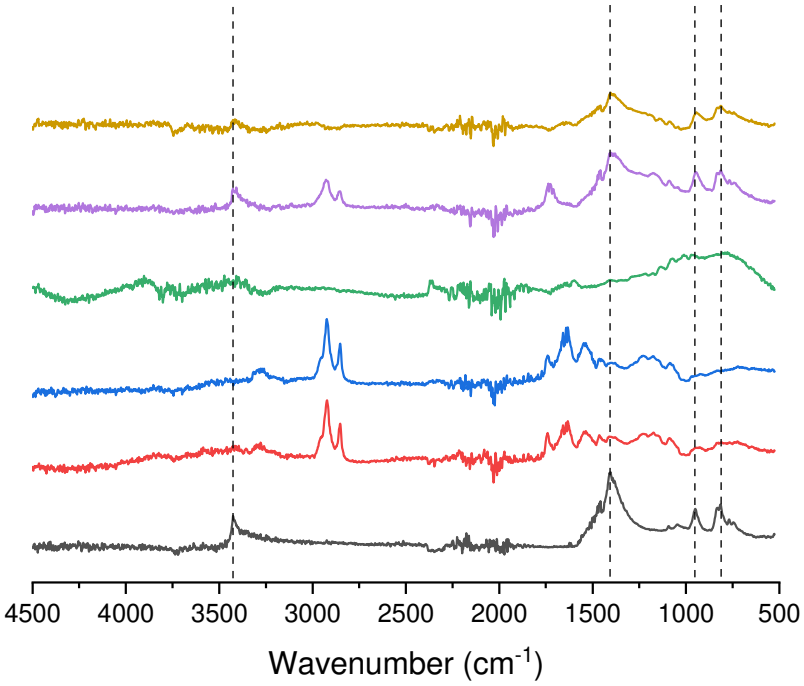

Figure 4.106: ATR-IR spectra: AZ (black line), AZY5 (red line), AZEY5 (blue line), AZG5 (pink line), AZO5 (green line) and AZEW5 (dark blue line).

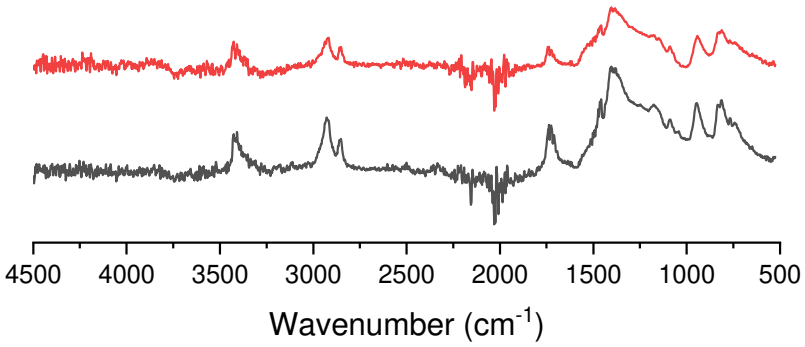

Figure 4.107: ART-IR spectra: AZO5 (black line), SAZO5 (red line).

Chapter 5: Discussion

Copper-based pigments are known to be “dangerous” pigment for organic material supports (paper, parchment, wood), because of their ability in inducing degradation paths, mainly represented by oxidation and hydrolysis reactions. However, the mechanism through which copper-pigments brings about degradation is not perfectly clear. The CW-EPR technique was applied in this work, because EPR is likely the only technique able to identify and characterize with high sensitivity Cu(II) species. Verdigris pigment is particularly interesting, because it is known as the most efficient pigment in inducing degradation. Therefore, a wide EPR characterization has been carried out on this pigment and its combinations with the binders. EPR signals of pure verdigris are easily recognized, due to the typical triplet (S=1) spectrum related to the dimeric structure of the copper acetate: a bimetallic carboxylate complex with a bidentate bridging coordination. The Hamiltonian quantities (factor g, hyperfine constant A, zero field parameters E and D), that describe the spin system, were estimated through spectral simulation: the obtained parameters were equal to those reported by Binet [16].

The two unpaired electrons (Cu^{2+}: [Ar] $3d^9$) localized on the copper centers are magnetically coupled. The type of interaction can be ferromagnetic (i.e., the stable state is ferromagnetic) or antiferromagnetic (i.e., the stable state is antiferromagnetic). It is possible to determine the nature of the coupling by evaluating the Double Integral under the EPR spectrum (DI) as a function of the temperature. The DI is an estimation of the magnetic susceptibility χ that depends on the type of magnetism (paramagnetism, ferromagnetism, antiferromagnetism): paramagnetic, antiferromagnetic, and ferromagnetic systems respond differently to temperature

changes. It was noticed that the raw pigment has an antiferromagnetic behavior below 210 K, and a ferromagnetic behavior above 210 K, indicating a ferromagnetic-antiferromagnetic transition around 210K.

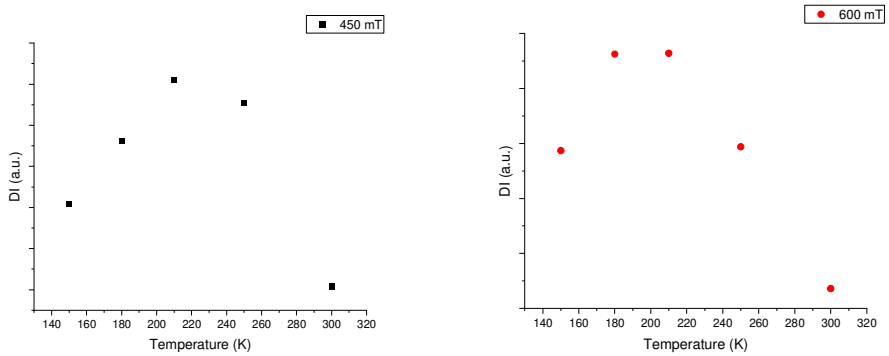

Figure 5.1: DI vs Temperature for 450 mT signals (black dots) and 600 mT (red dots).

The verdigris was also characterized by XRF and ATR-IR experiments. In the limit of XRF sensitivity, the absence of other metals in the raw pigment that could be EPR-active was verified, while the ATR-IR spectra highlighted the main vibrational modes..

The CW-EPR spectra of the verdigris sample with a pigment/binder ratio 1:3, which was the common ratio used for a typical color paste, highlighted a very surprising aspect of pictorial mixtures: the presence of monomeric Cu(II) complexes. This data is very relevant, and almost unknown in literature, since the pictorial layer is considered a suspension of small pigment grains in the binder, whose function is to act as a glue. The EPR investigation suggests that the pigment is at least partially dissolved in the matrix of the binder. This leads to the formation of copper monomer complexes. Moreover, EPR indicates that different binders have different capability of dissolving the verdigris pigment, giving rise to different complexes between the Cu(II) ions and the binder molecules.

In order to explore the binder action, another series of samples was prepared with a 5% pigment/binder ratio, so to increase the amount of copper monomers and to better characterize the complexes. Actually, the signal of monomeric copper species increased, while the signal of the dimeric copper species, confirming that the monomeric copper complexes were due to the binder molecules. The main spectral parameters were obtained by simulation with a program written with the EasySpin software. The EPR spectra of the complexes were characterized by different parameters, depending on the binder used in the mixtures, and usually more copper species were present for a type of binder. The parameters of the various species, in particular $A_{//}$ and $g_{//,}$ were plotted in the Peisach-Blumberg diagrams, allowing the evaluation of the number and the nature of donor atoms involved in the complexes. It was observed that fatty acid- and carbohydrates-based binders induced a four-oxygen (4O) complexation, as expected. On the other hand, protein-based binders induced a nitrogen-based complexation. Unfortunately, in the protein-based binder cases it was very difficult to understand how many nitrogen and oxygen are actually involved in the complexes, because of the overlap of the assignment regions.

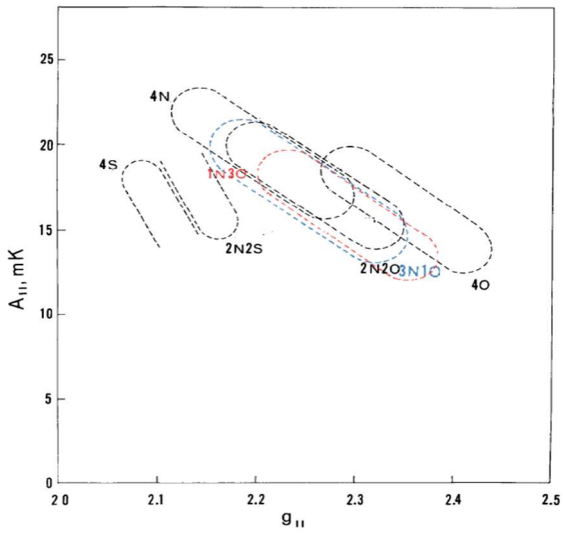

Figure 5.2: Peisach-Blumberg diagram.

In some spectra with protein binders, small super hyperfine features were visible on the main lines of the Cu(II) hyperfine pattern: these features are indicative of coupling with nitrogen atoms, therefore supporting the assignment based on the Peisach-Blumberg diagrams.

The Double Integral trend with temperature was obtained both for monomer and dimer signals in the pigment/binder mixtures. As expected for isolated copper complexes, the monomer signals showed the typical trend of paramagnetic species, according to Curie law: a signal intensity growth on lowering temperature.

On the other hand, the dimer signals for the verdigris/binder combinations had a different behavior than the pure verdigris pigment, with a very small dependence on temperature. This suggests that the copper dimers are actually dissolved in the binder, and the cooperative ferromagnetism, which exists in the verdigris crystal structure, ceases down: the large dimer-dimer distances do not allow a magnetic interaction, isolating single dimers that have a mainly antiferromagnetic nature.

Only in the linseed oil, the DI plot showed a clear maximum around 210 K reproducing the trend observed for raw verdigris, suggesting the presence of small verdigris particles not dissolved.

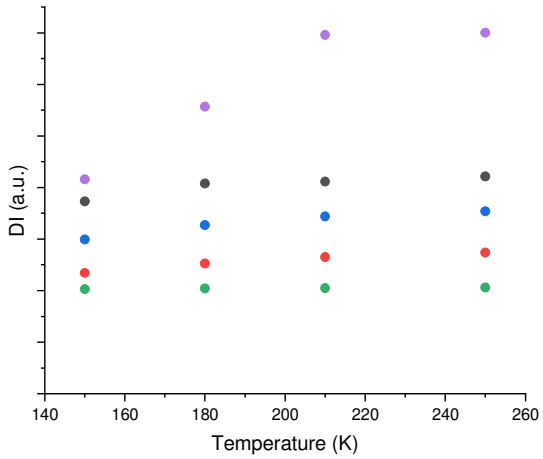

Figure 5.3: DI of dimer signal (450 mT) vs temperature: VRC5 (black dots), VREW5 (red dots), VRY5 (blue dots), VREY5 (green dots) and VRO5 (purple dots).

The spectra acquired at 150 K were also simulated, in order to evaluate possible changes in the magnetic parameters, indicative of changes in the type of copper species. Only small differences were observed, indicative that the monomeric copper complexes were the same as observed at room temperature. However, in most simulations, no more than two species were taken into account, but it was difficult to fit experimental spectra at high and low temperature with the same set of parameters: this suggests that probably, in many cases, more than two species were present. Further EPR experiments, at Q-band and with different pigment/binder ratios, will be necessary to evaluate the actual number of copper species to be simulated.

ATR-IR spectra of the 5% verdigris/binder mixtures were acquired and analyzed, in order to evaluate the changes in the binders with the formation of the copper complexes. The IR signal of verdigris (copper acetate) was absent in all the verdigris/binder combinations, except for VRO5, where a residual signal was still present. Small changes in the binder signals in the spectral region below 1600 cm^{-1} were also detected. Unfortunately, it is very difficult understand the changes of the

signals because of spectra crowdedness. Moreover, even if the assignment were possible, the changes are so small that it is impossible to understand nature and number of atoms involved in the complexes by checking changes in ligand vibration modes. The only conclusion from ATR-IR is that some complexes were likely formed in the mixtures. CW-EPR technique was much sensitive, providing clear evidence for copper complex formation, and providing information about type and nature of these complexes.

Then, it was considered a second type of pigment: the copper resinate. As discussed in the Chapter 2, the verdigris pigment and the copper resinate have the same molecular structure: a bimetallic carboxylate complex with a bidentate bridging coordination. However, the copper resinate ligands have a different functionalization. The CW-EPR technique permitted to characterize the magnetic properties of copper-resinate complexes in the pigment. The experimental spectrum showed typical dimeric signals, as observed in the VR sample, but simulations indicated different magnetic parameters, related to longer Cu-Cu distances than in verdigris. In addition to the dimer signal, a copper monomer signal was evident in the copper resinate spectrum, indicating that the resin components can coordinate single Cu(II) ions. The monomer signal was simulated, and the $A_{//}$ and $g_{//}$ values were plotted in the Peisach-Blumberg diagram: the position in the diagram clearly suggests a four-oxygen (4O) type of coordination. Since natural resins are mainly composed by diterpenoids having carboxylic groups, we can reasonably suppose that carboxylates bridge the Cu(II) ions in these complexes. Further EPR investigations are needed to establish if this is the actual situation. The DI vs. temperature trend for monomeric and dimeric signals was evaluated, and the monomeric signal, as expected, showed a paramagnetic trend in agreement with the Curie law. On the other hand, the dimer signal showed the same

trend observed for the verdigris pigment: the DI plot against the temperature displays a maximum around 210 K suggesting a ferromagnetic-antiferromagnetic transition. Therefore, we can suppose the presence of cooperative magnetism, i.e., the copper dimers are probably placed in a short-range order.

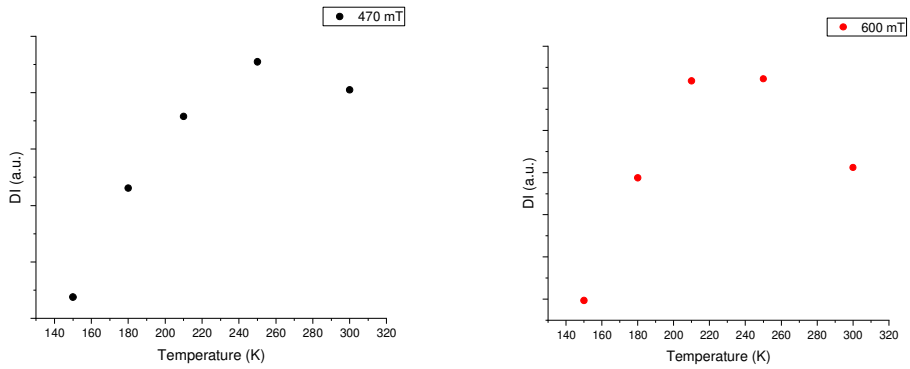

Figure 5.4: DI dimer signal vs temperature: 470 mT (black dots) and 600 mT (red dots).

In fact, also the ATR-IR spectrum of the raw copper resinate show signals very similar to the verdigris. The resin signal (Venice turpentine) is also observed, while minor signals below 1500 cm^{-1} suggest possible copper-binder interactions.

Two series of samples with different copper resinate/binder ratio (1:3 and 5%) were prepared and evaluated by CW-EPR and ATR-IR techniques. The considerations made for the verdigris pigment are valid also for the copper resinate. Moreover, the simulation values for spectra acquired at room temperature and 150 K are similar, suggesting that the same kind of complexes are formed. Therefore, we can conclude that, much alike what observed with verdigris, the complexes originally present in the copper resinate are broken by the binder molecules, forming new monomeric copper-binder complexes.

A difference is observed in the copper resinate with linseed oil (sample RRO5) with respect the same sample with verdigris (sample VRO5): there is no evidence in the DI

vs. temperature plot of a residual ferromagnetic behavior. This is probably related to a complete disruption in oil of the copper resinate pigment particles. As for verdigris, the monomer signals have a paramagnetic nature.

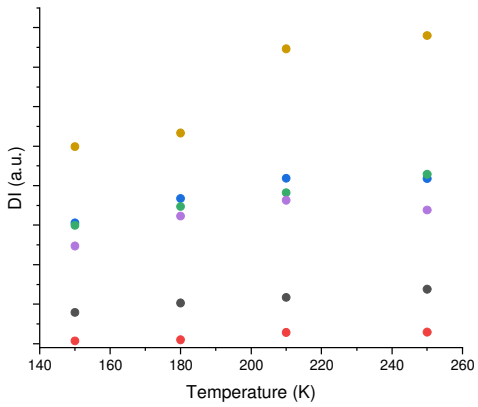

Figure 5.5: DI of dimer signal (470 mT) vs temperature: RRC5 (red dots), RREW5 (blue dots), RRY5 (green dots), RREY5 (purple dots) and RRO5 (yellow dots).

Malachite and azurite were copper pigments of natural origin, widely used by ancient painters as green and blue pigments, respectively. They are carbonate pigments, as discussed in the Chapter 2.

The CW-EPR spectrum of natural malachite (LM) is very complex. Fe(III) signals are very evident, while copper signals do not appear, indicating that Cu(II) ions are mainly antiferromagnetically coupled. Many signals stand out at low magnetic fields: these spectral features are due to the presence of so-called superparamagnetic species, that could be small particles of copper or iron oxides. The spectra acquired at lower temperatures suggest the presence of both types of species.

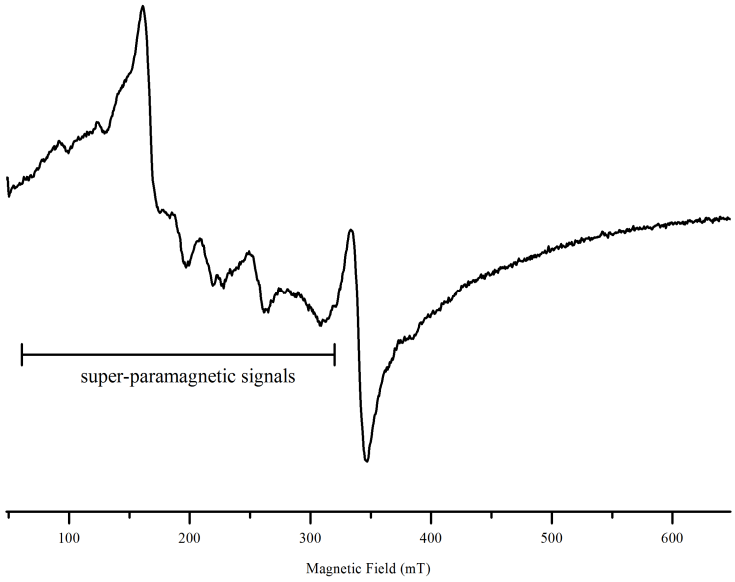

Figure 5.6: natural malachite CW-EPR spectrum at room temperature.

By comparison, also synthetic malachite was considered. Although considered "pure" malachite, iron impurities were also present in the synthetic malachite (SLM). The iron presence both in natural and synthetic pigment was verified by XRF experiments. The ATR-IR spectra of LM and SLM samples were equal and confirmed the carbonate nature of the pigment, highlighting the main vibrational modes of the CO_3^{2-} group.

Two series of samples with different malachite/binder ratio (1:3 and 5%) were prepared and evaluated by CW-EPR and ATR-IR techniques, as done for resinate and verdigris. The CW-EPR spectra of the samples with ratio 1:3 did not add further information. In fact, the copper features were covered by dominating iron signals. On the contrary, the samples at 5% showed some interesting CW-EPR spectra. In general, the analysis was disturbed by the strong iron signals, but in some spectra, the typical quartet pattern of copper monomer was observed. In these cases, it was possible to simulate the spectra and collect the spectral parameters. It is generally observed that the same binder induced some monomeric copper complexes, which were similar in

verdigris, copper resinate and malachite. However, some other complexes showed different parameters for the three pigments. This suggests that the different starting structure of the raw pigment can affect the type of complexes, either because some ligand present in the raw pigment (e.g., carbonate in malachite) is conserved also in some monomeric complexes after mixing with the binder, or because of differences in the environment (e.g., different pH). Actually, some complexes were typical of malachite mixtures.

The DI plot against the temperature confirmed the paramagnetic nature of the copper monomer signals, even if the analysis was very disturbed by residual iron signals.

The ATR-IR spectra highlighted some small differences compared to the raw pigment and the raw binder ones, suggesting the formation of copper complexes, as seen for the previous pigments.

The azurite has the same magnetic properties of malachite, as expected for two carbonate pigments. Even in the azurite are evident signals due to superparamagnetic species, related to the presence of iron and copper oxides. The presence of the two metals was verified by XRF experiments. The synthetic azurite showed an EPR spectrum even more complicated than the natural azurite. In fact, the oxides signals were absent, but Mn(II) features were evident.

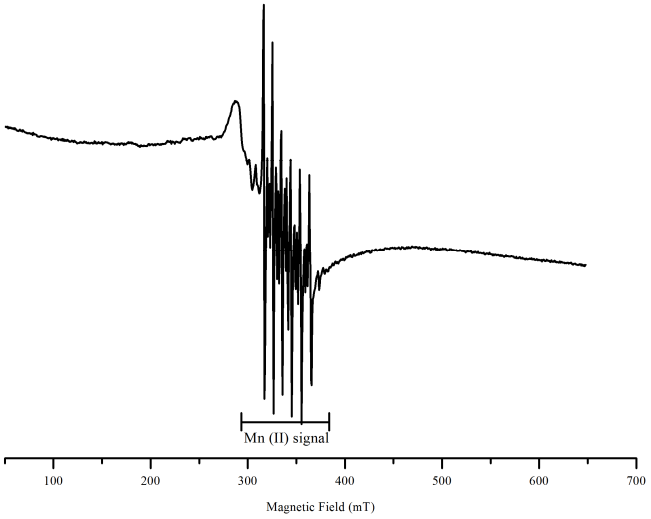

Figure 5.7: synthetic azurite CW-EPR spectrum at room temperature.

The samples with different in pigment/binder ratio (1:3 and 5%) were prepared and evaluated by CW-EPR and ATR-IR techniques. The spectra of both kinds of sample were very disturbed by iron signals, even more than for malachite. Therefore, the experimental spectra were not simulated. However, in some cases, the quartet features slightly stood out from the iron signals. Not even low temperature experiments allowed a better analysis: just some features in the CW-EPR spectra were indicative of the possible presence of monomeric copper complexes. In addition, small changes in the ATR-IR spectra in the region around 1600 cm^{-1} suggested a possible copper complexation.

Chapter 6: Conclusions

The aim of this master's thesis work is to investigate through continuous wave-EPR (CW-EPR) the possible formation of copper complexes in mixtures of copper-based pigments (e.g. verdigris, copper resinate, malachite and azurite) and many natural binders (e.g. yolk, egg white, arabic gum, rabbit glue and linseed oil).

The obtained results have been very interesting for the field of cultural heritage, highlighting the great potential of the EPR technique in the characterization of copper species, which are well know active catalysts in degradation reactions (oxidation and hydrolysis).

First, the majority of the mixtures shows copper monomer signals in the spectra, suggesting a significant interaction between the pigments and the binders. Therefore, the pigments are not simply dispersed in the binder matrices, but a certain amount of them is actually dissolved to form Cu(II) complexes with molecules of the binder. To the best of our knowledge, this is the first time in literature that such copper complexes are clearly identified.

Secondly, it is noticed that protein binders induce the formation of more monomer copper complexes, resulting in a stronger EPR signal of monomer copper species, as expected because of the great capability of the copper to bind nitrogen atoms present in the proteins.

The raw verdigris pigment and the raw copper resinate pigment show dimer signals due to their molecular structures. Evaluating the trend of the Double Integral (DI) with temperature of these dimeric signals, a typical trend ferromagnetic-antiferromagnetic has been observed, indicative of magnetic ordering typical for many interacting

magnetic centers. On the other hand, in the mixtures of verdigris/copper resinate with the 1:3 pigment/binder ratio, the dimeric signals often did not disappear, but the magnetic trend of DI vs. temperature was typical of paramagnetic species (isolated species), suggesting that a certain amount of dimer dissolves in the binder matrices without generating monomer species.

Finally, it was observed that the verdigris and the copper resinate pigments dissolve better in the binders than the azurite and the malachite ones. Although the analysis of malachite and the azurite spectra has been complicated by the presence of many EPR-active species (e.g. superparamagnetic species, Mn(II) or Fe(III) complexes), the EPR intensity of detected copper monomer species was always quite low, suggesting that these pigments were less interacting with the binders.

As known since ancient times, the verdigris and the copper resinate pigments are more prone to degradation than the malachite and the azurite ones, and this could suggest a correlation between the number of the complexes formed in the mixtures and the degradation tendency of these pigments. More investigations on these aspects are required to establish a clear correlation.

These results pave the way for further studies: first, the characterization of copper complexes by advanced EPR techniques e.g. the Electron Spin Echo Envelope Modulation (ESEEM) and the Electron Nuclear DOuble Resonance (ENDOR); secondly, the characterization of artificially aged materials to study the evolution of the copper complexes evolution in the degradation processes, and their impact with respect to type and amount of copper complexes.

Bibliography

[1] Brunello F. *De Arte Illuminandi e altri trattati sulla tecnica della miniatura medievale*; Neri Pozza Editore.

[2] Brostoff, L. B.; Connelly Ryan, C. Tracing the Alteration of Verdigris Pigment through Combined Raman Spectroscopy and X-Ray Diffraction, Part I. *Restaurator. International Journal for the Preservation of Library and Archival Material* **2020**, *41* (1), 3–30..

[3] Lazzarini, A.; Cavallo, G.; Cassitti, P. Microstratigraphic Research of Altered Medieval Painted Plaster Fragments from the St John Monastery in Müstair (Grison Canton, Switzerland). *Studies in Conservation* **2022**, 1–11.

[4] Vermeulen, M.; Sanyova, J.; Janssens, K.; Nuyts, G.; De Meyer, S.; De Wael, K. The Darkening of Copper- or Lead-Based Pigments Explained by a Structural Modification of Natural Orpiment: A Spectroscopic and Electrochemical Study. *J. Anal. At. Spectrom.* **2017**, *32* (7), 1331–1341.

[5] Zoleo, A.; Nodari, L.; Rampazzo, M.; Piccinelli, F.; Russo, U.; Federici, C.; Brustolon, M. Characterization of Pigment and Binder in Badly Conserved Illuminations of a 15th-Century *Archaeometry* **2014**, *56* (3) 496-512.

[6] Hawkins, C. L.; Davies, M. J. Oxidative Damage to Collagen and Related Substrates by Metal Ion/Hydrogen Peroxide Systems: Random Attack or Site-

Specific Damage? *Biochimica et Biophysica Acta (BBA) - Molecular Basis of Disease* **1997**, *1360* (1), 84–96.

[7] Ciglanská, M.; Jančovičová, V.; Havlínová, B.; Machatová, Z.; Brezová, V. The Influence of Pollutants on Accelerated Ageing of Parchment with Iron Gall Inks. *J. Cult. Herit*. **2014**, *15* (4), 373–381.

[8] Cennini C. *The Book of the Art of Cennino Cennini: A Contemporary Practical Treatise on Quattrocento Painting*, translated by Herringham J.C., George Allen, Ruskin House, London (original edition *Il Libro dell'Arte*, Padova, XIV-XV century).

[9] Unknown *Eraclio. I Colori e le Arti dei Romani e la compilazione pseudo-eracliana*, translated and commented by Romano G.C., Società editrice Il Mulino, 1996 (original edition *Eraclii sapientissimi viri. De coloribus et de artibus Romanorum*, VIII-X century).

[10] Plinio il Vecchio *Storia delle Arti Antiche (libri XXXIV-XXXVI)*, translated by Maurizio Harari, BUR – classici greci e latini, 2000 (original edition *Naturalis Historia*, 77-78 d.C.).

[11] Marco Vitruvio Pollione *De Architectura traslated* by Luciano Migotto, Studio Tesi Edizioni, 2008 (original edition De Architectura 15 a.C.).

[12] Unknown *Mappae Clavicula. Alle origini dell'alchimia in Occidente*, translated by Sandro Baroni, Giuseppe Pizzigoni and Paola Travaglio, Il Prato, 2013 (original edition *Mappae Clavicula*, VIII-IX century).

[13] Braxandall M. Pittura ed esperienze sociali nell'Italia del Quattrocento; Piccola Biblioteca Einaudi, Torino, 2000.

[14] Van Niekerk, J. N.; Schoening, F. R. L.; de Wet, J. F. A new type of copper complexs found in the crystal structure of cupric acetate $Cu_2(CH_3COO)_4 \cdot 2H_2O$. *Acta Crystallogr*. **1953**, 6, 501–504.

[15] Brown, G. M.; Chidambaram, R. Dinuclear copper (II) acetatemonohydrate: a redetermination of the structure by neutron-diffraction analysis. *Acta Crystallogr., Sect. B: Struct. Crystallogr. Cryst. Chem*. **1973**, 29, 2393–2403.

[16] Alter, M.; Binet, L.; Touati, N.; Lubin-Germain, N.; Le Hô, A.-S.; Mirambet, F.; Gourier, D. Photochemical Origin of the Darkening of Copper Acetate and Resinate Pigments in Historical Paintings. *Inorg. Chem.* **2019**, *58* (19), 13115–13128.

[17] Gettens, R. J. Identification of the materials in paintings. *Studies in Conservation* **1966**, *11* (2), 52–53.

[18] Mills J.S., White R. *The organic chemistry of museum objects*, *2nd edition*, Arts and archaeology, Butterworth-Heinmann Ltd., Oxford, **1994**

[19] Laurie,A.P. *The Pigments and Mediums of the Old Masters*, Macmillan and Co., Ltd., London 1914, pp. 35-39 and 99-103.

[20] Flieder, F., 'Mise aupoint des techniques d'identification des pigments etdes liants indus dans lacouche picturale des enluminures demanuscrits', *Studies in Conservation*, **1968**, 13, 49-86, (c.f. pp. 60-62).

[21] R. G. Burns editor *Mineralogical applications of crystal field theory, 2nd edition*, Cambridge University Press, **1993.**

[19] Vasari G. *Le vite de' più eccellenti pittori scultori e architettori*, Vol.1, Edizioni per il club del Libro, Milano, **1962**

[22] Lambert, J. B. *Archaeological Chemistry—III*; Ed.; Advances in Chemistry; American Chemical Society: Washington, D.C., **1984**; Vol. 205.

[23] Regert, M.; Colinart, S.; Degrand, L.; Decavallas, O. Chemical Alteration and Use of Beeswax Through Time: Accelerated Ageing Tests and Analysis of Archaeological Samples from Various Environmental Contexts. *Archaeometry* **2001**, *43* (4), 549–569.

[14] Peisach, J.; Blumberg, W. E. Structural Implications Derived from the Analysis of Electron Paramagnetic Resonance Spectra of Natural and Artificial Copper Proteins. *Archives of Biochemistry and Biophysics* **1974**, *165* (2), 691–708.

[25] Zoleo, A.; Speri, L.; Bronzato, M. Electron Paramagnetic Resonance as a Probe for Metal Ions and Radicals in Paper. *Restaurator. International Journal for the Preservation of Library and Archival Material* **2015**, *36* (4).

[26] Stoll, S.; Schweiger, A. EasySpin, a Comprehensive Software Package for Spectral Simulation and Analysis in EPR. *Journal of Magnetic Resonance* **2006**, *178* (1), 42–55.

[17] Bette, S.; Costes, A.; Kremer, R. K.; Eggert, G.; Tang, C. C.; Dinnebier, R. E. On Verdigris, Part III: Crystal Structure, Magnetic and Spectral Properties of Anhydrous Copper(II) Acetate, a Paddle Wheel Chain: On Verdigris, Part III: Crystal Structure, Magnetic and Spectral Properties of Anhydrous Copper(II) Acetate, a Paddle Wheel Chain. *Z. Anorg. Allg. Chem.* **2019**, *645* (15), 988–997.

[28] Platania, E.; Streeton, N. L. W.; Kutzke, H.; Karlsson, A.; Uggerud, E.; Andersen, N. H. Infrared, Raman and Computational Study of a Crystalline Mononuclear Copper Complex of Relevance to the Pigment Verdigris. *Vibrational Spectroscopy* **2018**, *97*, 66–74..

[29] Wiggins, M. B.; Heath, E.; Booksh, K. S.; Alcántara-García, J. Multi-Analytical Study of Copper-Based Historic Pigments and Their Alteration Products. *Appl Spectrosc* **2019**, 000370281985660.

[30] Nepveu, F.; Magnetic Properties and EPR Spectra of Tetranuclear Copper(I1) Complexes. *Inorg. Chem.* Act. **1987**, 134*,* 43-48..

[31] Burkhardt, A.; Spielberg, E. T.; Görls, H.; Plass, W. Chiral Tetranuclear μ_3 -Alkoxo-Bridged Copper(II) Complex with 2 + 4 Cubane-Like Cu_4O_4 Core Framework and Ferromagnetic Ground State. *Inorg. Chem.* **2008**, *47* (7), 2485–2493.

[32] Wang, G.; Yang, H.; Liu, Y.; Tong, L.; Auwalu, A. Study on the Mechanical Activation of Malachite and the Leaching of Complex Copper Ore in the Luanshya Mining Area, Zambia. *Int J Miner Metall Mater* **2020**, *27* (3), 292–300.